Spring 2012

De-Centralized and Centralized Control for Realistic EMS Maglev Systems

Mohamed M. Aly M. Moawad
Old Dominion University

DE-CENTRALIZED AND CENTRALIZED CONTROL FOR REALISTIC EMS MAGLEV SYSTEMS

by

Mohamed M. Aly M. Moawad
M.Sc. March 2006, Cairo University, Egypt

A Dissertation Submitted to the Faculty of
Old Dominion University in Partial Fulfillment of the
Requirements for the Degree of

DOCTOR OF PHILOSOPHY

AEROSPACE ENGINEERING

OLD DOMINION UNIVERSITY
May 2012

Approved by:

Thomas Alberts (Director)

Colin Britcher (Member)

Jeremiah Creedon (Member)

Brett Newman (Member)

Oscar González (Member)

ABSTRACT

DE-CENTRALIZED AND CENTRALIZED CONTROL FOR REALISTIC EMS MAGLEV SYSTEMS

Mohamed M. Aly M. Moawad
Old Dominion University, 2012
Director: Dr. Thomas Alberts

A comparative study of de-centralized and centralized controllers when used with real EMS Maglev Systems is introduced. This comparison is divided into two parts. Part I is concerned with numerical simulation and experimental testing on a two ton six-magnet EMS Maglev vehicle. Levitation and lateral control with these controllers individually and when including flux feedback control in combination with these controllers to enhance stability are introduced. The centralized controller is better than the de-centralized one when the system is exposed to a lateral disturbing force such as wind gusts. The flux feedback control when combined with de-centralized or centralized controllers does improve the stability and is more resistant and robust with respect to the air gap variations. Part II is concerned with the study of Maglev vehicle-girder dynamic interaction system and the comparison between these two controllers on this typical system based on performance and ride quality achieved. Numerical simulations of the ODU EMS Maglev vehicle interacting with girder are conducted with these two different controllers. The de-centralized and centralized control for EMS Maglev systems that interact with a flexible girder provides similar ride quality.

Centralized control with flux feedback could be the best controller for the ODU Maglev system when operating on girder. The centralized control will guarantee the

suppression of the undesired lateral displacements; hence it will provide smoother ride quality. Flux feedback will suppress air gap variations due to the track discontinuities.

This dissertation is dedicated with love, to my parents and my wife.

ACKNOWLEDGEMENTS

First of all, I would like to express my sincere and heartfelt appreciation and thanks to my advisor, Professor Thomas Alberts. I was really lucky to work with him, and I have learned a lot from him. The completion of this research would have been impossible without his guidance and encouragement.

I wish to express my special thanks to Professor Colin Britcher for his help, support and for his suggestions in improving the write-up of this dissertation.

I am extremely thankful to Professors Jeremiah Creedon, Brett Newman and Oscar González for being a part of my committee and reviewing this manuscript. The financial support by the Aerospace Engineering Department of Old Dominion University and ODU research foundation are gratefully acknowledged.

Finally, I can never thank enough my parents Mr. Mohamed Aly and Mrs. Nesma Wanas, and my wife Mrs. Rania Naoum. Without their unconditional love, I could have never come so far. This dissertation is dedicated to them.

TABLE OF CONTENTS

LIST OF FIGURES

LIST OF TABLES

CHAPTER 1

INTRODUCTION

1.1 Introduction

Since the 1970's, magnetic levitation has been successfully implemented for many applications. The applications include transport, magnetic bearings, space launch systems and vibration isolation. Maglev is a high-speed ground transportation method that uses contact-less levitation, and guidance and propulsion electromagnetic principles, potentially reaching velocities comparable to turbo propeller and jet aircraft (550 to 700 km/h) in regular service [1]. Maglev is a fast, safe, and nearly pollution free transportation method. Conversely, it is historically known to be technically challenging to develop and expensive to establish. However, early examples of Maglev were constructed in Japan, and Germany three decades ago.

There are two types of magnetic levitation: Electro-Dynamic Suspension (EDS), and Electro-Magnetic Suspension (EMS). This dissertation is concerned with EMS Maglev systems.

A full-scale Electro-Magnetic Suspension (EMS) Maglev demonstration system is currently being used as research vehicle on the Old Dominion University (ODU), Norfolk VA campus by several of the university's engineering faculty and students [2-9]. The ODU test vehicle (bogie) is basically an aluminum structure equipped with six electromagnets, six Pulse Width Modulated (PWM) power amplifiers, two linear induction motors (LIMs) along with position and acceleration sensors, and data acquisition and control equipment. The original Maglev system was installed on the Old

Dominion University (ODU) campus by American Maglev Technologies (AMT) from the years 2001 to 2002 with the intention of becoming a permanent student transportation system [8]. After installation of the system at ODU and some initial on-campus testing, the project came to a halt due to technical difficulties in achieving stable levitation. The inability to achieve stable levitation was attributed to flexibility of the guideway girders. A quick interpretation of the problem is that when the Maglev vehicle is moving on a flexible girder, the measured air gaps are affected due to the relaxation of the girder, which was not accounted when the controller was designed. In order to design an appropriate controller for the system, the dynamics of a flexible guideway should be added to the vehicle's dynamics to form a complete vehicle-guideway interaction model that accounts for that inevitable interaction. One of the issues that needs to be addressed in this regard is the interaction between the Maglev vehicle and a flexible guideway in combination with the controller scheme (de-centralized or centralized), as flexible guideways are lower in construction cost than rigid ones.

An open research issue at the ODU Maglev test lab is the EMS Maglev guidance (lateral control) problem. Usually, the guidance in EMS Maglev systems is attained by one of two methods [10-12]. The first approach is to use separate magnets for levitation and guidance; the second is to use the levitation magnet set for levitation and guidance with a special type of guideway tracks called inverted U-rail tracks. The ODU Maglev system employs the second method.

In this dissertation, the comparison between de-centralized and centralized controllers of an electromagnetically suspended vehicle (EMS Maglev) will be studied. The comparison will include the application of these controllers on the EMS Maglev

vehicle for two cases: first, when interacting with a flexible guideway (after understanding the interaction); and second, for levitation and guidance control when inverted U-rails are utilized. Flux feedback will be added in combination with these controllers to improve the stability. Experimental testing of these controllers (especially for levitation and guidance control) is carried out in Old Dominion University's Maglev test facility, on the demonstration vehicle that is also called the "Test Bogie."

In this chapter, Maglev systems and their working principles are briefly introduced. Literature related to this work is reviewed with focus on Maglev systems, EMS Maglev research at ODU, Maglev-girder interaction, guidance control and de-centralized/ centralized controllers. The motivation behind and the scope and goals of this research work are specified.

Chapter 2 presents the modeling of EMS Maglev systems: 1-DOF and 2-DOF system models for an inverted U-rail. Multivariable control tools will be utilized for analysis. Methods for multivariable PID controller gains selection are presented. Concepts of de-centralized, centralized and flux feedback controllers are illustrated. Simple EMS Maglev systems are studied first before working with the ODU EMS Maglev system.

In chapter 3, a detailed analysis of de-centralized and centralized control for an EMS Maglev system levitation and guidance is introduced. A simple EMS Maglev model (rigid case) that exhibits the heave and lateral motions is studied. The flexible case is considered by attaching one flexible mode to the heave motion of that model. The MIMO root loci for the 2-DOF system with de-centralized and centralized controllers are shown.

Numerical simulations are carried out using MATLAB/SIMULINK® for these typical systems after using a unified criterion for controllers' gains selection.

Chapter 4 presents the complete model for the ODU EMS Maglev bogie. The de-centralized and centralized control for that system is introduced. Flux feedback control in combination with the de-centralized and centralized control for the system is described. Numerical simulation is performed using MATLAB/SIMULINK® for the system with these controllers. Details of the experimental testing of the test bogie with de-centralized controller are also presented.

Chapter 5 presents the details for the generalized Maglev-girder interaction LPV model, and its dynamic change with regard to the vehicle's position. A simple 2-DOF Maglev-girder interaction model is presented for the purpose of study and investigation of its dynamic change with vehicle position and velocity. The MIMO root loci for that simple system with de-centralized and centralized control schemes are shown. Concepts for ride quality are also presented. The simulation results for the ODU Maglev bogie with de-centralized and centralized control when applying a unified approach for controllers' gains selection based on LQR criterion are presented.

In Chapter 6, conclusions that can be drawn from this research work are presented. Recommendations for future work are also provided. The next sections introduce Maglev systems and their working principles.

1.2 Maglev Systems

The word "Maglev" is derived from MAGnetic LEVitation. Maglev is a transportation system that suspends, guides and propels vehicles, essentially trains. These vehicles use magnetic field for levitation and propulsion, enabling them to achieve speeds

up to 700 km/h comparable to turbo propeller and jet aircraft in regular service. Unlike wheel-on-rail trains, Maglev vehicles have no mechanical contact with the guideway, in this manner frictionless and nearly noiseless propulsion. Basically, there are two types of Maglev systems realized in practice, EDS and EMS systems. These are briefly described below.

1.2.1 Electrodynamic Suspension Systems (EDS)

EDS systems rely on forces of repulsion between the vehicle and guideway. The train employs magnets that induce current in the guideway that creates a repulsive magnetic field which causes the levitation. EDS systems are inherently stable because, the resulting repulsive force increases as the gap decreases [13]. Most EDS Trains as shown in Figure 1.1 must be in motion to levitate so the vehicle must be equipped with wheels because the EDS will not levitate at speeds below the critical speed.

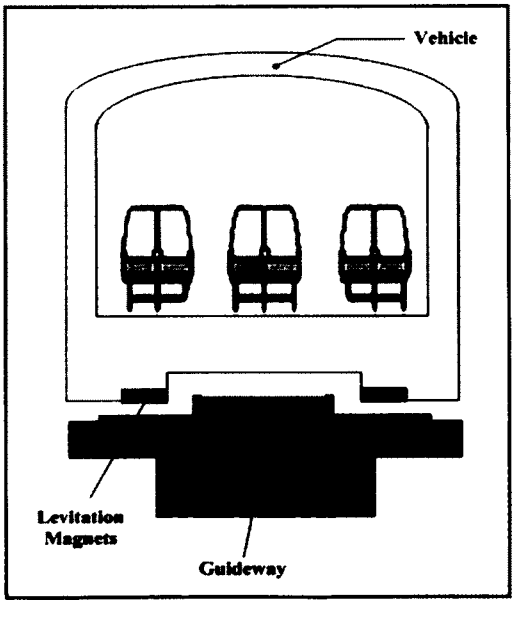

Figure 1.1. EDS Maglev System Concept

There are some modern EDS Maglev systems can levitate at zero speed such as the Korean HTSC system by using AC superconducting magnets [3].

1.2.2 Electromagnetic Suspension Systems (EMS)

EMS systems rely on forces of attraction between the vehicle and guideway. As shown in Figure 1.2, the electromagnets on the vehicle interact with and are attracted to ferromagnetic tracks on the guideway that results in the levitation of the vehicle. This enables EMS systems to levitate at zero speed. In EMS systems, the force that is produced by the electromagnet is a nonlinear function of the magnet current and the airgap. This nonlinear function is basically an inverse square relationship that produces a fundamentally unstable open-loop characteristic [14]. This can either be modeled as a (nonlinear) negative spring, or the suspension's linearized transfer function can be shown to have a positive real pole (eigenvalue). Since, the EMS systems are open loop unstable, feedback control is necessary in order to stabilize them.

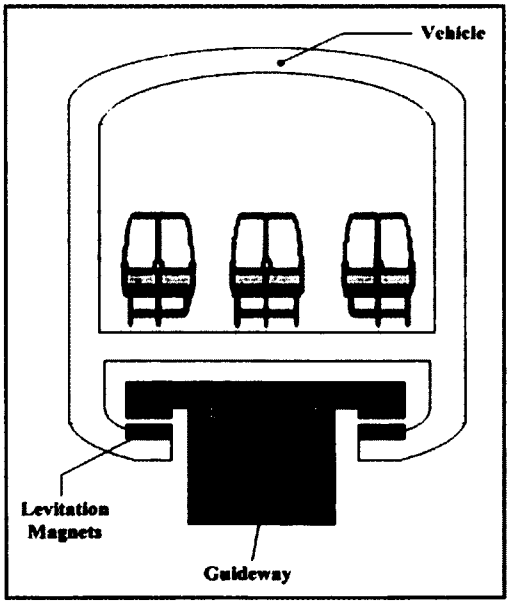

Figure 1.2. EMS Maglev System Concept

1.3 Literature Review

Literature related to Maglev research will be divided into those including control of EMS Maglev systems, EMS Maglev research at ODU, control of Maglev-girder (guideway) system interaction, EMS Maglev levitation and guidance control, and de-centralized and centralized control. In the following, a brief review of some important works related to the above-mentioned categories is presented.

1.3.1 Control of EMS Maglev Systems

Various kinds of control techniques have been applied and tested on simple Maglev systems such as magnetic ball levitation and levitation of one or two mass systems. Some of these are described below. In [10-12], the nonlinear equations of a 2-DOF EMS Maglev system that represent heave and lateral motions are presented. The authors linearized the system model and show that with small displacements, the system's heave and lateral motions are de-coupled and successfully designed individual controllers for each channel. The basic model that describes the modeling of a simple one mass magnetic levitation system is described in [13].

Other topics like ride quality, dynamic interaction between guideway and the vehicle, centralized and de-centralized control and a review of current research (of the 1980's) in Maglev are presented. The principle of the magnetic levitation design for passenger transport application (Maglev at Birmingham) is explained in [15]. The hypothesis that measurements of magnet current and airgap flux density are sufficient for stable control is explored, and strategies by which such control can be achieved are examined in [16]. A robust observer design to estimate the airgap and flux density for a single-axis Maglev system is introduced in [17]. Research for small experimental vehicle

levitation to test the control of an EMS Maglev system using a centralized non-linear electromagnet force control algorithm and a guideway following algorithm is conducted in [18]. The effect of using different sets of state variables in designing linear optimal controllers for Maglev vehicles is examined in [19]. A nonlinear state transformation, along with a PI controller for the levitation of 1-DOF EMS Maglev system, which leads to second order model of the system, is obtained. The result concluded from this work is that good performance can be achieved for Maglev systems using simple controllers.

1.3.2 EMS Maglev Research at ODU

At Old Dominion University (ODU), Norfolk VA campus, there is a full-scale Electro Magnetic Suspension (EMS) Maglev demonstration system that is established and tested. As part of this research effort, design and implementation of control systems for a Maglev laboratory experiment (1-DOF Maglev test rig) at Old Dominion University are described in [2]. A detailed dynamic model for the ODU Maglev test-vehicle that incorporates structural dynamics with flexible modes of vibration, non-linear electrodynamics, feedback controllers, discrete time implementation, noise filters and disturbance inputs is developed and validated via real time experimental testing in [3]. Dynamic modeling, numerical simulation and experimental validation of an EMS demonstration vehicle are presented in [4]. This dynamic model incorporates rigid body modes as well as a finite number of flexible modes of vibration. De-centralized PID controllers are designed individually for each of the six electromagnets. A dynamic model of the vehicle-girder coupled with a controller is developed for the ODU Maglev demonstration system using software– MADYMO in [5]. MADYMO stands for MAthematical DYnamic Models, a software package developed by TASS for design and

analysis for occupant safety systems in the transport industry. A study on the effects of track irregularities on the dynamic responses of a Maglev train is presented. The track here is a combination of concrete guideway, rails and ribs. Its irregularities can be due to the flexibility and the unevenness of the track in [6]. A simple analysis evaluating the stability threshold for magnetically levitated flexible structures using dissipative collocated controllers is presented in [7]. A single degree of freedom test rig was constructed using one magnet and a short section of rail from the Old Dominion University Maglev system in [8]. The analysis of stability requirements for EMS magnetically levitated vehicles with structural flexibility and the implications of collocated versus non-collocated control is contrasted in the context of the stability of flexible modes in [9].

1.3.3 Control of Maglev-Girder Interaction

The model of a Maglev vehicle moving on a guideway was introduced in the cases of a concentrated and distributed vehicle loads at different vehicle speeds in [21] showing that the speed of vehicle changes the girder vibration shape and amplitude. After this, many research reports have been presented to study vehicle-girder interaction with many theoretical and simulation details in terms of vehicle velocity, vehicle dynamics, electrodynamics and controllers. Refs. [22-31] are the most recently conducted research in this area. Some of these research papers consider the girder vibration as disturbance injected to the vehicle model [22-23] and others consider the girder flexible model as a part of the system [24-28]. Most of the research on vehicle-girder interaction focuses on studying dynamics and response [26,30-31], applying different controller techniques (Nonlinear H_∞ [23], and LQR [24], neuro-PI [29]), and optimally design the for girder or

vehicle parameters [27-28]. In [22], a dynamic interaction model of a 5-DOF Maglev vehicle-guideway system under controllable magnetic suspension forces is developed. The vehicle is simplified as a body with primary and secondary suspension parts. Regions for the disturbance of heave motion or/and lateral motion and the control parameters are numerically searched to stabilize the system. Nonlinear H_∞ state and output feedback controllers for EMS Maglev vehicles are developed in [23]. Experimental results from a 1-DOF suspension system are included to highlight the effectiveness of the proposed nonlinear state- and output-feedback controllers to suppress guideway-induced disturbances.

In [24] the authors suggested that if the vibration mode frequency of a single span guideway is very high compared with the span crossing frequency of the vehicle, the guideway deflection by the weight of the vehicle can be assumed to be quasi-static. In [25], a vibration analysis of the coupled equations of motion of 3-DOF Maglev vehicle-guideway is derived for the improvement of performance and reduction of construction costs.

A numerical model incorporating guideway dynamics, vehicle dynamics (with 16 electromagnetic forces), guideway irregularity, and the interaction of different systems is developed in [26]. The guideway irregularity model has greater influence on the acceleration of the vehicle body rather than those on the guideway displacement.

For the Mashhad-Tehran Maglev system, a model for guideway load distribution and accuracy of such a model is the backbone for optimized guideway design. Parameters that are effective for the analysis and design of guideways, including its loading patterns and structural models, are investigated. Vehicle mechanical design and its loading

capacity, in addition to guideway geometry and properties of magnetic force elements, are used to develop the loading models in [27].

In [28], simulation for a Maglev vehicle model with 30-DOF (five-cars) operating over a single-span elevated U-shaped girder guideway was performed. It was shown that a distributed-load vehicle model is better than a concentrated-load model, and multicar vehicles have less car-body acceleration than does a single-car vehicle because of intercar constraints, which indicates that the multicar vehicle would provide better ride comfort.

A neuro- PI (proportional-integral) controller to control a Maglev vehicle (2-DOF moving oscillator) interacting with a simply supported beam guideway is introduced in [29]. The Maglev vehicle model is simplified as evenly distributed force acting on the guideway at constant speed by using the mode superposition method.

In [30], they concluded that closed-form solutions of the guideway imply that vehicle–guideway interaction does not necessarily occur with the Maglev vehicle passing across a bridge at constant speed. From the analytical results of the impact factor, the displacement of the rail and bridge could reach their local extreme value if the running speed of the load is close to certain values.

The vertical acceleration response of a simple beam traveled by a series of equally spaced moving loads at constant speeds is studied by the superposition method was presented in [31]. The maximum acceleration response of the beam is dominated by the fundamental vibration mode for a properly damped beam.

1.3.4 EMS Maglev Levitation and Guidance Control

One of the current research issues at the ODU Maglev test lab is the EMS Maglev guidance problem (lateral control). Usually, guidance in EMS Maglev systems can be

achieved by two different methods [10]. The first is to use separate magnets for levitation and guidance, the second is to use a combined magnet set for levitation and passive guidance with a special type of guideway tracks called inverted U-rail tracks. Guidance can be attained actively using the combined magnet set that is laterally offset or staggered [11-12] when centralized control is employed. When de-centralized control is used, guidance is achieved passively. The ODU Maglev system is concerned with the second method. Figures 1.3 and 1.4 show simple sketches for EMS Maglev levitation and guidance methods.

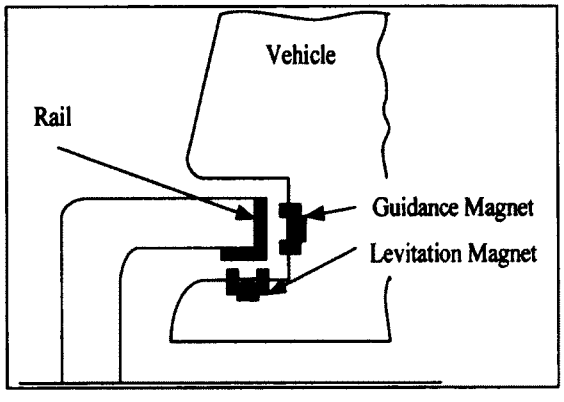

Figure 1.3. Separate Levitation and Guidance

In [32], PID centralized and de-centralized controllers were designed to control the 1-ton Maglev research vehicle at the University of Sussex. The lateral control for that system was achieved using guidance magnets. De-centralized control of the guidance clearance is achieved by using separate electromagnets for the German Transrapid Maglev [33].

Few papers in the literature have discussed the problem of EMS Maglev guidance control especially when electromagnets are used for both levitation and guidance. In [10-12], the decoupling between heave and lateral channels is performed after linearization

for a lightweight EMS Maglev system, then two separate controllers for the heave and lateral channels are utilized.

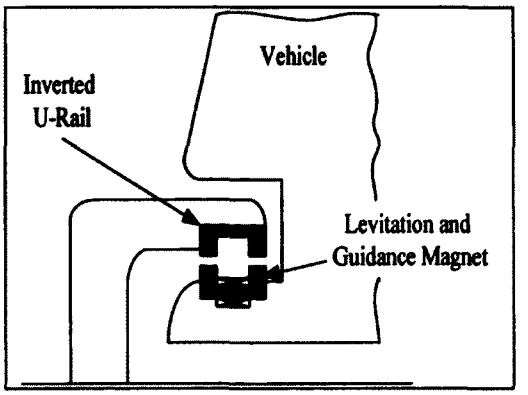

Figure 1.4. Combined Levitation and Guidance

A guide-effective EMS (by combining a levitating mode with a guiding mode) with a controller that is based on pole placement techniques is used for controlling both levitation and guidance modes [34]. A MATLAB/SIMULINK based model for a high speed Maglev train with vertical and lateral control is presented [35] in which LQR control is used for each single mass magnet. A Magnemotion report states that by using a magnetic gap that is ¼ the width of the suspension rails it is possible to provide passive guidance with a lateral guidance force up to 33 % of the vertical lift force [36].

1.3.5 De-centralized and Centralized Control

Necessary conditions for the existence of a de-centralized control law that meets specified feedback system requirements were developed in [37]. De-centralized control can be limited in terms of achieving acceptable performance if the required bandwidths of the closed-loop subsystems greatly differ. Some systems that exhibit special

uncontrollability and unobservability properties cannot be stabilized under de-centralized control.

The problem of stabilizing a decentralized linear time-invariant multivariable system via local output feedback with dynamic compensation is investigated in [38]. The concept of "Fixed Modes" was presented as a necessary and sufficient condition for solution existence. A systematic design of stabilizing de-centralized controllers for large-scale interconnected dynamic systems is presented in [39]. The design is obtained by model reduction and modeling of interactions between the subsystems comprising the overall system. Three design schemes are proposed with feed-forward, feedback and static compensators.

A review of the decentralized control of large scale interconnected systems concepts, methods, and results have been presented in [40]. Decompositions of large scale systems that provide the integration of decentralized control and parallel computation are also introduced.

In [41], the structures of de-centralized and centralized controllers for multivariable systems feedback control are illustrated. Stability, performance, pairing selection and controllability analysis for de-centralized control are provided.

The concepts of de-centralized and centralized control of EMS Maglev system are introduced in [13]. De-centralized control for EMS Maglev systems was applied early in development of the German Maglev system. De-centralized controllers were used for levitation and guidance control loops separately [33]. PID centralized and de-centralized controllers were developed to control the levitation and guidance of 1-ton Maglev research vehicle at the University of Sussex [32]. The de-centralized and centralized

control techniques for a 200kg test vehicle that utilizes four magnets were designed and implemented on an analog computer [42]. The control of a small experimental EMS Maglev vehicle using a centralized non-linear electromagnet force control algorithm, a suspension control algorithm, and a guideway following algorithm is developed in [18]. De-centralized and centralized control of a 2-DOF EMS Maglev system was presented in [2]. The comparison between the two controllers is performed, and it is shown that the PD centralized control is not suitable to control some flexible modes. In [3-4], a PID de-centralized controller has been successfully designed and validated for the ODU Maglev test bogie. This controller is able to control the vehicle's rigid and flexible modes efficiently. In [43], a new approach to control the levitation of a 3-DOF vehicle with four magnets is developed. The concept of the centralized control is utilized to produce the forces and moments required by the heave, roll and pitch controllers via a command policy that determines an optimal distribution of forces.

1.4 Scope and Goals of Present Work

Investigating the literature relevant to this research, it is noted that there are many interesting studies on electromagnetic suspension system levitation control [2-4,7-20], many studies on control of Maglev-girder interaction [22,31], and many studies on the Maglev guidance control [10-11,32-36]. However, understanding the Maglev-girder interaction and dynamical changes associated with vehicle velocity is not clearly mentioned. This is one of the issues addressed by this dissertation. De-centralized or centralized controller schemes and their influences on the Maglev-girder interaction system are not investigated although they are commonly used. The comparison between

these two controllers is made for Maglev-girder interaction system based on the achieved performance and ride quality.

Another topic that is under investigation in this dissertation is guidance control when the EMS Maglev system utilizes magnet set with inverted U-rail tracks. De-centralized and centralized controllers have been part of many studies [2-4,13,18,32-43], and they are both known to have advantages and limitations. In the present work, a comparative study between de-centralized and centralized controllers when applied on the EMS Maglev system is introduced when a particular concern is given to lateral control. On the ODU Maglev testing facility, the experimental testing of both de-centralized and centralized controllers will be conducted on the test bogie for validation.

Flux feedback control for EMS Maglev systems was illustrated in many references [2,13-14,18]. Measuring the flux field density in the electromagnetic suspension and feeding it back in an internal loop can improve the overall stability [2,13]. The inclusion of flux feedback in combination with de-centralized and centralized controllers will be also considered in this dissertation.

CHAPTER 2

EMS MAGLEV SYSTEM ANALYSIS AND CONTROL

2.1 Introduction

In this chapter, the modeling of EMS Maglev systems is introduced. Simple EMS Maglev systems are studied first before working with the ODU EMS Maglev system. Nonlinear and linear equations of motion of a simple single DOF EMS Maglev system are derived. Next, the equations of motion of the 2-DOF EMS Maglev system for an inverted U-rail are introduced. This system model is the simplest model that describes the heave and lateral motions (rigid case) when two magnets are used. The flexible case is considered by attaching one flexible mode to the heave motion. The static characteristics of the staggered magnet pair is presented to show how the levitation and lateral forces change with the stagger distance. Multivariable control tools that can be utilized for system analysis are presented. These tools include relative gain array (RGA), coupling factor, and the Niederlinski index. Methods for multivariable PID controller gains selection are presented. These methods include auto tuning technique, characteristic locus method, optimization method, and trial and error method. Concepts of the commonly used control techniques for EMS Maglev systems, de-centralized and centralized control, are introduced. Finally, flux feedback for EMS Maglev systems, how to use it, and its advantages including stability improvement and noise reduction are illustrated.

2.2 Single DOF EMS Maglev System Modeling

A single DOF EMS Maglev system is composed of two subsystems that interact with each other [44-45]. These two subsystems are mechanical and electrical. The mechanical subsystem is the mass dynamics and its relation with gravity. The electrical subsystem is the electrodynamics. In the following these two subsystems are introduced.

2.2.1 Mechanical System Dynamics

The dynamics of the mechanical subsystem is the subsystem that defines the mapping S_1 between the difference between levitation force and the gravity to gap z;

$$S_1 : g - \frac{F_z}{m} \rightarrow z \tag{2.1}$$

where F_z is the levitation force, m is the system mass, and g is the gravitational constant. Figure 2.1 shows the EMS Maglev mechanical subsystem.

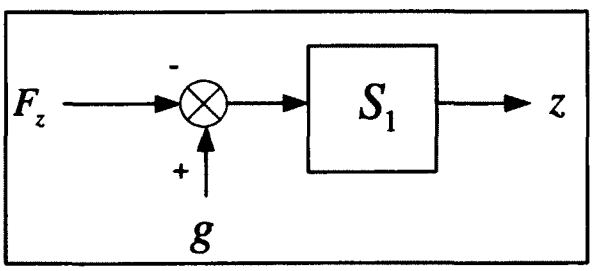

Figure 2.1. EMS Maglev Mechanical Subsystem

The conventional method that can be used to find the dynamical equations of an EMS Maglev system is based on Newton's second law:

$$m\ddot{z} = mg - F_z \tag{2.2}$$

where $\ddot{z}$ is the gap acceleration, and the levitation force is determined in the following section.

2.2.2 Electrodynamics

The electrodynamics or the electrical subsystem is the subsystem that defines the mapping S_2 between the input voltage and levitation force, and the levitation force F_z. Figure 2.2 shows the EMS Maglev electrical subsystem.

$$S_2 : V \rightarrow F_z \tag{2.3}$$

where, V is the input voltage to the electromagnet.

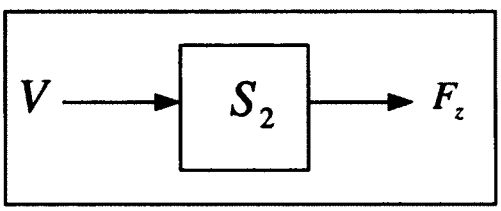

Figure 2.2. EMS Maglev Electrical Subsystem

Usually, the voltage input to an electromagnet is fed by a current amplifier. The relation that is between the input voltage to the electromagnet and the command current represents the third mapping S_3 as shown in Figure 2.3.

$$S_3 : I_c \rightarrow V \tag{2.4}$$

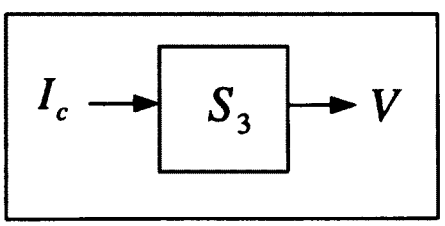

Figure 2.3. Current Amplifier

The voltage applied to the coil of the electromagnet is

$$V = RI + L(z)\frac{dI}{dt} - L(z)\frac{I}{z}\frac{dz}{dt} \tag{2.5}$$

The electromagnets are driven by current amplifiers intended to follow a current command I_c with an amplifier feedback gain K_A.

$$V = K_A(I_c - I) \tag{2.6}$$

The final current loop is

$$\frac{dI}{dt} = \frac{K_A}{L(z)}(I_c - I) - \frac{RI}{L(z)} + \frac{I}{z}\frac{dz}{dt} \tag{2.7}$$

The inner feedback loop in Eq. (2.7) provides an accurate current hold but it does not guarantee to provide a gap hold.

The instantaneous generation of an attractive force between an electromagnetic and ferromagnetic plate is the idea that is behind the magnetic levitation. The levitation system model is derived from the work in reference [46]. For the electromagnet shown in Figure 2.4, the levitation force is

$$F_z = \frac{\mu_o N^2 I^2 L_m W_m}{4z^2}\left(1 + \frac{2}{\pi}\frac{z}{W_m}\right) \tag{2.8}$$

where, μ_o : is the permeability of the free space, L_m : is the length of the magnet, W_m : is the width of the magnet and N: is the electromagnet's number of turns.

The instantaneous magnet inductance is

$$L(z) = \frac{\mu_o N^2 L_m}{2}\left(\frac{W_m}{z} + \frac{2}{\pi}\ln\left(\frac{1}{z}\right)\right) \tag{2.9}$$

In Figure 2.4, Φ is the magnetic flux. The magnetic flux of the electromagnet is

$$\Phi = \frac{\mu_o NI}{2z}\sqrt{1 + \frac{2z}{\pi W_m}} \tag{2.10}$$

Figure 2.4 shows the electromagnetic-track configuration.

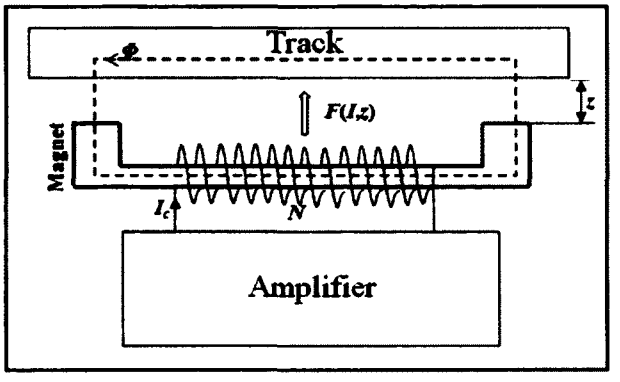

Figure 2.4. Electromagnetic-Track Configuration

The modeling of a single DOF EMS Maglev system considering the mechanical and electrical subsystems is as shown in Figure 2.5.

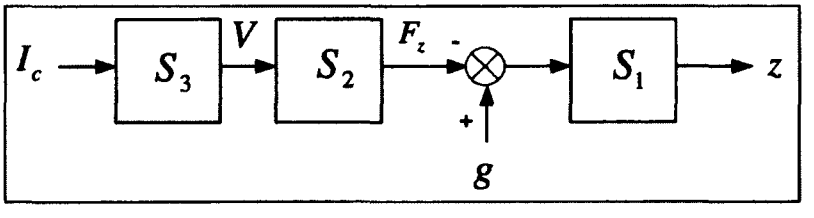

Figure 2.5. Single DOF EMS Maglev System Block Diagram

Eqs.(2.2), and (2.7) represent the complete nonlinear dynamic model for a single-axis EMS Maglev system.

2.2.3 Linearized System Dynamics

A linear model can be obtained by using a Taylor series expansion around the nominal equilibrium point (z_o, I_o), then:

$$m\Delta\ddot{z} = -k_z\left[\frac{I_o(t)}{z_o(t)}\right]^2 + k_i\Delta z$$
$$\Delta\dot{I} = \frac{k_z}{k_i}\Delta\dot{z} - \frac{K_A + R}{L}\Delta I \tag{2.11}$$

where, the coefficients k_z and k_i are computed directly from linearizing the levitation force F_z with respect to air gap z and current I around their nominal points z_o, and I_o, respectively:

$$k_z = \left.\frac{\partial F_z}{\partial z}\right|_{z_o, I_o} = \frac{1}{2}\frac{\mu_o N^2 L_m W_m I_o^2}{z_o^3}\left(1 + 2\frac{z_o}{\pi W_m}\right) - \frac{\mu_o N^2 L_m I_o^2}{2\pi z_o^2} \tag{2.12}$$

$$k_i = \left.\frac{\partial F_z}{\partial I}\right|_{z_o, I_o} = \frac{1}{2}\frac{\mu_o N^2 L_m W_m I_o}{z_o^2}\left(1 + 2\frac{z_o}{\pi W_m}\right) \tag{2.13}$$

The coefficient k_z in Eq. (2.12) can be considered as the suspension's stiffness and it is fundamentally negative due to the variation of force with gap. This is the negative spring that was mentioned in [14], which is originally nonlinear.

So, the state space model of the linear system can be written as follows [2,7,9]:

$$\begin{bmatrix}\dot{z}\\ \ddot{z}\\ \dot{I}\end{bmatrix} = \begin{bmatrix}0 & 1 & 0\\ k_z/m & 0 & -k_i/m\\ 0 & k_z/k_i & -(K_A+R)/L\end{bmatrix}\begin{bmatrix}z\\ \dot{z}\\ I\end{bmatrix} + \begin{bmatrix}0\\ 0\\ K_A/L\end{bmatrix} I_c \tag{2.14}$$

$$[z] = [1 \quad 0 \quad 0]\begin{bmatrix}z\\ \dot{z}\\ I\end{bmatrix} \tag{2.15}$$

where Eqs. (2.14) and (2.15) are the state equation and the output equation, respectively with:

$$A=\begin{bmatrix} 0 & 1 & 0 \\ k_z/m & 0 & -k_i/m \\ 0 & k_z/k_i & -(K_A+R)/L \end{bmatrix};\ B=\begin{bmatrix} 0 \\ 0 \\ K_A/L \end{bmatrix};C=\begin{bmatrix} 1 & 0 & 0 \end{bmatrix};\text{ and } D=0$$

representing the dynamics, input, output and throughput matrices, respectively.

The system transfer function will be:

$$G(s)=C(sI-A)^{-1}B+D\cong\frac{-K_x}{(s-\omega_m)(s+\omega_m)(s+\alpha)}=\frac{-K_x}{(s^2-\omega_m^2)(s+\alpha)} \tag{2.16}$$

where,

$$K_x=K_A\frac{k_i}{L} \tag{2.17}$$

$$\alpha=\frac{K_A+R}{L} \tag{2.18}$$

$$\omega_m\cong\sqrt{\frac{k_z}{m}} \tag{2.19}$$

The system has three real poles. One is positive, which indicates the inherent instability of the EMS Maglev systems. The pole α is the electrical (or electrodynamics) pole. The pair $\pm\,\omega_m$ represents the mechanical poles. ω_m can be considered as the unstable natural frequency of the mechanical subsystem. The value of ω_m can vary significantly with the system air gap and current as it depends on k_z (Eq. (2.12)). Figure 2.6 shows the pole-zero map of the single axis EMS Maglev system, open loop.

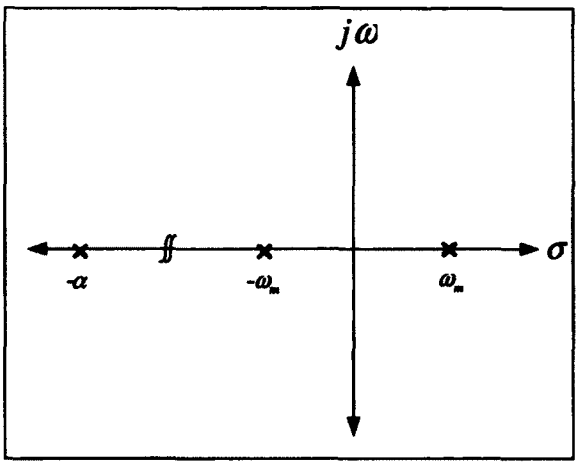

Figure 2.6. Pole-Zero Map of the Single Axis EMS Maglev System, Open Loop

The basic open loop block diagram of the single axis EMS Maglev system can be drawn based on the state space model in Eqs. (2.14) and (2.15) as shown in Figure 2.7.

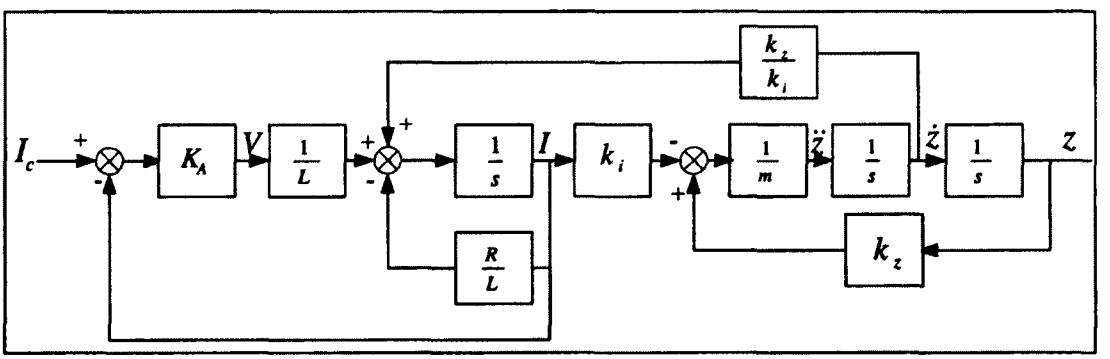

Figure 2.7. Block Diagram of a Single Axis Maglev Rigid System

2.3 Two DOF Maglev system with an inverted U-rail

The system that is under consideration is composed of two magnets that are placed under an inverted U-rail. If it is assumed that the rail widths are large enough compared to the air gap, and it is assumed that the magnet's lateral displacement is small enough so

that a part of uniform field exists in the air gap, then each magnet-rail pole corner pair can be treated independently.

The U-shaped rails produce the required levitation, while the lateral forces are generated by the fringing fields [11-12]. In reality, the electromagnetic flux fringing fields occur around electromagnet poles [2][11][47]. In Figure 2.8, magnetic field models for U shaped magnets; a) uniform, b) with fringing shown.

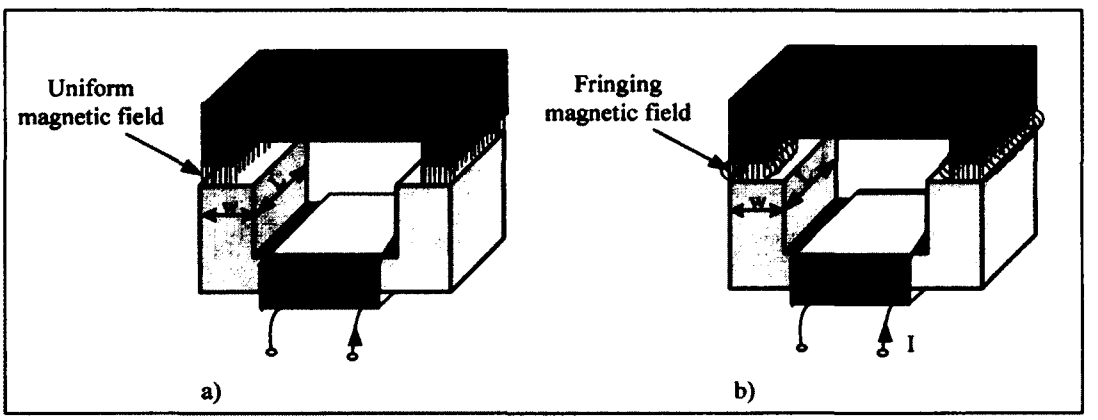

Figure 2.8. Magnetic Field Models for U-Shaped Magnets, a) Uniform, b) with Fringing

The magnetic fields and forces that can be generated are calculated using conformal mapping techniques [11] and the resulting vertical and lateral forces closed form expressions are, respectively:

$$F_z = \frac{\mu_o N^2 I^2 L_m W_m}{4z^2} \rho(y,z) \tag{2.20}$$

$$F_y = \frac{\mu_o N^2 I^2 L_m W_m}{4z^2} \varepsilon(y,z) \tag{2.21}$$

where,

$$\rho(y,z)=1+\frac{2}{\pi}\frac{z}{W_m}\left(1-\frac{y}{z}\tan^{-1}\frac{y}{z}\right) \quad \varepsilon(y,z)=\frac{2}{\pi}\frac{z}{W_m}\tan^{-1}\frac{y}{z},$$

where, I : is the coil current, z : is the air gap and y : is the lateral displacement.

It is clearly noted from Eq. (2.20), that *the levitation force is unstable with respect to the air gap z when I is constant, and it is inversely proportional to the air gap*; hence, active control is required for stabilization. On the other hand, from Eq. (2.21), *lateral force is proportional with respect to the lateral displacement y and is stable.*

The expressions of the levitation and lateral forces that in Eqs. (2.20) and (2.21) are plotted numerically, as shown in Figure 2.9.

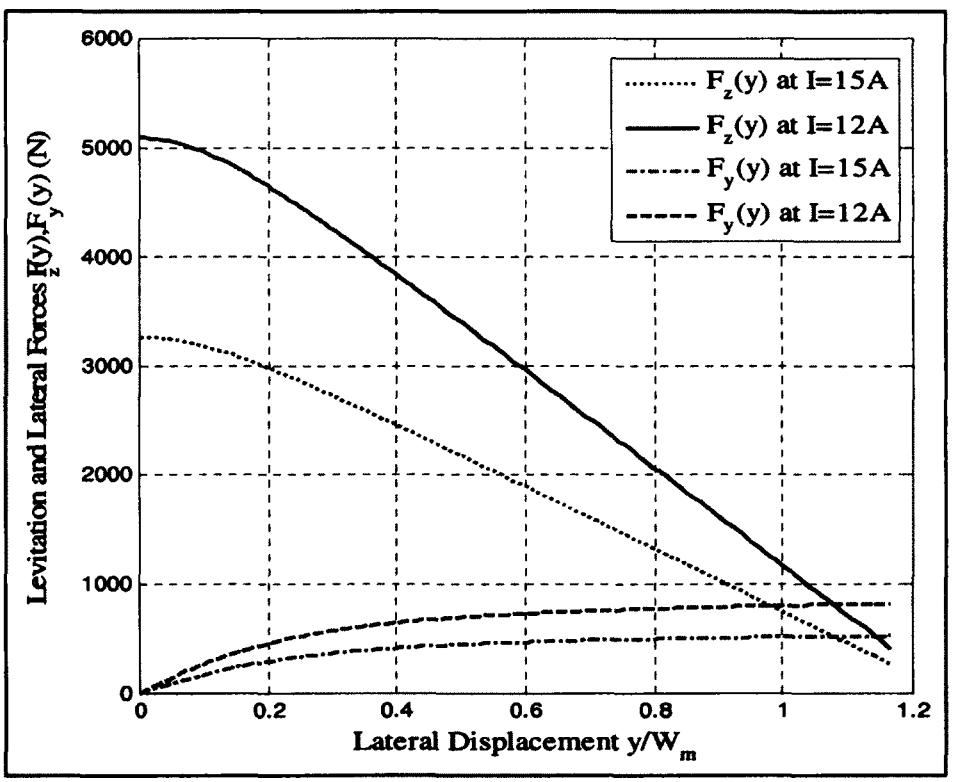

Figure 2.9. Single Magnet Levitation and Lateral Forces vs Lateral Displacement at Constant Current

In Figure 2.9, the forces are plotted at some specific conditions of: constant currents (12, and 15A), nominal air gap, and versus normalized lateral displacement.

2.3.1 Model for a Staggered Pair. Rigid Case

The arrangement of the two magnets that are used in the 2-DOF EMS Maglev system is shown. Figures 2.10-2.12 show two electromagnets that are staggered under an inverted-U rail.

Each magnet is supplied by individual currents I_1, and I_2 to support a vehicle of mass M. It is required that this configuration is able not only to support the vehicle weight, but also to damp the lateral displacements due to lateral disturbing forces as wind gusts.

"Heave stability is attained by increasing both magnet currents with increasing air gap, while the suspension's lateral force is adjusted by increasing the current in one magnet, and decreasing that in the other, as functions of the vehicle's lateral motion" [10].

An important assumption for modeling is to regard the suspension as interacting with the rail at a single point. This assumption renders heave and lateral motions as possible motions.

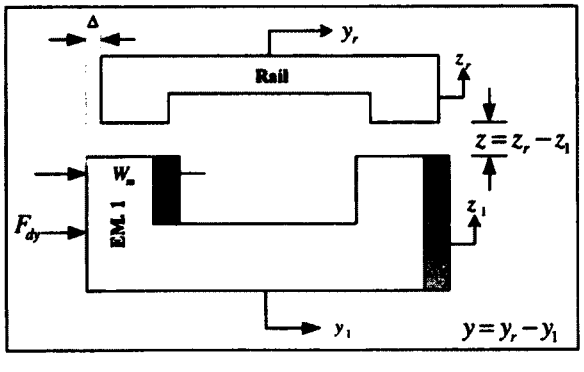

Figure 2.10. Two Staggered Magnets Configuration

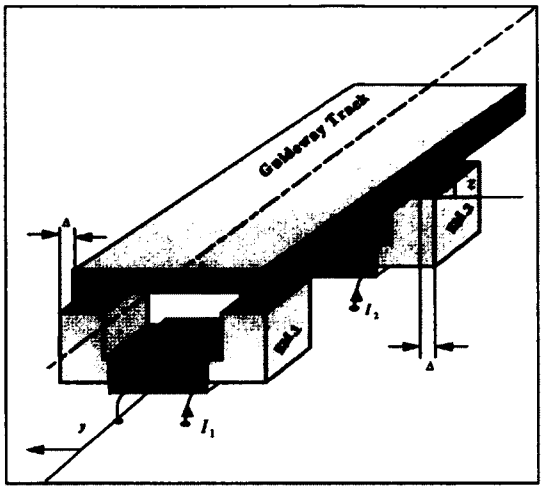

Figure 2.11. Two Staggered Magnets Configuration in 3D

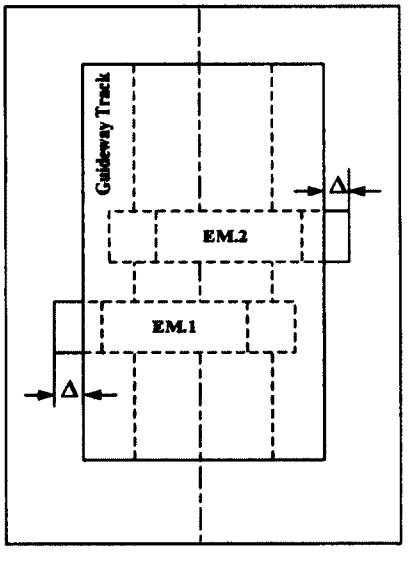

Figure 2.12. Two Staggered Magnets Configuration Plan View

In Figure 2.10, z_r, and y_r are the displacements relative to rail in vertical and lateral directions, respectively; z_1, and y_1 are the absolute vertical and lateral positions, respectively. Then the air gap $z = z_r - z_1$, and the relative magnet-rail displacement is $y = y_r - y_1$.

The coupled nonlinear expressions of the levitation and lateral forces are:

$$F_z = F_{z1} + F_{z2} = \frac{\mu_o N^2 I_1^2 Lw}{4z^2}\rho(\Delta - y, z) + \frac{\mu_o N^2 I_2^2 Lw}{4z^2}\rho(\Delta + y, z) \tag{2.22}$$

$$F_y = -F_{y_1} + F_{y2} = -\frac{\mu_o N^2 I_1^2 Lw}{4z^2}\varepsilon(\Delta - y, z) + \frac{\mu_o N^2 I_2^2 Lw}{4z^2}\varepsilon(\Delta + y, z) \tag{2.23}$$

The system equations are formed by applying Newton's second law

$$M\ddot{z} = -F_z + Mg \tag{2.24}$$

$$M\ddot{y} = F_y + F_{dy} \tag{2.25}$$

where,

F_{dy}: is the disturbing force in y-axis direction and g: is the gravitational constant.

2.3.2 Model for a Staggered Pair. Flexible Case

The dynamic model of the EMS Maglev vehicle in practice includes rigid body and structural vibration modes [3]. The mode shapes (eigenvectors) and natural frequencies of vibration (eigenvalues) of the Maglev vehicle for selected modes are always found from a finite element model. The system entire flexible modes can be modeled by many methods; one of the most suitable ways is the finite element method. The idea behind the finite element method is to provide a formulation which can exploit digital computer for the analysis of irregular systems. It divides a continuous subsystem into a number of elements using fictitious dividing lines. The points of intersection of dividing lines are referred to as "nodes" or "joints". Each joint has a certain number (up to six) of Degrees of Freedom (DOF) [48]. A Lagrangian formulation is usually applied wherein the node forces are determined as functions of the adjacent elements. Then, the problem is reduced to the eigenvalue problem that can be solved using standard numerical techniques.

The flexible body case can be attained by adding one flexible mode that appears when a secondary mass is attached to the system primary mass with a spring and damper as shown in Figure 2.13.

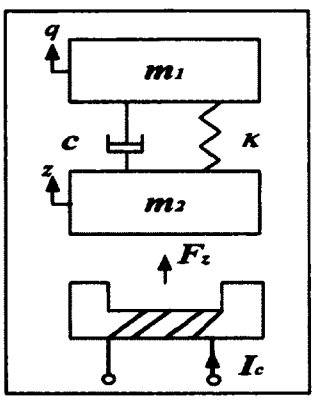

Figure 2.13. Simple Model of a Flexible Maglev System

where, c is the damping coefficient, κ is the stiffness coefficient, m_1 is the secondary mass, m_2 is the primary mass and I_c is the command current.

If point forces and torques are applied at each node, the final "modal" model has the form

$$\ddot{q}(t) + \eta q(t) = \gamma^T f(t) \tag{2.26}$$

$$y(t) = \Gamma q(t) \tag{2.27}$$

where q is the $n\times1$ modal amplitude vector, Γ is the $n\times n$ generalized mode-shape matrix, f is the vector of generalized applied forces (levitation forces), $\eta = diag(\omega_1^2, \omega_2^2, ...\omega_n^2)$,and y is the $n\times1$ displacement vector. The finite element method gives the rigid and the flexible modes. Thus $q(t)$ in Eq. (2.26) includes also the zero-frequency modes. It is more convenient to use only the flexible segment of the finite element model, and to augment it

with the rigid body equations Eqs. (2.26, and 2.27) that are obtained separately. In order to make Eq. (2.26) more general, inherent structural damping should be included by adding damping terms (after eigenvalues problem has been solved), therefore

$$\ddot{q}(t) + \chi\dot{q}(t) + \eta q(t) = \gamma^T f(t) \tag{2.28}$$

where,

$$\chi = 2diag\,(\varsigma_1\omega_1, \varsigma_2\omega_2, \ldots, \varsigma_n\omega_n)$$

where ς_i and ω_i, $i=1,2,\ldots n$ is the inherent damping ratio and natural frequency of the i^{th} flexible mode. For large flexible space structures ς_i are typically on the order of 0.001-0.01. The structural damping can be assumed herein to equal 0.01[48].

2.3.3 Electrodynamics

In this section, a unified model for the electromagnet electrodynamics is illustrated. The instantaneous magnet permeance in terms of y and z [12] is:

$$P(y,z) = \frac{\mu_o Lw}{2z}\left\{1 + \frac{2z}{\pi w}\left[1 + \frac{1}{2}\ln\left(1 + \left(\frac{y}{z}\right)^2\right) - \frac{y}{z}\tan^{-1}\frac{y}{z}\right]\right\} \tag{2.29}$$

Then, the magnet inductance in terms of y and z is found from the relationship with the magnet permeance as [12]:

$$L_m(y,z) = N^2 P(y,z) \tag{2.30}$$

or,

$$L_m(y,z) = \frac{\mu_o N^2 Lw}{2z}\left\{1 + \frac{2z}{\pi w}\left[1 + \frac{1}{2}\ln\left(1 + \left(\frac{y}{z}\right)^2\right) - \frac{y}{z}\tan^{-1}\frac{y}{z}\right]\right\} \tag{2.31}$$

The voltage applied to the coil of each electromagnet is

$$V = RI + L_m(y,z)\frac{dI}{dt} - L_m(y,z)\frac{I}{z}\frac{dz}{dt} \tag{2.32}$$

The electromagnets are driven by current amplifiers intended to track a current command I_c with an amplifier feedback gain K_A.

$$V = K_A(I_c - I) \tag{2.33}$$

The final current loop is

$$\dot{I} = \frac{K_A}{L_m}(I_c - I) - \frac{RI}{L_m} - \frac{I\dot{z}}{z} \tag{2.34}$$

Eq. (2.34) to be used for each electromagnet (using subscripts 1 and 2 for each electromagnet's current) as there are two of them. Combining Eqs. (2.24), (2.25), and Eq. (2.34) (one for each electromagnet), a six state nonlinear model for the system rigid case is constructed:

$$\dot{x} = f(x,u) = [f_1 \quad \cdots \quad f_6]^T$$
$$x^T = [z \quad \dot{z} \quad y \quad \dot{y} \quad I_1 \quad I_2]^T$$

$$f_1 = \dot{z} \qquad f_2 = -\frac{F_z}{M} + g \tag{2.35}$$
$$f_3 = \dot{y} \qquad f_4 = \frac{F_y}{M} + \frac{F_{d_y}}{M}$$
$$f_5 = \beta I_{c1} - \alpha I_1 + \frac{I_1\dot{z}}{z} \qquad f_6 = \beta I_{c2} - \alpha I_2 + \frac{I_2\dot{z}}{z}$$

where

$\alpha = \frac{K_a + R}{L_m}$, and $\beta = \frac{K_a}{L_m}$

If adding Eq. (2.28) to the previous system of equations, an eight state nonlinear model for the system case is established:

$$\dot{x} = f(x,u) = [f_1 \quad \cdots \quad f_8]^T$$
$$x^T = [z \quad \dot{z} \quad y \quad \dot{y} \quad I_1 \quad I_2 \quad q_1 \quad \dot{q}_1]^T$$

$$\begin{aligned} f_1 &= \dot{z} & f_2 &= -\frac{F_z}{m_2} + \frac{m}{m_2}g + \frac{\kappa}{m_2}(q_1 - z) + \frac{c}{m_2}(\dot{q}_1 - \dot{z}) \\ f_3 &= \dot{y} & f_4 &= \frac{F_y}{m} + \frac{F_{d_y}}{m} \\ f_5 &= \beta I_{c1} - \alpha I_1 + \frac{I_1 \dot{z}}{z} & f_6 &= \beta I_{c2} - \alpha I_2 + \frac{I_2 \dot{z}}{z} \\ f_7 &= \dot{q}_1 \\ f_8 &= \frac{\kappa}{m_1}(z - q_1) + \frac{c}{m_1}(\dot{z} - \dot{q}_1) \end{aligned} \tag{2.36}$$

where total mass $m=m_1+m_2$

It should be noted that both rigid and flexible cases of the 2-DOF EMS Maglev system are unstable. The instability is in the heave channel as described in Eq. (2.20). Further investigation on this model will be introduced in the next chapter.

2.3.4 Static Characteristics of a Staggered Magnet Pair

In this section, the static characteristics of a staggered magnet pair are studied. It is well known that the staggered magnet design has considerable lateral force capabilities. The effects of stagger separation Δ on the vertical and lateral force characteristics are shown in Figure 2.13 (in 2D format. In Figure 2.14, force normalization is at levitation force of $\Delta = 0$ and y=0).

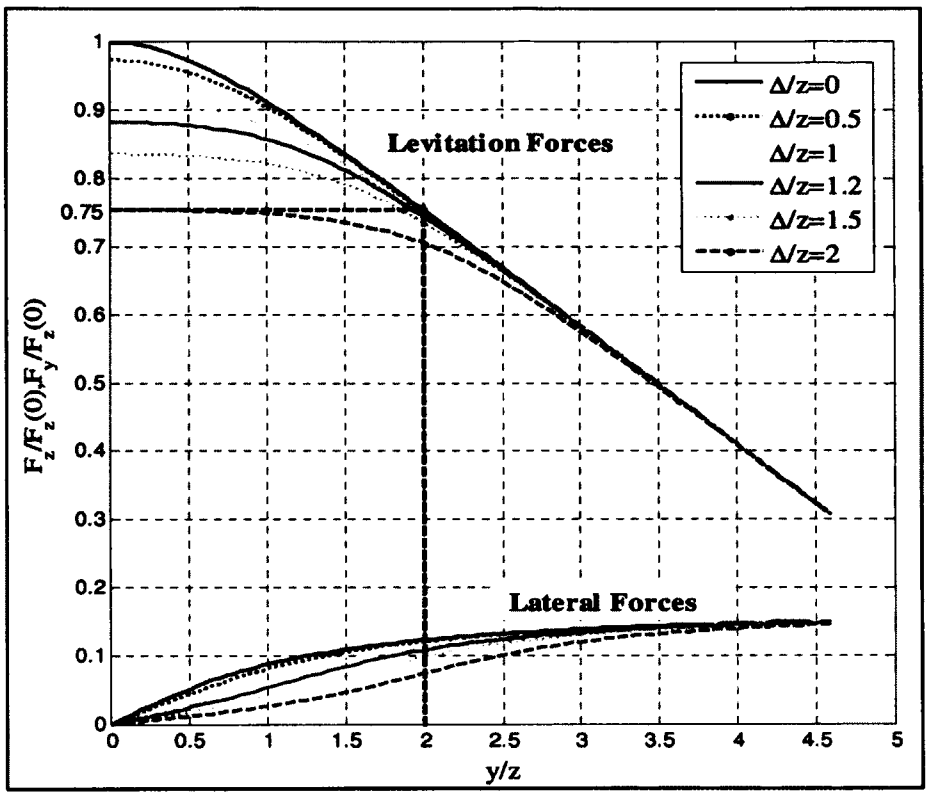

Figure 2.14. Levitation and Lateral Forces vs Lateral Displacement for Various Stagger Separations

The curves received in this section are normalized with respect to the levitation force at zero lateral displacement "y"; considering equal constant currents, $I_1 = I_2$; constant gap; and the ratio between L_m/z=3.8. These results show that the maximum lateral force for $I_1 = I_2$ does not change significantly as Δ is changing over a wide range. At Δ=0, the levitation force decreases rapidly while the lateral force increases rapidly towards its maximum, as the magnet set is displaced laterally [10]. The staggering of the magnets reduces the levitation force considerably up to 25% for $\Delta / z = 2$ at $y = 0$ as shown in Figure 2.13, which may affect the system levitation if the controller design does not tolerate this force reduction. For large Δ, the levitation force remains essentially constant

over a good range of lateral displacements. Staggering has more influence on the levitation forces than the lateral forces due to higher coupling found for the levitation forces compared to the lateral forces as observed in Eqs. (2.20) and (2.21). The Maclaurin expansion of the trigonometric function $\tan^{-1}(\_)$ that relates the staggering distance with the levitation and lateral forces is

$$\tan^{-1}(x) \cong x - \frac{1}{3}x^3 + \frac{1}{5}x^5 - \frac{1}{7}x^7 - \ldots\ldots \tag{2.37}$$

If the higher terms are ignored, the relation between the lateral forces of a staggered magnets pair and the terms $\frac{\Delta + y}{z}$ and $\frac{\Delta - y}{z}$ will approximately vanish as the stagger Δ in the first term and second term will cancel each other out. The relation between the levitation forces of a staggered magnets pair considering the terms $\frac{\Delta + y}{z}$ and $\frac{\Delta - y}{z}$ will be approximated as a nonlinear function of $2(\Delta^2+y^2)/z$. This could be the reason of having this big difference in the levitation force versus the lateral force with the staggering distance.

The extension of the levitation and lateral forces plots of Figure 2.13 are shown in Figures 2.15, and 16 but in a 3D format.

The decision on which stagger distance to be used can be deduced from the intersection of $\frac{y}{z} = 2$ with the normalized levitation force at 0.75 as in Figure 2.14. This corresponds to a stagger distance of $\Delta \leq 1.2z$ for the magnet pair used for this 2-DOF EMS Maglev system. This result can be generalized to determine stagger distances for the ODU Maglev system magnets.

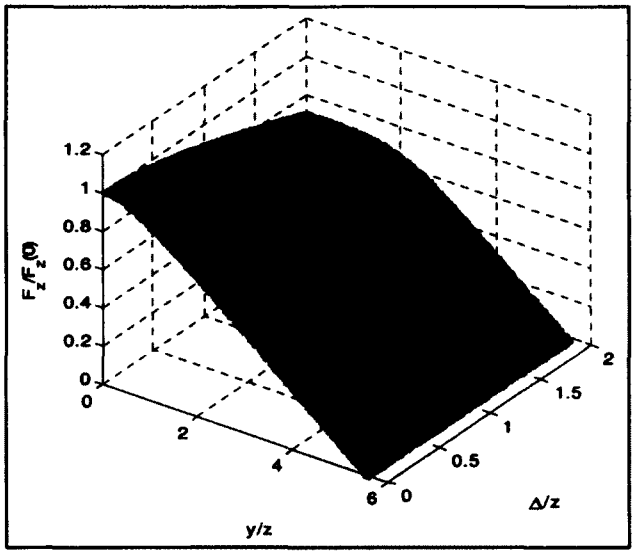

Figure 2.15. Levitation Forces vs Lateral Displacement for Various Stagger Separations-3D

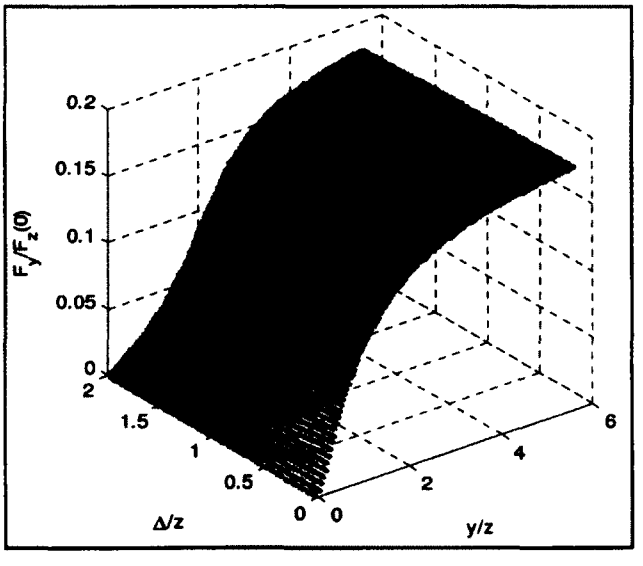

Figure 2.16. Lateral Forces vs Lateral Displacement for Various Stagger Separations-3D

2.4 System Coupling Measures

2.4.1 Relative Gain Array (RGA)

Interaction existing between the control loops causes the manipulated variable in one loop to influence the controlled variable in the other loop. A technique called the Relative Gain Array (RGA) has been used to analyze the interaction between different control loops.

The RGA is of a non-singular square complex matrix G is a square complex matrix defined as [41]:

$$RGA(G) = G \times (G^{-1})^T \tag{2.38}$$

where $\times$ is the Schur product.

The relative gain of a controlled variable i to a manipulated variable j is defined *as*

$$\lambda_{ij} = \frac{\text{gain with the other loops open}}{\text{gain with the other loops closed}} \tag{2.39}$$

where the concept of a closed loop is that the output of a loop is always at its set point whatever happens to try to change it. The mathematical expression can be

$$\lambda_{ij} = \frac{\left(\frac{\partial y_i}{\partial u_j}\right)_{u_k=0,k\neq j}}{\left(\frac{\partial y_i}{\partial u_j}\right)_{y_k=0,k\neq i}} = \frac{g_{ij}}{\hat{g}_{ij}} \tag{2.40}$$

Here $g_{ij} = [G]_{ij}$ is the ij'th element of G, whereas $\hat{g}_{ij}$ is the inverse of the ji'th element of G^{-1}. The definition of relative gain indicates that its purpose is to measure how much the gain of one loop changes when the other loops in an interacting system are closed.

A special case to be noticed when a two-input-two-output system (TITO) is considered. A 2×2 matrix with elements g_{ij},the RGA is [41]:

$$RGA(G)=\begin{bmatrix}\lambda_{11} & \lambda_{12}\\ \lambda_{21} & \lambda_{22}\end{bmatrix}=\begin{bmatrix}\lambda_{11} & 1-\lambda_{11}\\ 1-\lambda_{11} & \lambda_{11}\end{bmatrix};\ \lambda_{11}=\frac{1}{1-\frac{g_{12}g_{21}}{g_{11}g_{22}}} \tag{2.41}$$

The RGA of a TITO system as in Eq.(2.38) indicates that the interaction between direct channels is the same (u_1-y_1, u_2-y_2), and for the cross channels is also the same (u_1-y_2,u_2-y_1).

Some notes on RGA are necessarily provided. The RGA is a direct measure of the steady state control effort required to overcome interaction conflict effects [49]. The RGA is dimensionless and invariant under any single variable transformation. The dynamic extension of RGA can be achieved by plotting RGA(s) versus s or with frequency $j\omega$ to show the interaction over wide range of frequency [50].

2.4.2 Coupling Factor

The coupling factor κ_o is determined by finding the ratio between the product of non-diagonal steady state gains and the product of the diagonal gains [51]. For a TITO system, the coupling factor is:

$$\kappa_o=\frac{K_{12}K_{21}}{K_{11}K_{22}} \tag{2.42}$$

where, K_{ij} is the steady state gains (DC gains) of g_{ij}.

The type of coupling is defined by:

$\kappa_o<0$: negative coupling

$\kappa_o>0$: positive coupling

From the viewpoint of stability, a control system needs to be reconfigured if $|\kappa_o|>>1$ [51].

2.4.3 Niederlinski Index

Niederlinski [52] invented a rule that can be utilized to determine the proper input-output pairing for a multivariable system that is under control. The pairing rule gives a clear indication for *minimum interaction*; it is often necessary to utilize this rule in conjunction with stability considerations provided by the following theorem originally given by Niederlinski:

Theorem 2.1 Consider an $n\times n$ multivariable system whose manipulated and controlled variables have been paired as follows: y_1-u_1,y_2-u_2,...y_n-u_n , resulting in a transfer function model of the form [51]:

$$y(s)=G(s)u(s) \tag{2.43}$$

Let each element of $G(s)$, $g_{ij}(s)$ be rational and n individual feedback controllers (which has *integral action I, PI, PID*) be designed for each loop so that each one of the resulting n feedback control loops is stable when all other n-1 loops are open. Then, under closed loop conditions in all n loops, the multiloop system will be unstable for all possible values of controller parameters (i.e. it will be structurally monotonically unstable) if Niederlinski's index (NI) defined below is negative:

$$NI=\frac{\det[G(0)]}{\Pi_{i=1}^{n} g_{ii}(0)}<0 \tag{2.44}$$

Eq. (2.44) is necessary and sufficient only for 2×2 systems, but for higher dimensional systems, it provides only sufficient conditions, i.e. if Eq. (2.44) holds, then the system is definitely unstable; otherwise, the system may not be unstable because the stability will, in this case, depend on the values taken of the controller parameters.

2.5 Generalized Multi-Input Multi Output Root Loci

The root locus technique provide with much insight into the problem. It not only enables the designer to select the proper controller dynamics that may attain the required performance but also can be used to achieve insensitivity of the system to large parameter uncertainty [53]. The generalized MIMO root loci can be regarded as an extension of scalar-loop concepts, as opposed to earlier efforts which introduce eigen-based concepts [54]. Recalling the sketching rules of root locus associated with scalar-loop applications are to transform the Evans design technique from a iterative strategy to a powerful tool where clear and brief relationships between design inputs and resulting effects upon stability and performance are available [55]. The modern mathematical programs can be used to find the roots of closed-loop MIMO systems easily, and at any dimension. Then, drawing the root loci corresponding to any system parameter change is possible. The earlier research in this field is valuable to understand, explain and justify the behavior of the multivariable root loci, but not for practical utilization [56]. A simple method that can be used to sketch the MIMO root loci based on the traditional method on which the eigenvalues of the closed loop system are allowed to be changed by increasing a scalar gain k that is associated with the designed controller and sketching their change starting from the location of the system open loop eigenvalues ($k=0$) till the end ($k=\infty$) or in other words, to establish the root loci of the MIMO system as the scalar gain is changing from zero to infinity [56]. The method can be used with the simple MIMO systems, and it is based on the state space representation in order to avoid the numerical errors that may be encountered with the transfer function representations.

The MIMO root loci technique is a useful technique in the design process of a multivariable controller, and it enables a check of the multivariable gain margin on which the system can tolerate any gain variations [57]. A general linear MIMO system is shown in Figure 2.17.

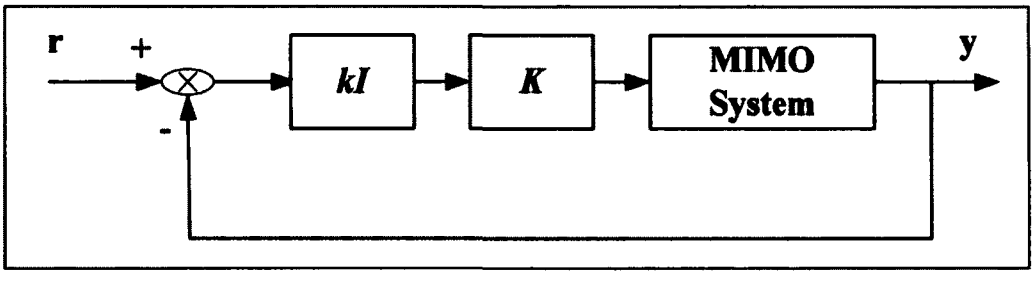

Figure 2.17. MIMO Control System

where, r is the command input, y is the system output, k is the scalar gain and I is the identity matrix.

The state space system with the controller in a closed loop form (output feedback) can be easily found as follows:

$$A_{cl} = A - kBCK \tag{2.45}$$

where, A_{cl} is the closed loop dynamics matrix, and K is the controller. The eigenvalues of the closed loop system can be found by finding the roots of the following characteristic equation:

$$sI - A_{cl} = 0 \tag{2.46}$$

where, s is the Laplace operator.

The system open loop eigenvalues (starting point) can be easily found by exchanging the matrix A_{cl} in Eq. (2.45) by the matrix A.

2.6 Methods for Multivariable PID Controller Gains Selection

In this section, some methods that can be used to select the multivariable PID controllers' gains are received. The methods that are mentioned in this section include: auto tuning technique, characteristic locus design method, optimization method, and trial and error method. Other methods of tuning multivariable PID controllers' gains include intelligent techniques like genetic, fuzzy, neural, or combinations that are not included in this section.

2.6.1 Auto Tuning Technique

2.6.1.1 Generalized Ziegler-Nichols Method

The Ziegler-Nichols design method is a very popular heuristic method used in process control to determine PID controller parameters for SISO systems. Niederlinski extended this method to a multivariable system [52] which also utilizes the critical frequency and critical gain to determine parameters of diagonal PID controllers. The generalized Ziegler-Nichols method procedure for tuning of PI or PID control of MIMO system is described below [52][58], assuming the system is of the best pairing configuration [59].

i. Choose n weighting factors w_i ($i = 1, ...n$) for the relative control quality of the n controlled variable.

ii. Use the best input-output pairing configuration, and then bring the P-controlled system to a stable oscillation while the following relations between loops are kept:

$$\frac{K_{c.i}G_{ii}(0)}{K_{c.i+1}G_{i+1,i+1}(0)} = \frac{w_i}{w_{i+1}},\ i = 1, ...n\text{-}1 \tag{2.47}$$

where, $K_{c.i}$ is the gain of P-controller, and determine the corresponding critical loop gain K_{cr}.

iii. Evaluate the critical frequency Ω_{cr} and the critical controller gain $K_{c.i.cr}$, for the given system.

iv. Determine the controller parameters by the generalized Ziegler-Nichols tuning formula listed in Table 2.1 where the choice of the coefficient α_i depends on the ratio $\alpha_i = \dfrac{\Omega_{cr}}{\omega_{i.c}}$.

where, $\omega_{i.c}$ is the critical frequency of the P-Controlled single variable system of $G_{ii}(s)$.

Table 2.1 Generalized Ziegler-Nichols Tuning Rules

Controller	Parameters of PID controller		
	K_p	τ_i	τ_d
P	$\alpha_1 K_{c.i.cr}$	-	-
PI	$\alpha_2 K_{c.i.cr}$	$0.8T_{cr}$	-
PID	$\alpha_3 K_{c.i.cr}$	$0.5T_{cr}$	$0.12T_{cr}$
where $T_{cr} = \dfrac{2\pi}{\Omega_{cr}}$ $0.5 \le \alpha_1 \le \sqrt{0.5}$ $0.45 \le \alpha_2 \le \sqrt{0.45}$ $0.6 \le \alpha_3 \le \sqrt{0.6}$			

where, the integral time and derivative time are τ_i ,and τ_d, respectively.

If $\alpha_i << 1$ a large controller gain can be selected; if α_i is near to one the controller gain should be at the lower limit value.

v. Check whether the relative control quality is satisfactory. If not, change w_i appropriately and return to step 2.

2.6.1.2 Automatic Tuning PID Controller

To use the generalized Ziegler-Nichols tuning formula to determine PID controller parameters, it is necessary to find the critical frequency Ω_c and critical gain $K_{c.i.cr}$ of a multivariable control system. In the design method proposed by Niederlinski, proportional controllers are introduced in each loop to obtain a stable oscillation by increasing the controller gains [59].

The concept of Relay feedback can be used to tune the multivariable PID controller gains. The relay feedback can be used to determine the critical frequency Ω_c and critical gain $K_{c.i.cr}$. In [60], three possible relay feedback schemes for MIMO system were presented:

i. Independent single-relay feedback (IRF), in which one loop at a time is subjected to relay feedback while all other loops are open.
ii. Sequential relay feedback (SRF), in which a loop is closed with a simple controller once a relay test is performed to that loop and repeat this until all loops are checked.
iii. De-centralized relay feedback (DRF), in which all loops are on relay feedback at the same time.

DRF is more desirable as it is a complete closed loop test while IRF and SRF are only partial closed loop tests. Figure 2.18 shows the de-centralized relay test.

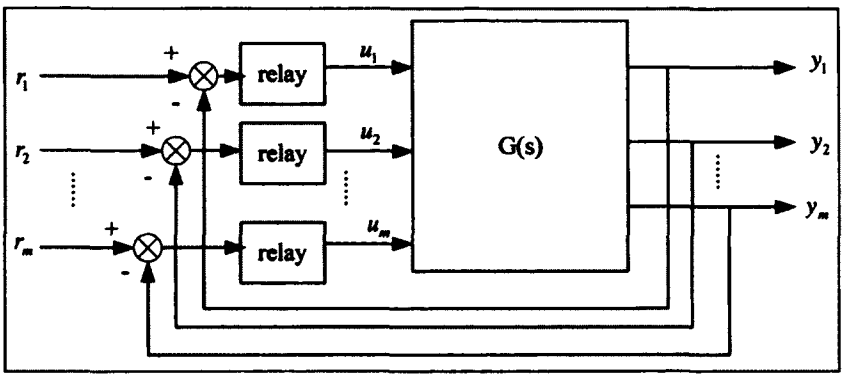

Figure 2.18. De-centralized Relay Test

2.6.2 Characteristic Locus Design Method

The idea of plotting characteristic (eigen) loci of the open-loop transfer function matrix is useful because it allows for checking the closed-loop stability for a MIMO feedback system by inspection [61-63].

The principle of the design method is to modify the gain and phase of the desired characteristic loci to achieve the required stability and to obtain a good closed loop system performance [59]. This method can be used to determine the PID controller parameters automatically so that the auto tuning procedure can be executed for the MIMO process without prior knowledge of the process [59]. Assuming the process is open loop stable, the critical frequency and the critical gains are Ω_c, K_{c1}, K_{c2}, ..,K_{ci}, and that the diagonal PID controller to be developed has the following transfer matrix,

$$G_c(s)=\begin{bmatrix} K_{p_1}\left(1+\frac{1}{\tau_{i_1}s}+\tau_{d_1}s\right) & 0 & \cdots & 0 \\ 0 & K_{p_2}\left(1+\frac{1}{\tau_{i_2}s}+\tau_{d_2}s\right) & \cdots & 0 \\ 0 & 0 & \cdots & 0 \\ 0 & 0 & \cdots & K_{p_i}\left(1+\frac{1}{\tau_{i_i}s}+\tau_{d_i}s\right) \end{bmatrix} \tag{2.48}$$

then the required magnitude m and argument ϕ of a specific characteristic locus at the frequency Ω_c to be attained by setting the PID parameters to be:

$$\begin{aligned} \Omega_c \tau_{d_i} - \frac{1}{\Omega_c \tau_{i_i}} &= \tan\phi \\ \left| G(j\Omega_c) G_c(j\Omega_c) \right| &= m \end{aligned} \tag{2.49}$$

Taking $\tau_{i_i} = \delta \tau_{d_i}$, then the following is obtained

$$\begin{aligned} \tau_{d_i} &= \frac{\tan(\phi) + \sqrt{4/\delta + \tan^2(\phi)}}{2\Omega_c} \\ \tau_{i_i} &= \delta \tau_{d_i} \\ K_{p_i} &= K_{c_i} \cos(\phi) m \end{aligned} \tag{2.50}$$

where, the subscript i indicates the controller in loop i and τ_i and τ_d are independent of i. By designing $G_c(s)$ with the parameters obtained from Eq. (2.50), the characteristic loci of the process with larger magnitude can be changed to any desired location at a critical frequency so that the gain or phase margin of the compensated characteristic loci can satisfy a desired condition.

2.6.3 Optimization Method

Optimal PID controller gains can be attained by optimizing certain integral performance indices. For SISO systems, the ISE criterion was commonly used to tune PID controllers. This criterion can be extended to tune diagonal PID controllers for multivariable systems.

2.6.3.1 Design PID Controllers for Uncoupled Systems

The interaction between loops determines how to design and select the PID controller gains. If there is a small interaction between loops, then an individual PID controller can be designed for each loop separately as for a SISO process. The

multivariable transfer matrix should be represented as a diagonal matrix and the off diagonal transfer functions are zero. This concept was first applied on a TITO system and can be generalized for MIMO system [59].

This method is still valid to design PID controller for each channel individually with re-tuning of the PID controllers' gains when all loops of the multivariable system with the controllers are closed to achieve the desired performance.

Another method can be utilized to design PID controllers by minimizing an error function for the whole system using integral performance index. This method was successfully applied on a TITO system [59] by defining return difference matrix:

$$E(s) = R(s) - Y(s) = (1 + G(s)G_c(s))^{-1} R(s) \tag{2.51}$$

The integral performance index to be minimized is:

$$J = \int_0^\infty F(e_{ii})dt \tag{2.52}$$

with the constraint

$$g_1 = \int_0^\infty F(y_{ji})dt < C \qquad i \neq j \tag{2.53}$$

where e_{ii} is an error signal in the loop i, y_{ij} is the output in the loop j. The following objective function can be utilized:

$$g_2 = \int_0^\infty \{\vartheta_1 F(e_{ii}) + \vartheta_2 F(y_{ij})\}dt \tag{2.54}$$

where, ϑ_i is the a weighting factor. There are various criteria that can be chosen for optimization.

2.6.3.2 Designing PID Controllers using Decoupling Technique

If there is severe interaction between loops, then the previous method will fail as the interaction between loops may destabilize the system, and then a decoupling technique can be used. The concept of decoupling techniques for multivariable control systems is introduced in many papers [59,41,65,66]. The idea of decoupling uses state variable feedback in which class of all feedback matrices which decouple the system are determined.

In [65], it was stated that some multivariable systems can be decoupled if they verify certain conditions otherwise; the decoupling matrices could not be found. The choice of the decoupling matrix may not be an easy task since it is related to the plant characteristics and the controller structure. Sometimes, the design leads to a higher-order or unrealizable decoupler [66].

After decoupling the system, the interaction between loops is eliminated and the modified system becomes n individual single variable system.

2.6.4 Trial and Error Method

The trial and error method can be used to tune the PID controller gains [67-69]. In practice, human knowledge can be used to develop PID controllers with good performance by trial and error. In [67], the PID controller was manually tuned through trial and error for a plant with under damped step response. Trial and error method is used to tune the PID controller gains from critical frequency Ω_c and critical gain $K_{c.i.cr}$ of a multivariable control system [68]. A trial and error procedure was used to determine sets of parameters (including controller gain, integral time and derivative time) which achieve satisfactory response of a PID controller over a nonlinear process [69]. Trial and

error method is time consuming and it is preferable to have good knowledge and background on the system that is under control, e.g. for EMS Maglev systems, the proportional control gain value K_p should be greater than the derivative control gain value K_d ($|K_p|>|K_d|$) [2,4].

2.7 EMS Maglev PID Control Schemes

Two common control schemes are used to control multivariable systems. These schemes are typically de-centralized (local) control, and centralized (modal or integrated) control. In the following subsections they are briefly described.

2.7.1 De-centralized Control Scheme

The idea behind de-centralized (local) control is that controllers are designed locally for each input-output pair, as shown in Figure 2.20. De-centralized control means that each input-output pair has its own control loop that is independent of other control loops [2-4,13,46]. When each input output pair is controlled, the overall system is controlled.

In Figure 2.19, the de-centralized control scheme is shown for m sensors/actuators and m controllers.

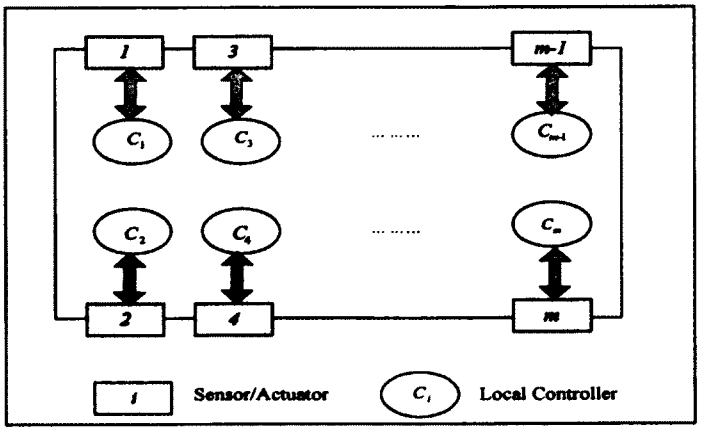

Figure 2.19. De-centralized Control Scheme

Some important notes to be mentioned with regard to the de-centralized control are as follows:

- the system modes (degrees of freedom) are not directly controlled.
- there is no authority from the de-centralized controller to control modes like roll, or pitch to a pre-set value.
- they are proven a guaranteed stability for systems with rigid body modes and also for flexible modes as well [2,7,9].

2.7.2 Centralized Control Scheme

The centralized control (integrated or modal) can control the system modes directly, or it can control the system as a whole. In order to achieve that, some necessary transformations should be performed. Usually, the measurements are transformed to modes, so the modes are de-coupled. This de-coupling step is not accurate enough, especially if the system has significant flexibility. Each mode is controlled by the corresponding modal controller to output the corresponding modal force or torque. These modal forces and torques are then transformed to control inputs (currents or voltages) via single or two transformations to be applied to the actuator. Controlling the overall system modes enables the control of the whole system.

In Figure 2.20, the centralized control scheme is shown for m sensors/actuators and m controllers.

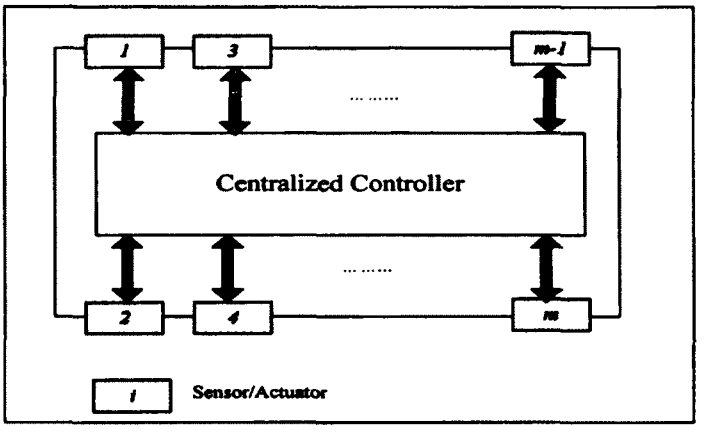

Figure 2.20. Centralized Control Scheme

Some important notes to be mentioned with regard to the centralized control are as follows:

- the system modes (degrees of freedom) are directly controlled.
- there is authority from the centralized controller to control modes like roll, or pitch to a pre-set value.
- since it is impractical to control all modes, some systems that exhibit significant flexibility may have stability issues as in [2].

The de-centralized and centralized control schemes described above are commonly used with the EMS Maglev systems. In the following chapters more illustrations on these control schemes will be introduced.

2.7.3 Flux Feedback Control

Flux feedback control for EMS Maglev systems was presented in many references like [2,13-14,18,69]. It has the merit of enhancing stability of Maglev systems. Measuring the flux in the electromagnetic suspension and feeding it back in an internal loop, as shown in Figure 2.22, increases the stability and robustness of the controlled

EMS Maglev system by reducing the effect of variations in the air gap [2]. Figure 2.21 shows a block diagram for flux feedback control of a single axis EMS Maglev system.

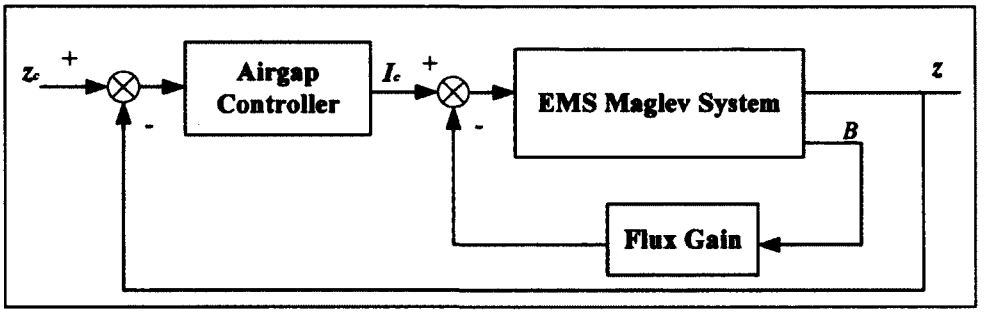

Figure 2.21. Block diagram of a Single Axis Maglev System with Flux Feedback Control

The idea behind flux feedback is to reduce the effect of the coefficients k_z, and k_i Eqs. (2.12) and (2.13). These coefficients are changing significantly as the operating point changes. The magnetic field density of the electromagnet B is:

$$B = \mu_o H = \frac{\mu_o NI}{2z}\left(1 + \frac{2z}{\pi W_m}\right) \tag{2.55}$$

where,

H: is the magnetic field intensity.

As shown in Eq. (2.55), the magnetic field density of an electromagnet is a linear function of a gap to current ratio. The magnetic flux of an electromagnet Φ is:

$$\Phi = BA = \frac{\mu_o NIA}{2z}\left(1 + \frac{2z}{\pi W_m}\right) \tag{2.56}$$

where, A: is the sectional area of the electromagnet.

It should be noted that the levitation force has a direct relationship with the magnetic flux as follows:

$$F_z = \frac{\Phi^2}{\mu_o A} \tag{2.57}$$

In Eq. (2.55), it is noted that the perturbation of the levitation force with respect to the flux operating point Φ_0 is less than the case of having perturbation with respect to the air gap and current operating points z_o, and I_o.

When linearizing the flux expression in Eq.(2.56), the following is received:

$$\Delta\Phi = k_{\Phi I} I + k_{\Phi z} z \tag{2.58}$$

where, $k_{\Phi I}$, and $k_{\Phi z}$ are the linearization coefficients

$$k_{\Phi I} = \left.\frac{\partial\Phi}{\partial I}\right|_{z_o, I_o} = \frac{\mu_o NA}{2z_o}\left(1 + \frac{2z_o}{\pi W_m}\right) \tag{2.59}$$

$$k_{\Phi z} = \left.\frac{\partial\Phi}{\partial z}\right|_{z_o, I_o} = \frac{-\mu_o NAI_O}{2z_o^2}\left(1 + \frac{2z_o}{\pi W_m}\right) + \frac{\mu_o NAI_o}{\pi W_m z_o} \tag{2.60}$$

Inclusion of flux feedback in a single axis EMS Maglev system block diagram is shown in Figure 2.22

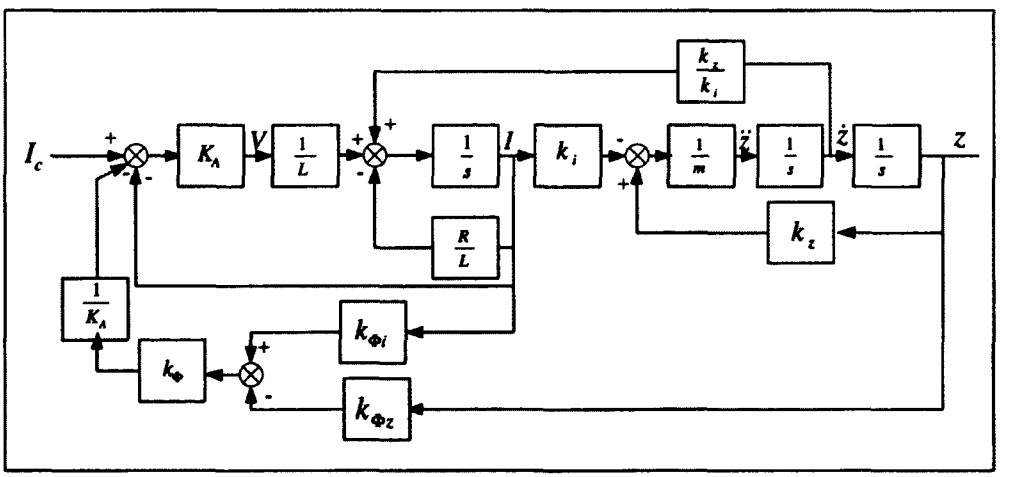

Figure 2.22. Block Diagram of an Open Loop Single Axis Maglev System with Flux Feedback

where, k_Φ is the flux feedback gain. This gain when chosen properly, the stability of a Maglev system will be enhanced.

So, the state space model of the linear single axis Maglev rigid system with flux feedback can be written as follows [2]:

$$\begin{bmatrix} \dot{z} \\ \ddot{z} \\ \dot{I} \end{bmatrix} = \begin{bmatrix} 0 & 1 & 0 \\ k_z/m & 0 & -k_i/m \\ k_\Phi k_{\Phi z}/L & k_z/k_i & -(k_\Phi k_{\Phi i} + K_A + R)/L \end{bmatrix} \begin{bmatrix} z \\ \dot{z} \\ I \end{bmatrix} + \begin{bmatrix} 0 \\ 0 \\ K_A/L \end{bmatrix} I_c \tag{2.61}$$

$$[z] = [1 \quad 0 \quad 0] \begin{bmatrix} z \\ \dot{z} \\ I \end{bmatrix} \tag{2.62}$$

where Eqs. (2.61) and (2.62) are the state equation and the output equation, respectively, with:

$$A = \begin{bmatrix} 0 & 1 & 0 \\ k_z/m & 0 & -k_i/m \\ k_\Phi k_{\Phi z}/L & k_z/k_i & -(k_\Phi k_{\Phi i} + K_A + R)/L \end{bmatrix}; B = \begin{bmatrix} 0 \\ 0 \\ K_A/L \end{bmatrix}; C = [1 \quad 0 \quad 0]; \text{ and } D = 0$$

representing the dynamics, input, output and throughput matrices, respectively.

The system transfer function is:

$$G_\Phi(s) = C(sI - A)^{-1}B + D = \frac{-K_\lambda}{mLs^3 + m(k_\Phi k_{\Phi i} + K_A + R)s^2 + k_\Phi(k_i k_{\Phi z} - k_z k_{\Phi i}) - k_z(K_A + R)} \tag{2.63}$$

where,

$$K_\lambda = K_A k_i$$

Observing Eq. (2.63), if

$$k_\Phi = \frac{k_z(K_A + R)}{k_i k_{\Phi z} - k_z k_{\Phi i}} \tag{2.64}$$

then,

$$G_{\Phi}(s) = C(sI - A)^{-1}B + D = \frac{-\frac{K_{\lambda}}{L}}{s^3 + \left(k_{\Phi}k_{\Phi i} + \frac{K_A + R}{L}\right)s^2} \tag{2.65}$$

Comparing Eq. (2.63) with Eq. (2.16), it is clearly noted that the flux feedback has the advantage of eliminating the unstable pole ω_m in Eq. (2.19). The new transfer function of the system $G_{\Phi}(s)$ has two poles ω_{Φ} at origin and one pole at the left hand plane α_{Φ} which shows a conditional stable system [13].

$$\alpha_{\Phi} = -\left(k_{\Phi}k_{\Phi i} + \frac{K_A + R}{L}\right) \tag{2.66}$$

The poles of the system $G_{\Phi}(s)$ are independent of k_z that ensures that the new system is less sensitive to the variations in the air gap operating point.

The flux feedback technique is not only helpful to improve the Maglev system stability but also in noise rejection [2] by having flux control in the inner loop and air gap control in the outer loop.

Figure 2.23 shows the pole-zero map of the single axis EMS Maglev system open loop.

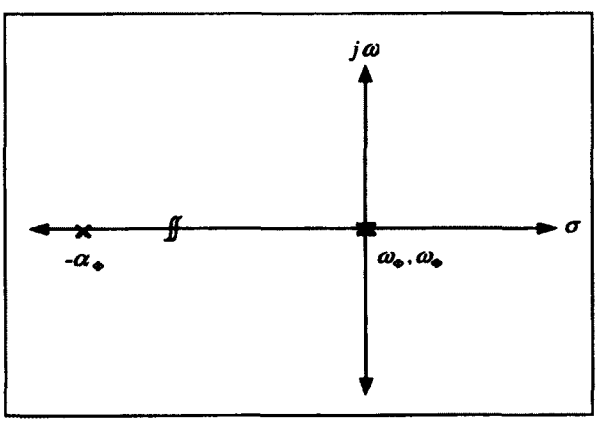

Figure 2.23. Pole-Zero map of Single Axis EMS Maglev System with Flux Feedback

It should be noted that calculation of k_Φ may be not accurate. One could overestimate or underestimate k_Φ so, the mechanical poles ω_Φ will not be at the origin. Considering three cases, the desired case $G(s)$ in which k_Φ is calculated accurately as in Eq.(2.64), $G_1(s)$ for k_Φ is 10% below, and $G_2(s)$ for k_Φ is 10% above; the pole-zero map is shown as Figure 2.24. The mechanical poles stay at origin as desired if k_Φ is properly selected. If k_Φ is 10% below, the mechanical poles will be on the $j\omega$ axis, if k_Φ is 10% above, one of the mechanical poles will be unstable similar to the original case with no flux feedback as in Eq. (2.16).

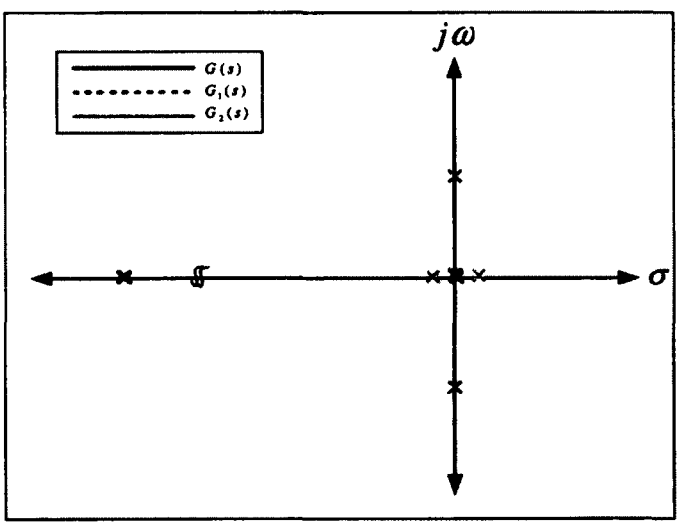

Figure 2.24. Pole-Zero map of Single Axis EMS Maglev System with Flux Feedback (Different Cases)

The step responses of these cases are achieved by designing one suitable PD controller for the system $G(s)$ and use it for all cases as shown in Figure 2.25. Two stable responses are received when k_Φ is properly selected and k_Φ is 10% above and one unstable response

for k_{Φ} is 10% below. The achieved results in Figures 2.24 and 2.25 are for a single axis EMS Maglev system using the same parameters as for the ODU EMS Maglev system except that the mass is m=1000kg.

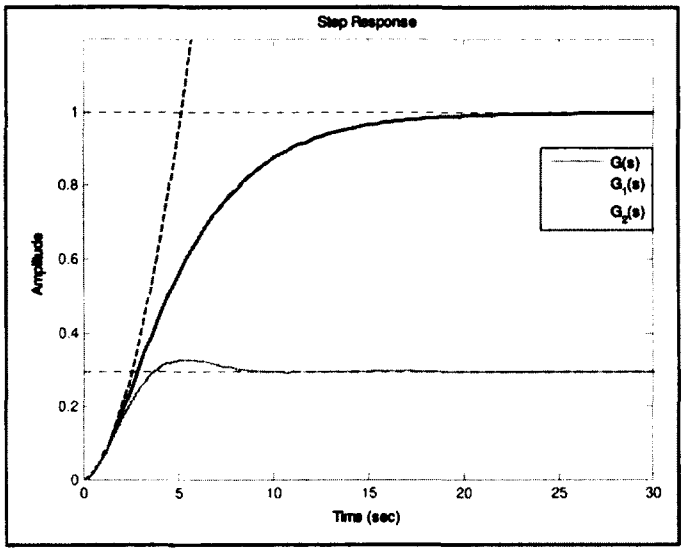

Figure 2.25. Step Response of Single Axis EMS Maglev System with Flux Feedback (Different Cases)

The question that arises is how to implement the flux feedback technique in practice. The magnetic flux of the electromagnet should be measured. Usually, the flux measurements can beattained by search coil or Hall-effect sensors. Hall-effect sensors must be mounted near the electromagnet pole face to minimize the measurement of leakage flux [18]. A search coil sensor provides transient flux measurements [13]. It is well known that the output signal, V, of a search coil sensor depends on the rate of change of flux density, dB/dt, which requires integration of the output signal. Hall-effect sensors enable flux control, both dynamically and in the steady state, but they need signal conditioning

circuits to interface with digital computer. In the ODU Maglev test bogie, Hall-effect sensors are utilized. Also it should be noted that the Hall-effect sensor measures the magnetic field density of an electromagnet B, which necessitates a conversion to magnetic flux Φ by using Eq. (2.54).

2.8 Discussions

The modeling of two simple EMS Maglev systems is introduced. Simple EMS Maglev systems are studied first before working with the ODU EMS Maglev system. Nonlinear equations of motion of a simple single DOF EMS Maglev system are derived. The linearized equations for this system are introduced. The unstable nature of a single axis EMS Maglev open loop system is discussed.

The complete nonlinear model of the 2-DOF EMS Maglev system for an inverted U-rail is introduced. The 2-DOF EMS Maglev system model is considered to be the simplest model that describes the heave and lateral motions when two magnets are used. Rigid body case and flexible case models are introduced. The static characteristics of the staggered magnet pair is presented to show the levitation and lateral forces change with the stagger distance. The 2-D and 3-D plots for the static characteristics of the levitation and lateral forces of the staggered pair are shown. At $\Delta=0$, the levitation force decreases rapidly while the lateral force increases rapidly towards its maximum, as the magnet set is displaced laterally. A considerable reduction in the levitation forces of the magnets are discovered with increasing stagger. This is due to the high coupling between the levitation force and the stagger distance Δ. The stagger distance for a magnet pair can be determined from the point of intersection at $\frac{y}{z}=2$ and $\frac{F_z}{F_z(0)}=0.75$ that corresponds to

$\Delta = 1.2z$ for the 2-DOF EMS Maglev system. This result can be generalized and applied on the ODU EMS Maglev system to decide which stagger distance to be used.

Multivariable control tools that are usually utilized for Multi input Multi Output systems analysis are presented. These tools include relative gain array (RGA), coupling factor, and the Niederlinski index. Complete description of these tools is introduced and special case of two input two output system is also provided. Auto tuning technique, characteristic locus method, optimization method, and trial and error method are introduced to provide with an insight on methods that are used to select the gains of the Multivariable PID controller.

The commonly used control schemes for EMS Maglev systems, de-centralized and centralized are introduced. Some challenges appear when utilizing the centralized control technique with the EMS Maglev system that possess infinite flexible modes. Practically, it is difficult to control all flexible modes by the centralized control technique due to the complication of their determination from local measurements. More illustrations on that issue are found in the next chapter.

Finally, the flux feedback principle is introduced. The complete linearized model of a single axis EMS Maglev system with flux feedback is presented. Flux feedback enhances the stability of these systems by selecting a suitable flux feedback gain to be used with the flux measurement in the inner loop. This gain makes the system independent of the air gap variations and hence it will more resistant to noise, but this gain should be carefully selected to avoid undesired instability that may result if it is overestimated.

CHAPTER 3

DE-CENTRALIZED AND CENTRALIZED CONTROL FOR EMS MAGLEV SYSTEM LEVITATION AND GUIDANCE

3.1 Introduction

In this chapter, the design of the de-centralized and centralized controllers for the nonlinear 2-DOF EMS Maglev system that was presented in chapter 2 is presented. In order to proceed in the design process, a linearized model for this system is introduced.

The pole-zero map for the system with the de-centralized and centralized schemes are shown for both rigid and flexible cases. A relative gain array is plotted for this scheme for both cases. Details for de-centralized controller design are presented. The MIMO root loci for this system (rigid and flexible cases) with the de-centralized controller are depicted.

An LQR based gradient-like search algorithm for MIMO PID controller tuning is introduced. This algorithm is to be applied on both de-centralized and centralized control schemes to have a unified criterion of gain selection. To have a fair comparison between these two schemes, the controllers' gains are selected on a unified base. Simulation results for the nonlinear 2-DOF EMS Maglev system rigid and flexible cases with the tuned controllers are depicted. Conclusions on the results received for the de-centralized and centralized control are introduced.

3.2 Linearized Model for 2-DOF EMS Maglev System

The system equations of motion are nonlinear and difficult to deal with, therefore the linearization principle is applied to get a linear perturbation model, which is easier [71]. The system linearized models are also providing with some useful properties that are found in the linear control theory.

A Linearized model can be obtained when a linearization technique is applied properly around the nominal equilibrium point x_o, then the system state space model is:

$$\begin{aligned} \dot{x} &= Ax + Bu \\ y &= Cx \end{aligned} \tag{3.1}$$

where:

$A = \left[\frac{\partial f}{\partial x}\right]_{\substack{x=x_o \\ u=u_o}}$ is the Jacobian matrix of f w.r.t x at (x=x_o, u=u_o)

$B = \left[\frac{\partial f}{\partial u}\right]_{\substack{x=x_o \\ u=u_o}}$, is the Jacobian matrix of f w.r.t x at (x=x_o, u=u_o)

C: is the output matrix (the system measured states are z and y).

The linearization technique is applied on the system nonlinear equations that are presented in Chapter 2 for both rigid and flexible cases (Eqs. (2.35) and (2.36)).

For the system rigid case,

$$A = \begin{pmatrix} 0 & 1 & 0 & 0 & 0 & 0 \\ a_{21} & 0 & a_{23} & 0 & a_{25} & a_{26} \\ 0 & 0 & 0 & 1 & 0 & 0 \\ a_{41} & 0 & a_{43} & 0 & a_{45} & a_{46} \\ 0 & 0 & 0 & 0 & a_{55} & 0 \\ 0 & 0 & 0 & 0 & 0 & a_{66} \end{pmatrix}, \quad B = \begin{pmatrix} 0 & 0 \\ 0 & 0 \\ 0 & 0 \\ 0 & 0 \\ \varepsilon & 0 \\ 0 & \varepsilon \end{pmatrix}, \quad C = \begin{pmatrix} 1 & 0 & 0 & 0 & 0 & 0 \\ 0 & 0 & 1 & 0 & 0 & 0 \end{pmatrix} \tag{3.2}$$

where,

$$a_{21}=-\frac{(k_{z_1}+k_{z_2})}{m},\ a_{23}=-\frac{(k_{y_1}+k_{y_2})}{m},\ a_{25}=-\frac{k_{i_1}}{m},\ a_{26}=-\frac{k_{i_2}}{m},\ a_{41}=-\frac{(k_{zy_1}-k_{zy_2})}{m},\ a_{43}=\frac{(k_{yy_2}-k_{yy_1})}{m},$$

$$a_{45}=-\frac{k_{iy_1}}{m},\ a_{46}=\frac{k_{iy_2}}{m},\ a_{55}=-\alpha+k_{it},\ a_{66}=a_{55}$$

where the linearization constants are

$$k_{z_1}=\left.\frac{\partial F_{z_1}}{\partial z}\right|_{z_o,y_o,I_o}=\frac{1}{4}\frac{\mu_o N^2 L_m W_m I_o^2}{z_o^2}\left(\frac{2}{\pi W_m}\left(\left(\frac{\tan^{-1}\left(\frac{\Delta-y}{z_o}\right)(\Delta-y)}{z_o}-1\right)\right)-z_o\left(\frac{\tan^{-1}\left(\frac{\Delta-y}{z_o}\right)(\Delta-y)}{z_o^2}+\left(\frac{(\Delta-y)^2}{z_o^3\left(\frac{(\Delta-y)^2}{z_o^2}+1\right)}\right)\right)\right) \tag{3.4}$$

$$k_{z_2}=\left.\frac{\partial F_{z_2}}{\partial z}\right|_{z_o,y_o,I_o}=\frac{1}{4}\frac{\mu_o N^2 L_m W_m I_o^2}{z_o^2}\left(\frac{2}{\pi W_m}\left(\left(\frac{\tan^{-1}\left(\frac{\Delta+y}{z_o}\right)(\Delta+y)}{z_o}-1\right)\right)-\left(\frac{\tan^{-1}\left(\frac{\Delta+y}{z_o}\right)(\Delta+y)}{z_o}+\left(\frac{(\Delta+y)^2}{(\Delta+y)^2+z_o^2}\right)\right)\right) \tag{3.5}$$

$$k_{y_1}=\left.\frac{\partial F_{y_1}}{\partial y}\right|_{z_o,y_o,I_o}=\frac{1}{4}\frac{\mu_o N^2 L_m W_m I_o^2}{z_o}\left(\frac{2}{\pi W_m}\left(\left(\frac{\tan^{-1}\left(\frac{\Delta-y}{z_o}\right)}{z_o}+\left(\frac{(\Delta-y)}{\left((\Delta-y)^2+z_o^2\right)}\right)\right)\right)\right) \tag{3.6}$$

$$k_{y_2}=\left.\frac{\partial F_{y_2}}{\partial y}\right|_{z_o,y_o,I_o}=\frac{1}{4}\frac{\mu_o N^2 L_m W_m I_o^2}{z_o}\left(\frac{2}{\pi W_m}\left(\left(\frac{\tan^{-1}\left(\frac{\Delta+y}{z_o}\right)}{z_o}+\left(\frac{(\Delta+y)}{\left((\Delta+y)^2+z_o^2\right)}\right)\right)\right)\right) \tag{3.7}$$

$$k_{i_1}=\left.\frac{\partial F_{z_1}}{\partial I_1}\right|_{z_o,y_o,I_o}=-\frac{\mu_o N^2 L_m W_m I_o^2}{2z_o^2}\left(\frac{2}{\pi W_m}\left(\tan^{-1}\left(\left(\frac{\Delta-y}{z_o}\right)(\Delta-y)\right)-z_o\right)-1\right) \tag{3.8}$$

$$k_{i_2}=\left.\frac{\partial F_z}{\partial I_2}\right|_{z_o,y_o,I_o}=-\frac{\mu_o N^2 L_m W_m I_o^2}{2z_o^2}\left(\frac{2}{\pi W_m}\left(\tan^{-1}\left(\left(\frac{\Delta+y}{z_o}\right)(\Delta+y)\right)-z_o\right)-1\right) \tag{3.9}$$

$$k_{zy_1}=\left.\frac{\partial F_{y_1}}{\partial z}\right|_{z_o,y_o,I_o}=-\frac{\mu_o N^2 L_m W_m I_o^2}{2\pi z_o^2}\left(\tan^{-1}\left(\frac{\Delta-y}{z_o}\right)-\frac{(\Delta-y)}{z_o\left(\left(\frac{\Delta-y}{z_o}\right)^2+1\right)}\right) \tag{3.10}$$

$$k_{zy_2}=\left.\frac{\partial F_{y_2}}{\partial z}\right|_{z_o,y_o,I_o}=-\frac{\mu_o N^2 L_m W_m I_o^2}{2\pi z_o^2}\left(\tan^{-1}\left(\frac{\Delta+y}{z_o}\right)-\frac{(\Delta+y)}{z_o\left(\left(\frac{\Delta+y}{z_o}\right)^2+1\right)}\right) \tag{3.11}$$

$$k_{yy_1} = \left.\frac{\partial F_{y_1}}{\partial y}\right|_{z_o, y_o, I_o} = -\frac{\mu_o N^2 L_m W_m I_o^2}{2\pi z_o^2}\left(\frac{1}{\left(\left(\frac{\Delta - y}{z_o}\right)^2 + 1\right)}\right) \tag{3.12}$$

$$k_{yy_2} = \left.\frac{\partial F_{y_1}}{\partial y}\right|_{z_o, y_o, I_o} = -\frac{\mu_o N^2 L_m W_m I_o^2}{2\pi z_o^2}\left(\frac{1}{\left(\left(\frac{\Delta + y}{z_o}\right)^2 + 1\right)}\right) \tag{3.13}$$

$$k_{iy_1} = \left.\frac{\partial F_{y_1}}{\partial I_1}\right|_{z_o, y_o, I_o} = -\frac{\mu_o N^2 L_m W_m I_o^2}{\pi z_o}\left(\tan^{-1}\left(\frac{\Delta - y}{z_o}\right)\right) \tag{3.14}$$

$$k_{iy_2} = \left.\frac{\partial F_{y_2}}{\partial I_2}\right|_{z_o, y_o, I_o} = -\frac{\mu_o N^2 L_m W_m I_o^2}{\pi z_o}\left(\tan^{-1}\left(\frac{\Delta + y}{z_o}\right)\right) \tag{3.15}$$

$$k_{iz} = -I_o \dot{z}_o z_o^2 \tag{3.16}$$

The flexible system case state space model is (with the subscript *f* for flexible):

$$A_f = \begin{pmatrix} 0 & 1 & 0 & 0 & 0 & 0 & 0 & 0 \\ \bar{a}_{21} & \bar{a}_{22} & \bar{a}_{23} & 0 & \bar{a}_{25} & \bar{a}_{26} & \bar{a}_{27} & \bar{a}_{28} \\ 0 & 0 & 0 & 1 & 0 & 0 & 0 & 0 \\ \bar{a}_{41} & 0 & \bar{a}_{43} & 0 & \bar{a}_{45} & \bar{a}_{46} & 0 & 0 \\ \bar{a}_{62} & \bar{a}_{52} & 0 & 0 & \bar{a}_{55} & 0 & 0 & 0 \\ \bar{a}_{61} & \bar{a}_{62} & 0 & 0 & 0 & \bar{a}_{66} & 0 & 0 \\ 0 & 0 & 0 & 0 & 0 & 0 & 0 & 1 \\ \bar{a}_{81} & \bar{a}_{82} & 0 & 0 & 0 & 0 & \bar{a}_{87} & \bar{a}_{88} \end{pmatrix}, B_f = \begin{pmatrix} 0 & 0 \\ 0 & 0 \\ 0 & 0 \\ 0 & 0 \\ \beta & 0 \\ 0 & \beta \\ 0 & 0 \\ 0 & 0 \end{pmatrix}, C_f = \begin{pmatrix} 1 & 0 & 0 & 0 & 0 & 0 & 0 & 0 \\ 0 & 0 & 1 & 0 & 0 & 0 & 0 & 0 \end{pmatrix} \tag{3.17}$$

where

$$\bar{a}_{21} = -\frac{(k_{z_1} + k_{z_2})}{m_2} - \frac{\kappa}{m_2}, \bar{a}_{22} = -\frac{c}{m_2}, \bar{a}_{23} = -\frac{(k_{y_1} + k_{y_2})}{m_2}, \bar{a}_{25} = -\frac{k_{i_1}}{m_2}, \bar{a}_{26} = -\frac{k_{i_2}}{m_2}, \bar{a}_{27} = \frac{\kappa}{m_2}, \bar{a}_{28} = -\bar{a}_{22} = \frac{c}{m_2},$$

$$\bar{a}_{41} = -\frac{(k_{zy_1} - k_{zy_2})}{M}, \bar{a}_{43} = \frac{k_{yy_2} - k_{yy_1}}{M}, \bar{a}_{45} = -\frac{k_{iy_1}}{M}, \bar{a}_{46} = \frac{k_{iy_2}}{M}, \bar{a}_{51} = k_{iz}, \bar{a}_{61} = \bar{a}_{51}, \bar{a}_{52} = k_{i_1},$$

$$\bar{a}_{55} = -\alpha + k_{iz}, \bar{a}_{62} = k_{i_2}, \bar{a}_{66} = \bar{a}_{55}, \bar{a}_{81} = \frac{\kappa}{m_1}, \bar{a}_{82} = \frac{c}{m_1}, \bar{a}_{87} = -\bar{a}_{81}, \bar{a}_{88} = -\bar{a}_{82}$$

where κ and c are the spring stiffness and viscous damping coefficients, respectively.

$$k_{i_1} = \left.\frac{\partial f_5}{\partial \dot{z}}\right|_{x=x_o} = \frac{I_o}{z_o} \quad , k_{i_2} = \left.\frac{\partial f_6}{\partial \dot{z}}\right|_{x=x_o} = k_{i_1} \quad , k_{iz} = \frac{\dot{z}_o}{z_o} \tag{3.18}$$

The system open loop transfer function can be easily determined from the state space model of the system linearized model as follows:

$$G(s) = C(sI - A)^{-1} B$$

$$G(s) = \begin{bmatrix} g_{11}(s) & g_{12}(s) \\ g_{21}(s) & g_{22}(s) \end{bmatrix} \tag{3.19}$$

This is a two input two output (TITO) transfer function. In Figure 3.1, the open loop system block diagram is shown.

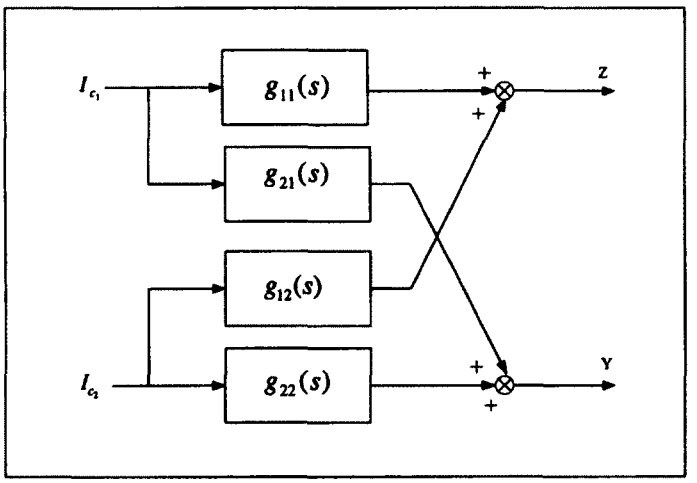

Figure 3.1. Open Loop System Block Diagram

In the following sections, important notes will be included based on the EMS Maglev system linearized model.

3.3 De-centralized Control of the 2-DOF EMS Maglev System

3.3.1 De-centralized Control Scheme

In this section a de-centralized control for the EMS Maglev system is introduced. In the de-centralized scheme, controllers are designed locally for each input-output pair as co-located actuators and sensors as shown in Figure 3.2. De-centralized control means that each magnet has its own control loop that is independent of other control loops [32]. Each controller is based on the magnet's air gap measurement, and has been designed to have sufficient damping. The controller aims to maintain the magnetic air gap to a certain value z_c. In this approach, the outputs (local measurements) are fed back into local controllers; one for each magnet. De-centralized PD or PID controllers are commonly utilized for EMS Maglev systems and they are sufficient [2-4,7,44-45]. The local measurements for this typical system are the same as the heave and lateral modes. The form of the de-centralized PD controller is:

$$\begin{aligned} I_{c_n} &= K_{p_n} e_n + K_{d_n} \dot{e}_n \\ e_n &= z_{c_n} - z_n \end{aligned} \tag{3.20}$$

where z_{c_n} : is the command air gap, K_{p_n}, and K_{d_n} are the controller proportional and derivative gains, respectively, and n =1,2 is the number of electromagnets.

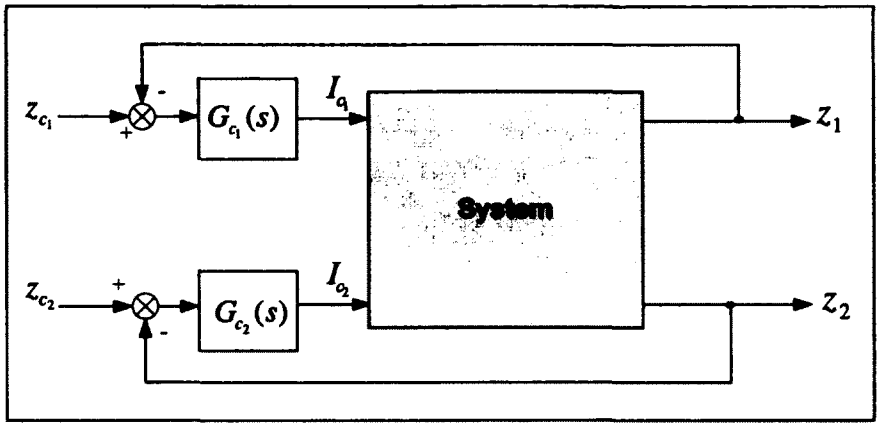

Figure 3.2. A 2-DOF EMS Maglev System with De-centralized Control

In de-centralized control, the stagger offset Δ is set to zero. This is due to the fact that staggering for de-centralized case is not useful as the levitation force reduces significantly, and no considerable change for the lateral force achieved. In de-centralized control, the lateral control is attained passively since when the absolute value of lateral displacement is greater than zero, the U-shaped magnets will align themselves with the inverted U-rail guideways to damp the lateral motion out naturally. This fact will be clarified in the next sections.

3.3.2 Pole zero Map for Rigid and Flexible Cases

In this section, a simple generic pole zero map is drawn for the 2-DOF EMS Maglev system open loop poles for the de-centralized scheme. This can be easily achieved by the aid of MATLAB.

In Figure 3.3, a generic pole-zero map for the system rigid case is shown. There are six poles, where two poles $\alpha_i, i = 1,2$ are far in the left hand side for the electrodynamics. Two poles p_{l_1}, p_{l_2} are located near the $j\omega$ axis for the lateral channel in the left hand

plane. Two poles $-\omega_m$, ω_m one in the left and one in the right hand plane for the heave channel. There are no transmission zeros.

In Figure 3.3, the flexible system case is shown by having two more poles p_{f_1}, p_{f_2} for the flexible mode and two transmission zeros z_{f_1}, z_{f_2}; both are located on the $j\omega$ axis inside dotted circles as shown in Figure 3.3.

The lateral poles for both rigid and flexible cases indicate stable behavior for the lateral motion unlike the heave motion which is unstable. This result coincides with another result found in [10-12] about lateral motion stability. The location of the alternating poles and zeros in Figure 3.3 is for a very lightly damped system with co-located actuators and sensors. If structural damping is considered for the flexible case, the alternating poles and zeros would be shifted into the left hand plane [72].

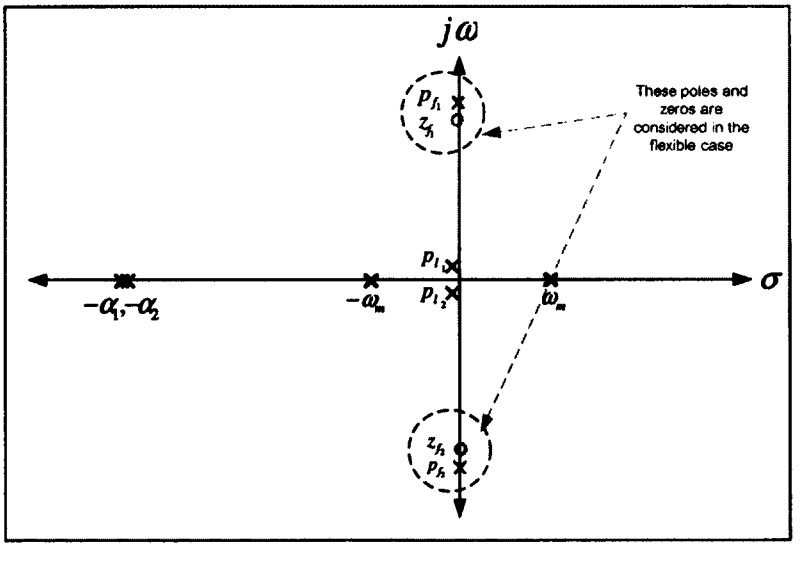

Figure 3.3. EMS Maglev System Open Loop Generic Pole-Zero Map (De-centralized Scheme)

3.3.3 Relative Gain Array for De-centralized Scheme Rigid and Flexible Cases

The Relative Gain Array is a technique invented by Bristol [49] that can be used for Multi Input Multi Output systems to define the degree of interaction between direct and cross channels. This technique is useful to show how much effort the controller should provide to overcome this interaction. In this section the RGA for system rigid and flexible cases is shown when the de-centralized controller is utilized.

Based on the ODU Maglev system electromagnet's parameters, zero stagger will result in interactions between loops for the rigid case is as follows:

$$RGA^{d}_{rigid} = \begin{bmatrix} 0.5 & 0.5 \\ 0.5 & 0.5 \end{bmatrix} \tag{3.21}$$

which means that equal interactions between direct and cross channels are the same. For a TITO system, if λ_{ij}=0.5, this indicates that there is a severe interaction between the two loops. A positive coupling factor $\kappa_o = 1$ for that system is observed; that means the selected pairs u_1 to y_1 and u_2 to y_2 are appropriate.

For similar conditions that are used for the rigid case, having the secondary mass of one tenth the primary mass, and the stiffness coefficient in Figure 2.12 is

$$\kappa = m_1 \omega_1^2 \tag{3.22}$$

where, ω_1 is the vibration frequency of the first mode of the ODU test bogie.

The interactions between loops are as follows:

$$RGA^{d}_{flex} = \begin{bmatrix} 0.666 & 0.333 \\ 0.333 & 0.666 \end{bmatrix} \tag{3.23}$$

Lower interactions are observed in the cross channels than in the direct channels. The received values of the individual RGA matrix elements are not exactly equal to 0.5, which means that the control for the direct and cross interactions of the flexible case is easier than the rigid case.

A positive coupling factor $\kappa_o = 0.25$ for that system is observed, which means the selected pairs u_1 to y_1 and u_2 to y_2 are appropriate, and the control of the flexible case is easier.

Increasing secondary mass to be 40% of primary mass makes the flexibility more pronounced. The RGA in the direct and cross channels are the same as in Eq. (3.23). This means that the de-centralized control does not experience considerable major changes when controlling EMS Maglev systems with significant flexibility, or it can be noted that the de-centralized control can stabilize EMS Maglev systems with significant flexibility without having big changes in the controllers' gains.

3.3.4 The De-centralized PD Controller Design

In this section, the de-centralized PD control with the 2-DOF EMS Maglev system-rigid case is to be developed. The design procedure for the uncoupled systems as in section 2.6.3.1 can be applied for the design of the de-centralized controller. Further tuning is necessary for the controllers' gains when all loops are closed with the system to overcome the effect of the cross channel interactions. Since, the de-centralized control is concerned with the air gap control of each individual electromagnet by having an individual controller for each one, then each electromagnet loop can be considered for design as a single axis Maglev system (SISO). The stability analysis of a single axis Maglev system that was introduced in [2][7] and can be used to ensure stability of the

individual loops (SISO). Based on the linearized model of the single axis Maglev system that is presented in Chapter 2, section 2.2.3, the transfer function of the system is approximated as:

$$G(s) \cong \frac{-K_x}{(s-\omega_{mi})(s+\omega_{mi})(s+\alpha_i)} = \frac{-K_x}{(s^2-\omega_{m_i}^2)(s+\alpha_i)} \tag{3.24}$$

If PD controller $G_{c_i}(s)$ is designed for each air gap of this typical system

$$G_{c_i}(s) = K_{p_i} + K_{d_i} s \tag{3.25}$$

Then the closed loop characteristic equation is:

$$1 + G(s)G_{c_i}(s) = 0 \tag{3.26}$$

$$s^3 + \alpha_i s^2 - K_x K_{d_i} s - \left(\omega_{m_i}^2 \alpha_i + K_x K_{p_i}\right) = 0 \tag{3.27}$$

Using Routh's criterion then:

$K_{p_i} < -\frac{\alpha_i \omega_{m_i}^2}{K_x}$ and $K_{d_i} < \frac{K_{p_i}}{\alpha_i} + \frac{\omega_{m_i}^2}{K_x}$ are used to stabilize the system, which means that positive feedback should be utilized to attain a stable system [2]. The root locus of each channel with the PD controller can be monitored as in Figure 3.4.

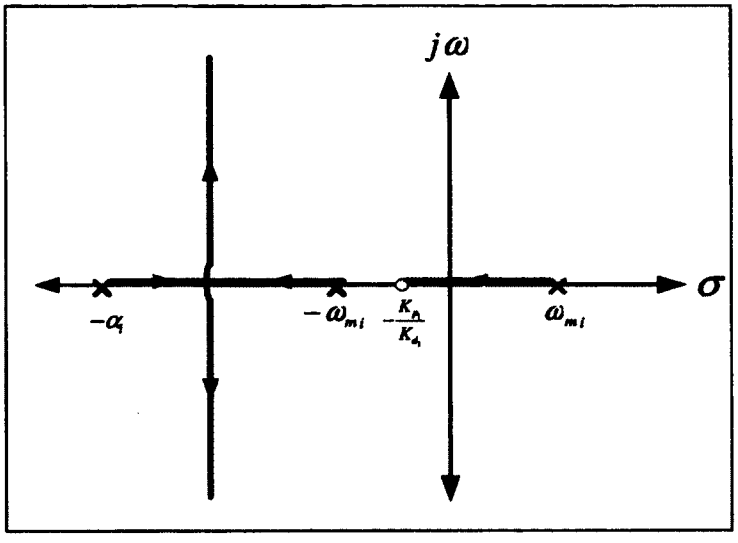

Figure 3.4. SISO Root Locus of De-centralized Control- Individual Channel

3.3.5 MIMO Root Loci for Rigid and Flexible Cases

In this section, the root loci of the system with the PD de-centralized control are shown in Figure 3.5. The closed loop poles are marked by small squares that appear in the left hand plane. For the system rigid case, the following is deduced: the PD de-centralized control does not affect three poles of the system, especially the two lateral poles and one pole of the electrodynamics, while affecting the other poles by making them more stable. The stable heave pole approaches a breakaway point with one of the electrodynamic poles and both are departing to infinity opposite to each other to an asymptote parallel to the $j\omega$ axis. The unstable one moves to the left hand plane on the real axis to a stable location.

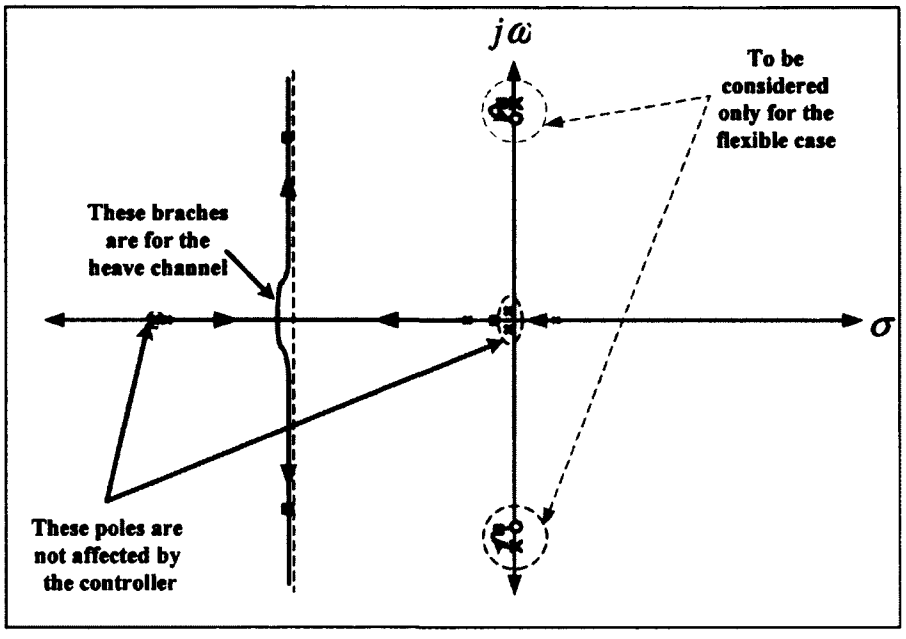

Figure 3.5. Root Loci of the PD De-centralized Control with System-Rigid and Flexible Cases

Considering the flexible case, the root loci sketch as shown in Figure 3.5 is similar to that rigid case, but in addition there are two flexible poles approach to the transmission zeros that are also located on the $j\omega$ axis.

The root loci for both rigid and flexible cases show that PD de-centralized control stabilizes the system by affecting the unstable heave pole while not affecting the lateral poles that are fortunately stable by nature [73] as shown in Figure 3.5.

The developed de-centralized controller for the rigid system case should stabilize the flexible case also. Some additional tuning may be utilized to damp the vibration of the flexible modes. The argument behind that is deduced from the previous results attained for EMS Maglev systems that ensure the ability of controlling flexible modes with the de-centralized PD controllers [3,4]. Also, the MIMO root loci for the PD de-centralized

control with the EMS Maglev system show that the flexible poles approach to the transmission zeros as $k \to \infty$.

3.4 Centralized Control of the 2-DOF EMS Maglev System

3.4.1 Centralized Control Scheme

Centralized or modal control enables the system to be controlled as a whole by measuring the local variables (air gaps and lateral displacements), converting them into modes using a transformation matrix [11,16], then controlling the suspension's modes to provide the modal forces. These modal forces are transformed to local forces. The command currents are generated from the local forces and the measured air gaps via a third transformation. When the suspension is approximated as interacting with the rail at a single point, the air gap and lateral displacement are the heave and lateral motions without transformation.

The transformation that relates the modal forces and local forces can be found from the geometry of the configuration in Figure 2.11 in Chapter 2. Then the modal forces (F_h and F_l) in terms of the magnet forces f_1 and f_2 are

$$\begin{bmatrix} F_h \\ F_l \end{bmatrix} = [T_2] \begin{bmatrix} f_1 \\ f_2 \end{bmatrix} \tag{3.28}$$

and the transformation matrix T_2 is

$$[T_2] = \begin{bmatrix} 1 & 1 \\ 1 & -1 \end{bmatrix}$$

The transformation from the magnet forces to the currents is found by linearizing the expression of the levitation force given in Eq. (2.22) in Chapter 2:

$$f_n^c \cong k_{z_n} z_n + k_{y_n} y_n + k_{i_n} I_{cn} \tag{3.29}$$

where, the linearization coefficients k_{z_n}, k_{y_n} and k_{i_n} are

$$k_{z_n} = \left.\frac{\partial F_{z_n}}{\partial z_n}\right|_{z_o, y_o, I_o}, \; k_{y_n} = \left.\frac{\partial F_{z_n}}{\partial y_n}\right|_{z_o, y_o, I_o} \text{ and } \; k_{i_n} = \left.\frac{\partial F_{z_n}}{\partial I_n}\right|_{z_o, y_o, I_o} \tag{3.30}$$

where z_o, y_o and I_o are the nominal air gap, lateral displacement, and current of each magnet, respectively.

The corresponding command current can be found from Eq.(3.7) with respect to z_n, y_j and I_{c_n} as:

$$I_{c_n} \cong \frac{f_n^c + k_{z_n} z_n + k_{y_n} y_n}{k_{i_n}} \tag{3.31}$$

In matrix form, as

$$I_c = T_3(f^c, z_n, y_n) \tag{3.32}$$

where $T_3 = diag\left[\begin{matrix} I_{c_1} & I_{c_2} & \cdots & I_{c_n} \end{matrix}\right]$.

The command model forces and torques are then

$$\begin{aligned} T^c &= K_{p_{n\Theta}} e_\Theta + K_{d_{n\Theta}} \dot{e}_\Theta \\ e_\Theta &= \Theta_c - \Theta \end{aligned} \tag{3.33}$$

where, Θ_c is the mode's command, and the controller's proportional, and derivative gains are $K_{p_{n\Theta}}$, and $K_{d_{n\Theta}}$, respectively. The centralized controller with the system is shown in Figure 3.6.

The transformation [T_3] (as shown in Figure 3.6) is considered as an inner feedback loop that changes the open loop system transfer function characteristics. Adding this transformation into the system, a new transfer function matrix is received as shown in Figure 3.6.

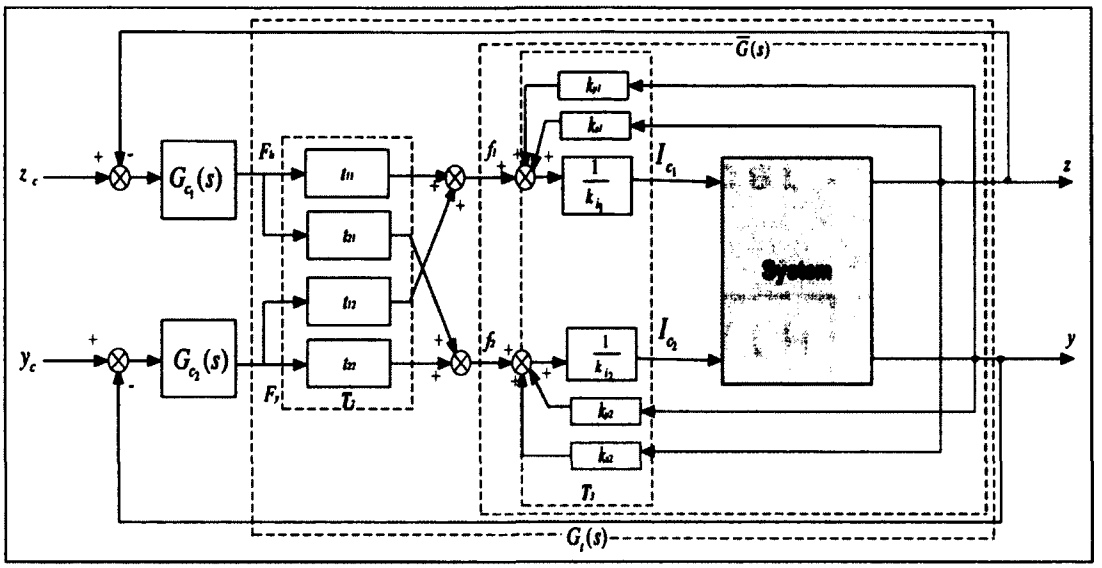

Figure 3.6. A 2-DOF EMS Maglev System with Centralized Control

$$\overline{G}(s) = k_i(s)G(s)(I - H(s)k_i(s)G(s))^{-1} \tag{3.34}$$

where,

$H(s) = \begin{bmatrix} k_{z_1} & k_{y_1} \\ k_{z_2} & k_{y_2} \end{bmatrix}$ is the displacements linearization coefficients matrix, and

$k_i(s) = \begin{bmatrix} 1/k_{i_1} & 0 \\ 0 & 1/k_{i_2} \end{bmatrix}$ is the currents linearization coefficients matrix.

$$G_t(s) = T_2 k_i(s)\overline{G}(s) \tag{3.35}$$

$G_t(s)$ relates the modal forces (F_h, and F_l) with the modes z and y.

The controllers $G_{c_1}(s)$, and $G_{c_2}(s)$ are the PD controllers of the heave and lateral channels, respectively.

3.4.2 Pole Zero Map for Rigid and Flexible Cases

In this section, a simple generic pole zero map is drawn for the 2-DOF EMS Maglev system open loop poles for the centralized scheme.

The transformation matrices $[T_2]$, and $[T_3]$ shown in Figure 3.7 for the centralized scheme changes the location of the lateral poles location slightly such that they lie on the $j\omega$ axis, thus they are marginally stable.

In Figure 3.7, a generic pole-zero map for the system rigid case is shown. There are six poles, two of which $(-\alpha_i^c, i=1,2)$ are far in the left hand side for the electrodynamics. Two poles p_{l_1}, p_{l_2} are located near the $j\omega$ axis for the lateral channel in the left hand plane. The two poles $-\omega_h$, ω_h have one in the left and one in the right hand plane for the heave channel. The electrodynamics poles are closer to each other due to the effect of the transformation T_2 on the system and there are no transmission zeros.

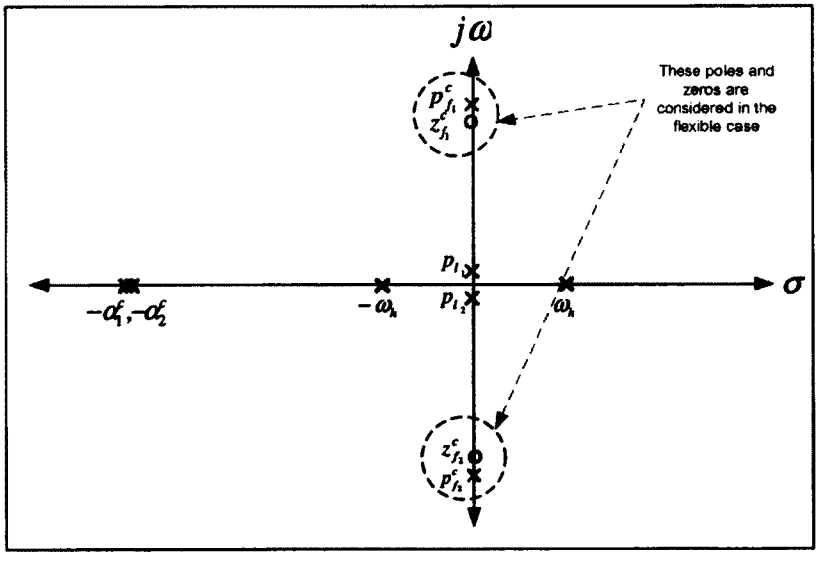

Figure 3.7. EMS Maglev System Open Loop Generic Pole-Zero Map (Centralized Scheme)

The generic pole-zero map for the flexible system case is shown in Figure 3.7 except that there are two more poles $p_{f_1}^c, p_{f_2}^c$ for the flexible mode and two transmission zeros $z_{f_1}^c, z_{f_2}^c$ both are located on the $j\omega$ axis.

3.4.3 Relative Gain Array of the Rigid and Flexible Cases

In this section, the RGA for the system rigid and flexible cases is shown when centralized control is utilized. Interesting results are expected to appear as the centralized control decouples the cross channels.

Figures 3.8, and 3.9 show the RGA Bode plot in the direct and cross channels for the rigid case, for different stagger distances. It is clearly noted that the RGA elements values are changed remarkably as the linearization coefficients are fedback to the system transfer function *G(s)* as described before and affecting the system dynamics and reduces the interaction between loops. The transformation T_3 decouples the system.

For stagger values of $\Delta=2z_o$ to $2z_o$, lower interactions between loops are found. Note z_o corresponds to the de-levitation position ($z_o = 0.75"$). Based on the ODU Maglev system parameters, a stagger of $2z_o$ will provide with the interactions between loops for the rigid case is as follows:

$$RGA_{rigid}^c = \begin{bmatrix} 1 & 0 \\ 0 & 1 \end{bmatrix} \tag{3.36}$$

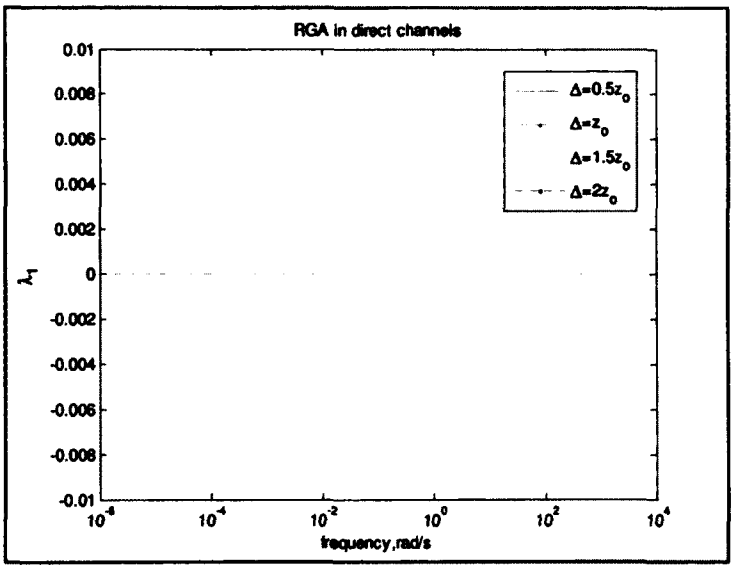

Figure 3.8. RGA in Direct Channels Bode Plot of the Centralized Scheme-Rigid Case

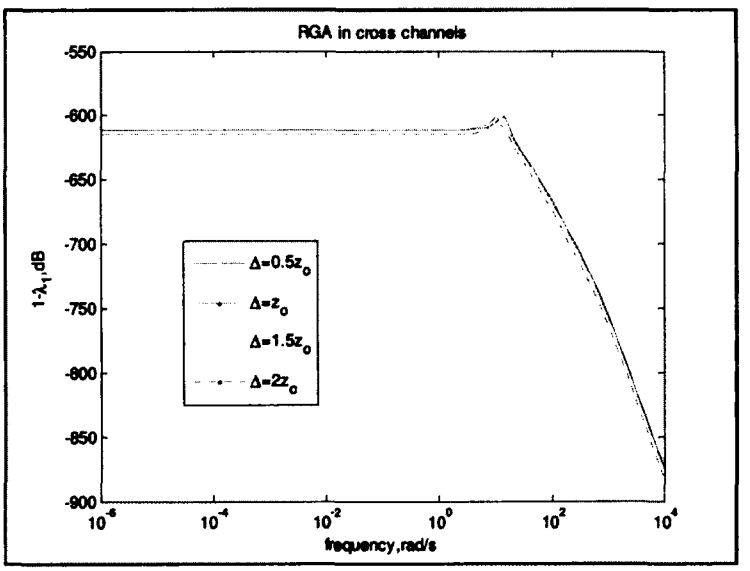

Figure 3.9. RGA in Cross Channels Bode Plot of the Centralized Scheme-Rigid Case

The interactions in the cross channels are zero. This means that the centralized control decouples the rigid body modes properly. The coupling factor $\kappa_o = 0$ for that system is observed, which means the selected pairs u_1 to y_1 and u_2 to y_2 are appropriate. It should

be noted that the control on this system will be easier as the coupling between loops is zero.

For similar conditions that are used for the rigid case, having the secondary mass of one tenth the primary mass, the interactions between loops are as follows:

$$RGA^{c}_{flexible} = \begin{bmatrix} 0.9716 & 0.0316 \\ 0.0316 & 0.9716 \end{bmatrix} \tag{3.37}$$

Small interactions appeared in the cross channels for the flexible case, while zero cross interactions are received for the rigid case. The interpretation is that the centralized control could not decouple the flexible modes efficiently and the effect of flexibility appears as small interactions in the cross channels. These interactions may require tuning of the controller gains to overcome them. The interactions in the direct channels for the flexible case is lower than for the rigid case, which indicates slightly easier control for direct channels for the flexible case.

A coupling factor $\kappa_o \cong 0$ for that system is observed, which means the selected pairs u_1 to y_1 and u_2 to y_2 are appropriate and the control of the flexible case is still possible by that control scheme. Figures 3.10, and 3.11 show the RGA Bode plot in the direct and cross channels for the flexible case for different staggers.

It is shown that the RGA Bode plots in the direct and cross channels start to change when the frequency increases from 10 to 100r/s. This may be due to the excitation of the system vibration frequency of mode 1 which in the same order (76.6r/s).

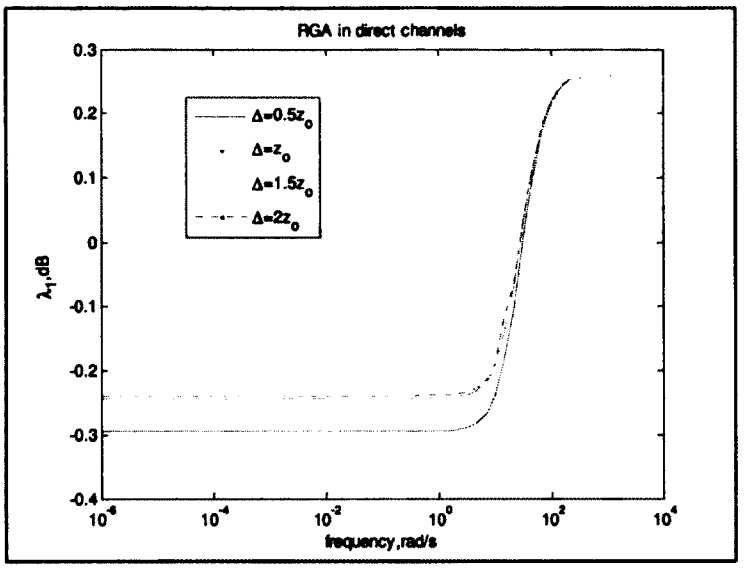

Figure 3.10. RGA in Direct Channels Bode Plot of the Centralized Scheme -Flexible

(Case 1)

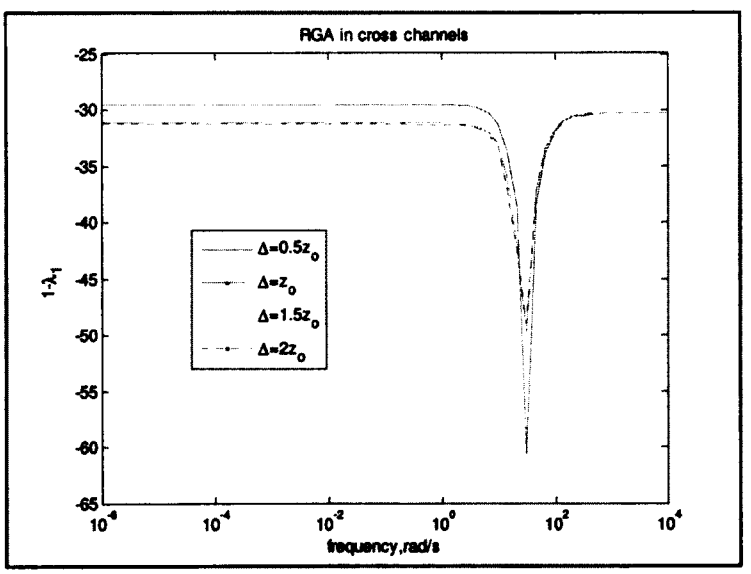

Figure 3.11. RGA in Cross Channels Bode Plot of the Centralized Scheme-Flexible

(Case 1)

With increasing flexibility in the system by having the secondary mass 40% of the primary mass, the RGA Bode plots in the direct and cross channels are as shown in Figures 3.12, and 3.13.

The flexibility effect on the RGA adds more uncertainty to the interaction between loops by having bigger notches that appear in the plots as increasing the frequency if compared with those in Figures 3.10 and 3.11. This even may require to consider the controller gains tuning.

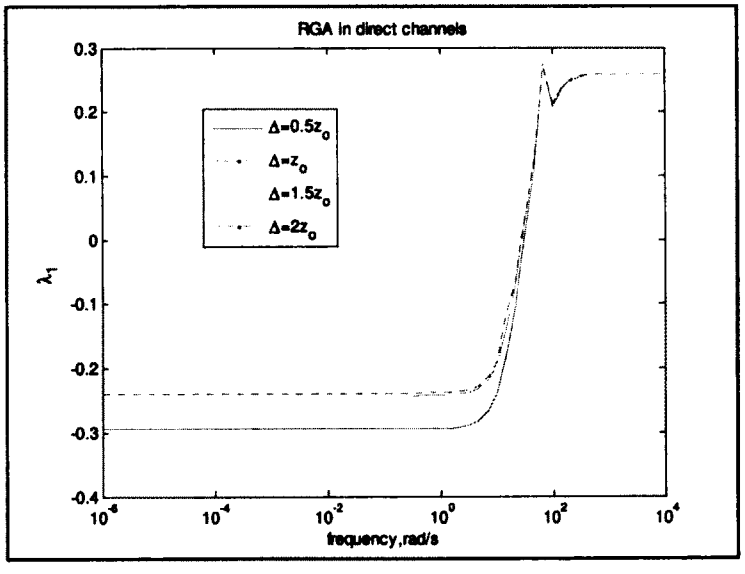

Figure 3.12. RGA in Direct Channels Bode Plot of the Centralized Scheme-Flexible (Case 2)

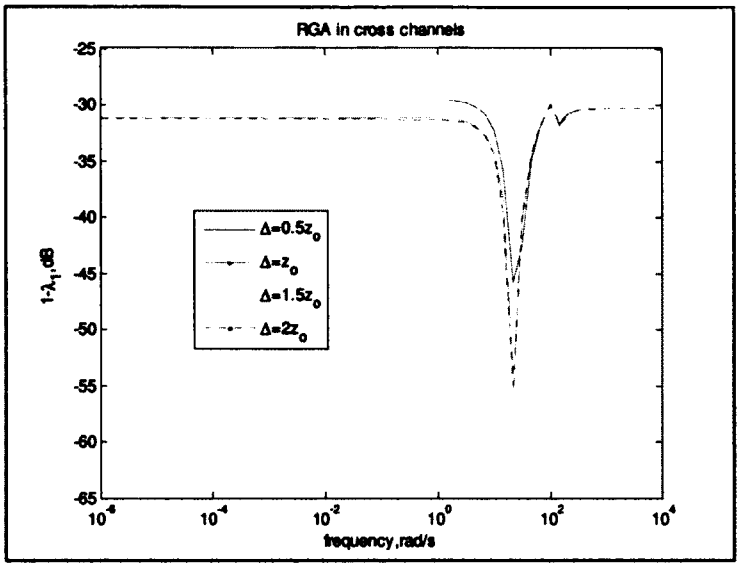

Figure 3.13. RGA in Cross Channels Bode Plot of the Centralized Scheme-Flexible (Case 2)

3.4.4 Stability Analysis for the Centralized PD Control with the 2-DOF EMS Maglev Rigid System Case

In this section, the stability analysis of the centralized PD control with the 2-DOF EMS Maglev rigid system case. The design procedure for the uncoupled systems that is presented in section 2.6.3.1 can be applied for the centralized controller design. The centralized control uses some transformation matrices that decouple the modes of a Maglev system. Then, the linearized 2-DOF Maglev system with the centralized controller transformation matrices included is as shown in Figure 3.14.

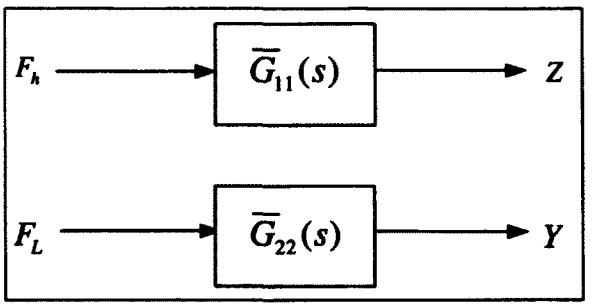

Figure 3.14. 2-DOF EMS Maglev System with the Centralized Control Transformations

where, the transfer function that relates heave force F_h and heave motion Z is

$$\overline{G}_{11}(s) \cong \frac{-K_{11}}{(s-\omega_h)(s+\omega_h)(s+\alpha_1)} \tag{3.38}$$

and the transfer function that relates lateral force F_L and lateral motion Y is

$$\overline{G}_{22}(s) \cong \frac{K_{22}}{(s+p_{l_1})(s+p_{l_2})(s+\alpha_2)} \tag{3.39}$$

where, $K_{11} = \frac{\alpha_1}{2}(a_{25}+a_{26})$, $K_{22} = -\frac{\alpha_2}{2}(a_{45}-a_{46})$, and $\alpha_1 = \alpha_2 \cong \frac{K_a}{L}$

Observing $\overline{G}_{22}(s)$, it is noted the characteristic polynomial $(s+p_{l_1})(s+p_{l_2})(s+\alpha_2)$ is marginally stable.

If PD controllers $G_{c_i}(s), i = 1,2$ are designed for both channels of this typical system,

$$G_{c_i}(s) = K_{p_i} + K_{d_i}s \tag{3.40}$$

Then the closed loop characteristic equation for the heave channel is:

$$1 + \overline{G}_{11}(s)G_{c_1}(s) = 0 \tag{3.41}$$

$$s^3 + \alpha_1 s^2 - K_{11}K_{d_1}s - (\omega_h^2\alpha_1 + K_{11}K_{p_1}) = 0 \tag{3.42}$$

Using Routh's criterion then:

$K_{p_1} < -\frac{\omega_h^2}{K_{11}}$, and $K_{d_1} < \frac{K_{p_1}}{\alpha_1} + \frac{\omega_h^2}{K_{11}}$ which indicates stability is achieved by positive feedback control [2]. The root locus of the heave channel with the PD controller $G_{c_1}(s)$ to be as shown in Figure 3.15.

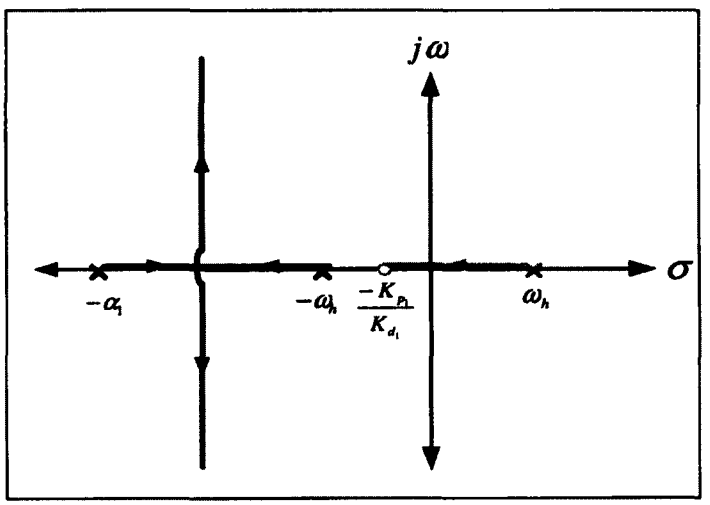

Figure 3.15. SISO Root Locus of the Heave Channel when Employing Centralized Control

The closed loop characteristic equation for the lateral channel with the controller involved is:

$$1 + \overline{G}_{22}(s)G_{c_2}(s) = 0 \tag{3.43}$$

$$s^3 + (p_{l_1} + p_{l_2} + \alpha_2)s^2 + (p_{l_1}p_{l_2} + \alpha_2(p_{l_1} + p_{l_2}) + K_{22}K_{d_2})s + (p_{l_1}p_{l_2}\alpha_2 + K_{22}K_{p_2}) = 0 \tag{3.44}$$

Using Routh's criterion:

$K_{p_2} > \frac{-\alpha_2 p_{l_1} p_{l_2}}{K_{22}} > 0$, $K_{d_2} > \frac{K_{p_2}}{\alpha_2}$, which ensures stability by negative feedback control.

The important note to be drawn here is that the lateral channel is stabilized by a negative feedback controller unlike the heave channel which needs a positive feedback controller to be stabilized. The centralized control stabilizes the EMS Maglev system once the heave motion is stabilized.

The root locus of the lateral channel with the PD controller $G_{c_2}(s)$ to be as shown in Figure 3.16.

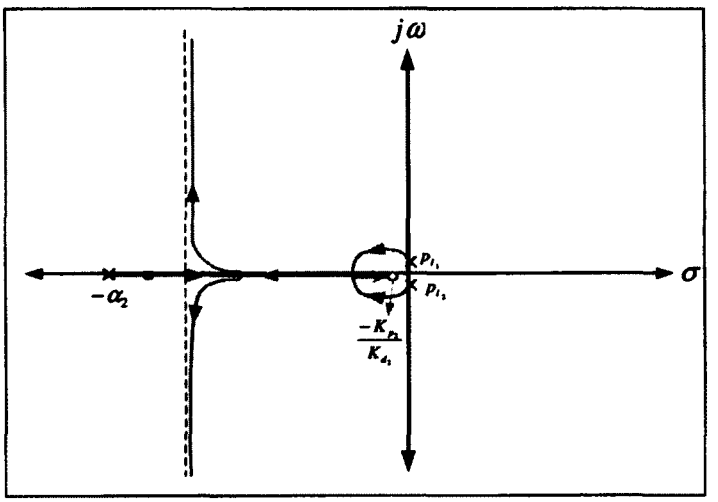

Figure 3.16. SISO Root Locus of the Lateral Channel when Employing Centralized Control

3.4.1 MIMO Root Loci for Rigid and Flexible Cases

In a similar manner, the MIMO root loci with the system when PD centralized control are shown in Figure 3.17. For the rigid system case, the two lateral poles that are on the $j\omega$ axis approach a breakaway point after moving on a circular path and then departing in the opposite direction, one of them approaches a second breaking point with one of the electrodynamics poles and departs vertically to an asymptote parallel to the $j\omega$

axis. The stable heave pole is approaching a third breakaway point with the other electrodynamics pole and departs vertically to another asymptote parallel to the $j\omega$. The unstable heave pole is travelling to the left hand plane to a stable location. Considering the flexible system case is similar to the rigid case, except that in addition, there are two flexible poles approaching the transmission zeros that are also located on the $j\omega$ axis inside dotted circles as in Figure 3.17.

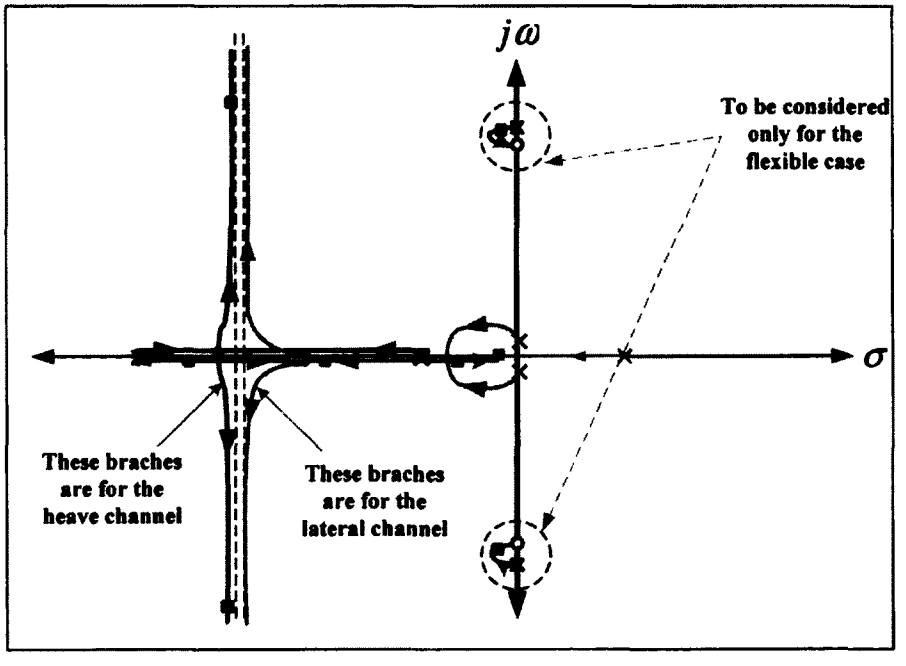

Figure 3.17. Root Loci of the PD Centralized Control with the System-Rigid and Flexible Cases

The root loci plots obtained for both rigid and flexible cases show that the PD centralized control makes the Maglev system more stable by affecting the unstable heave pole and the two marginally stable lateral poles, making them more stable [73] as shown in Figure 3.17.

It should be noted that the developed centralized controller for the rigid case can be applied on the flexible case too with some additional tuning for the PD controllers' gains. This note is deduced from the RGA Bode plots that shown small interactions in the cross channels, and from the MIMO root loci for the PD centralized control with the EMS Maglev system, that shown that the flexible poles approach to the transmission zeros as $k \to \infty$.

3.5 MIMO PID Controller Tuning Algorithm

3.5.1 An LQR Based Gradient Like Search Algorithm

In this section, a gradient-like algorithm that was found in [74] is utilized for the PID controller gain tuning. The search algorithm utilized is based on an optimal criterion for the synthesis of decentralized MIMO PID controllers that can be used for the Maglev systems. The idea behind this algorithm is that the system which is under control should be linearized (if it is nonlinear) to get a state space linearized model at the operating conditions. A linearized model can be obtained when linearization technique is applied properly around the nominal equilibrium point x_o. To consider output feedback, the gain matrix G_c is the multiplication of the output matrix by the controller K. In order to tune a decentralized MIMO PID controller, it is necessary to assure that the gain matrix G_c has a sparse structure [74]. Then the synthesized MIMO PID controller is equivalent to a static state feedback control law and thus, numerical optimization procedures can be used. The de-centralized PID controller structure definition as in [41], and can be applied to the centralized control scheme after adding the transformation matrices to the system.

To initiate the algorithm, a suitable gain matrix G_{co} (in a sparse form) is chosen by trial and error that ensures the stability of the system closed loop. Select an appropriate

weighting matrices σ, Λ and a small real number ξ that are used for updating G_c. When a sufficient number of iterations is used, then the optimized gain matrix G_c will converge. It should be noted that $J(G_c)$ for de-centralized and centralized schemes have the same value after n iterations.

The standard initial state averaged LQR objective function is:

$$J(G_c) = trace\{F(G_c)\} \tag{3.45}$$

where,

$$F(G_c) = \int_0^\infty \Gamma(t)^T (\sigma + G_c{}^T \Lambda G_c)\Gamma(t)dt \tag{3.46}$$

$\Gamma(t) = e^{(A_t + B_t G_c)t}$, $\sigma \geq 0$ and $\Lambda > 0$. $\overline{A}$ and $\overline{B}$ are the system modified dynamics and input matrices:

$$\overline{A} = \begin{bmatrix} A & 0 \\ C & 0 \end{bmatrix}, \ \overline{B} = \begin{bmatrix} B \\ 0 \end{bmatrix} \tag{3.47}$$

The matrix $A_t = \overline{A} + \overline{B}G_c$ is stable, the matrix $F(G_c)$ to be calculated by solving the following Lyapunov equation:

$$A_t^T F(G_c) + F(G_c)A_t + (\sigma + G_c{}^T \Lambda G_c) = 0 \tag{3.48}$$

The matrix W is calculated from the solution of another Lyapunov equation:

$$A_t^T W + WA_t + I = 0 \tag{3.49}$$

then, the gain matrix G_c is updated via

$$G_{c_t} = G_{c_{t-1}} - \xi \frac{d}{dG_c} trace\left\{F(G_{c_{t-1}})\right\} \tag{3.50}$$

$$\frac{d}{dG_c} trace\left\{F(G_{c_{t-1}})\right\} = 2\left(\Lambda G_c + B_t^T F(G_c)\right)W \tag{3.51}$$

A further check on the eigenvalues is performed to guarantee the stability of the closed loop system. When enough iterations are used, then the optimized gain matrix G_c will converge.

3.5.2 An LQR Based Gradient Like Search Algorithm for Controllers' Gains Tuning

The algorithm presented in the previous section was used to tune MIMO PID controllers, but here the algorithm is modified for MIMO PD controller tuning. The modification of the algorithm is to eliminate the states that represent the integral action in the PID controller. In Eq. (3.47), the modified dynamics and input matrices $\overline{A}$ and $\overline{B}$ are the same as the linearized system original dynamics and input matrices A, and B.

The nonlinearities in the Maglev system equations are found in the expressions given for the levitation and lateral forces as in Eqs. (2.22 and 2.23), and the magnet electrodynamics are as in Eq.(2.34) in Chapter 2. A linearized model can be obtained when linearization technique is applied properly around the nominal equilibrium point x_o, as in section 3.2.

The dimension of the gain matrix G_c is $2\times n_s + n_q$ for both schemes, where n_s is the number of non flexible states (rigid states, and states of the electromagnet currents), and n_q is the number of the flexible states. There are four nonzero elements in the gain matrix G_c for every scheme that represent the PD controller gains, and other elements are zero. The generalized gain matrix $G_{c_{dec}}$ for the de-centralized scheme is:

$$G_{c_{dec}} = \begin{bmatrix} k_{pz_1} & k_{dz_1} & 0_{2\times n_s+n_q-2} \\ k_{pz_2} & k_{dz_2} & \end{bmatrix} \tag{3.52}$$

The generalized gain matrix $G_{c_{cen}}$ for the centralized scheme is:

$$G_{c_{con}} = \begin{bmatrix} k_{pz} & k_{dz} & 0 & 0 & 0_{2\times n_s+n_q-4} \\ 0 & 0 & k_{py} & k_{dy} & \end{bmatrix} \tag{3.53}$$

In order to get the best output from this algorithm first, the tuned values of the controller should not flip signs. Second, the performance index J should converge as n increases. Third, the received tuned values of the gains should not violate the controller design constraints (e.g. K_p is usually bigger than K_d when PD control is utilized with an EMS Maglev system [7]). This necessitates the choice of proper values for the weighting matrices σ and Λ, and ξ.

3.5.3 Simulation Results

In this section, the simulation results of the 2-DOF Maglev system (rigid case) with the de-centralized and centralized control schemes are presented. The EMS Maglev system that is utilized here is nonlinear, and the simulation is built based on MATLAB/SIMULINK. The 2-DOF EMS Maglev system has a mass of 1000kg, and the electromagnet parameters are the same as those used for the ODU Maglev system: L=0.381m, W_m=0.051m, N=596turns, and the air gap of the de-levitated position is z=0.4". The lateral motion has been modeled according to the nonlinear equations too, but during the transition period from de-levitation to levitation or vice versa, there is an opposing lateral force simply modeled as a spring damper system that prohibits lateral displacements to appear during de-levitation.

The source of disturbing lateral force is the wind gust. The utilized wind gust model has a standard "1-cosine" shape. The model block is found in SIMULINK, and this block implements the mathematical representation in the Military Specification MIL-F-8785C. The wind gust is applied to the y-axis only, at speed of 20m/s, with a very small gust length. This represents the worst case for a wind gust that is similar to a step disturbance.

The amplitude of the aerodynamic force due to the wind gust is estimated based on the experimental results of a low speed urban Maglev vehicle 1:12 scale model at Old Dominion University low speed wind tunnel [75]. This disturbing lateral force has an amplitude of 471.18N and is applied in the time interval from 8 to 20s. Figure 3.18 shows the lateral disturbing force profile.

A unified system configuration for both schemes is assumed. This system configuration has control inputs as the command currents I_{c_i} and outputs as the air gaps z_i, then the search algorithm will optimize the performance index $J(I_{c_i}, z_i)$ for both schemes to calculate the gain matrix. The gain matrix obtained is used directly with the de-centralized scheme, but for the centralized scheme, transformations should be applied to attain the proper gain matrix. This configuration is equivalent to having modes as outputs because, the air gaps and modes for this system are the same. The gain matrix for each scheme has dimension of 2×6. The necessity of having the same $J(G_c)$ for both de-centralized and centralized after n iterations is very difficult to achieve and requires changing the weights until the required result is achieved. The simulation scenario for both schemes is based on the system configuration where inputs are the command currents and the outputs are the air gaps, thus the minimization is performed on the performance index $J(I_{c_i}, z_i)$.

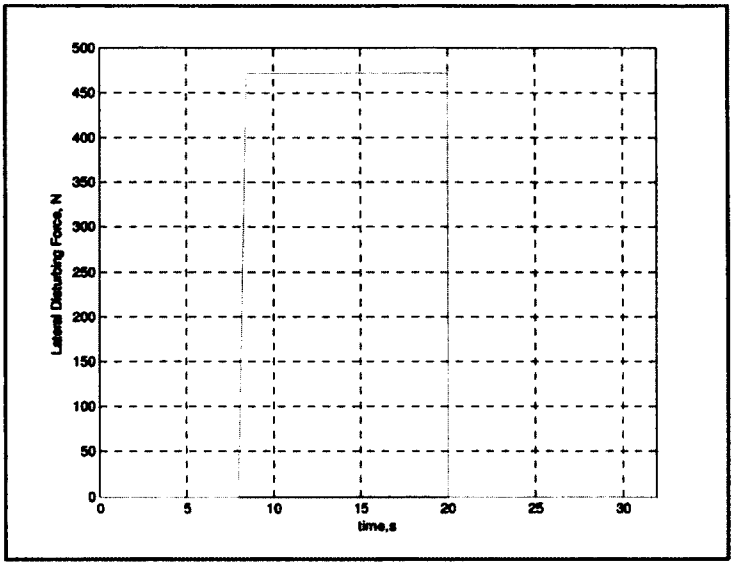

Figure 3.18. Lateral Disturbing Force

Figures 3.19 and 3.20 show the air gap and lateral responses of the 2-DOF Maglev system when PD de-centralized control is utilized. The lateral displacement due to disturbance is decreased to a value that is below 0.339mm after reaching to an amplitude of 0.95mm during the time interval 8 to 20s and this is due to the characteristics of the stable lateral poles and not due to the controller effect. Note that very low damping is noticed for the open loop lateral poles.

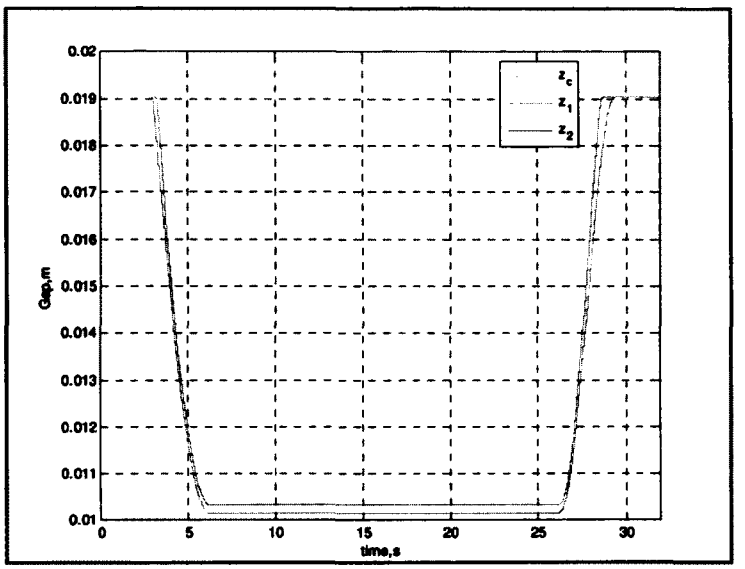

Figure 3.19. Air Gap Responses for the De-centralized Control-Rigid Case

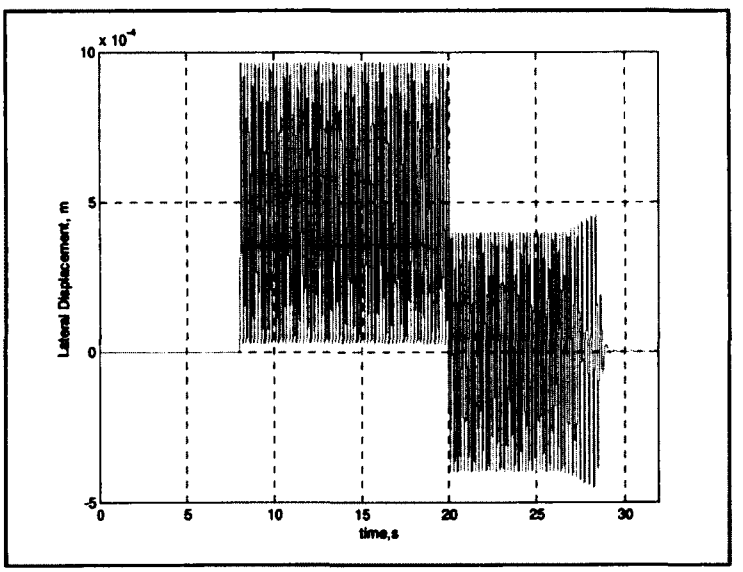

Figure 3.20. Lateral Displacement Response for the De-centralized Control-Rigid Case

A parametric time track is envisaged over the phase plane in addition to the time response for more analysis as shown in Figure 3.21, where the rate of lateral disturbance is plotted against the lateral disturbance from t=0 to 32 s. The system forms two stable elliptical limit cycles, the first one on the right corresponds to the reaction to the step response at

t=8 to 20s, and the second one on the left corresponds to the oscillation around the origin with $|y|=3.397\times10^{-4}$m, and $\left|dy/dt\right|=0.01092$m/s. In fact, the second limit cycle is composed of two perpendicular ellipses. One is for the oscillation around origin, and the second corresponds to the increased oscillations around origin that occurs before de-levitation in the time interval from t=26 to 28s. This is because, currents in electromagnets decrease causing weaker lateral force. It should be noted that the system will reach to origin at the end of the simulation as system de-levitates, so the amplitude of the lateral displacement is forced to zero.

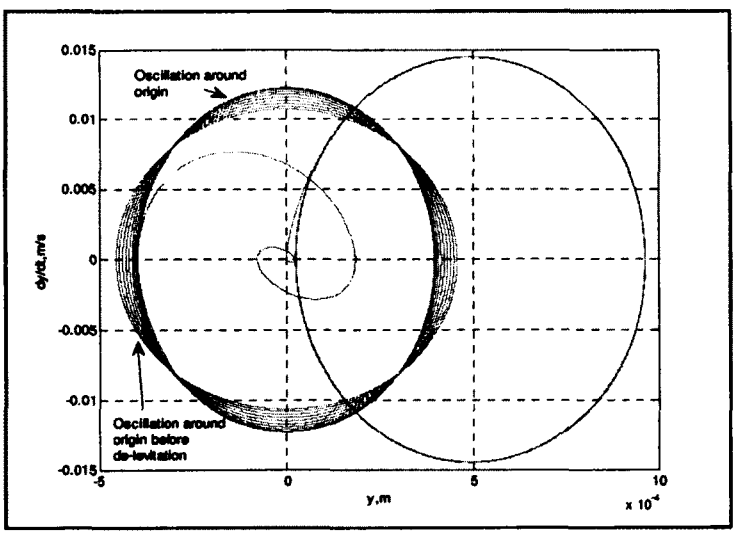

Figure 3.21. Phase Plane of Step Response for the De-centralized Control-Rigid Case

Figures 3.22, and 3.23 show the air gap and lateral responses of the 2-DOF Maglev system when PD centralized control is utilized. The same conditions are used for the system as have been used with the de-centralized controllers. The centralized controllers

overcome the lateral displacement that results due to the lateral disturbance force in a period of 1s.

A parametric time track is envisaged over the phase plane as shown in Figure 3.24 when PD centralized control is utilized. The system has two stable origins (limit cycles), the first one is on the right that returns to point ($y=8.695\times10^{-5}$m) in reaction to the lateral disturbance, the second point corresponds to the damped oscillation around origin. The system reaches equilibrium before de-levitation occurs. Both equilibrium points depicted in this simulation show the stable damping of the lateral displacement due to disturbance when PD centralized control is utilized.

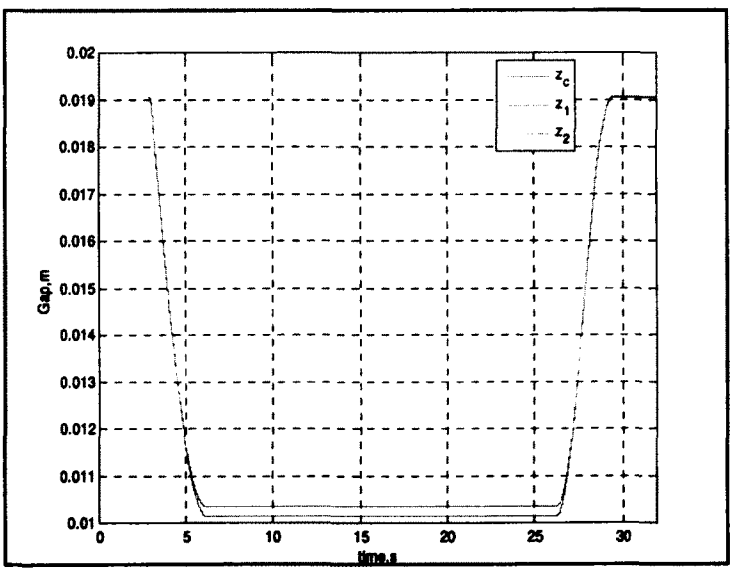

Figure 3.22. Air Gap Responses for the Centralized Control-Rigid Case

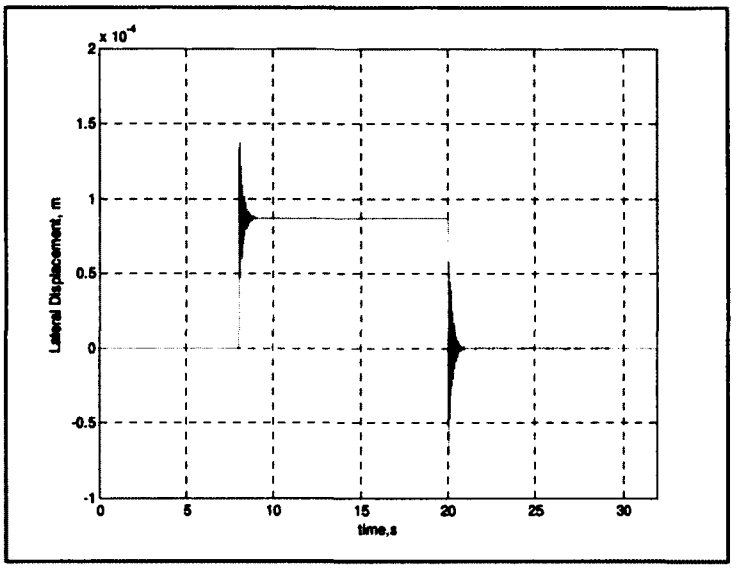

Figure 3.23. Lateral Displacement Response for the Centralized Control-Rigid Case

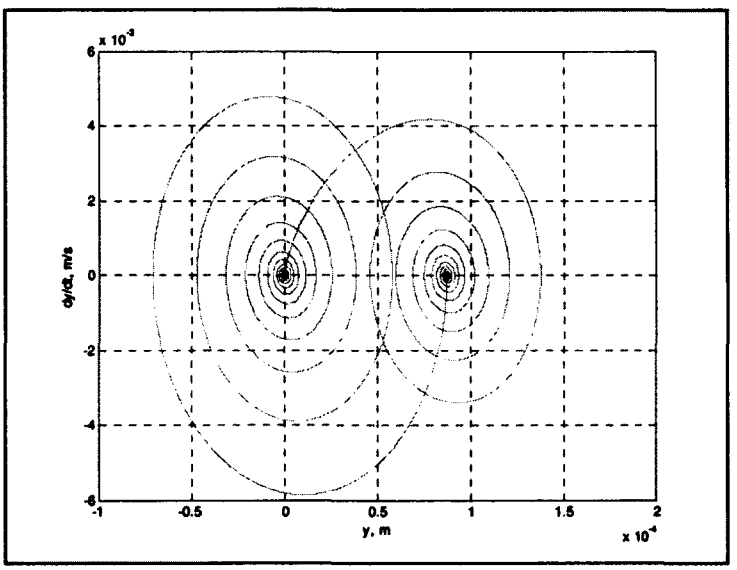

Figure 3.24. Phase Plane of Step Response for the Centralized Control-Rigid Case

To consider the flexible case of the 2-DOF EMS Maglev system, one vibration mode is considered which equals the ODU Maglev vibration mode 1, f_1=12.19Hz. The primary and secondary masses are 800kg, and 200kg, respectively.

Figures 3.25 and 3.26 show the air gap and lateral responses of the 2-DOF Maglev system-flexible case when PD de-centralized control is utilized. PD de-centralized control has stable behavior with the system as already proven in many references [2-4,7,9], but with low damping for the lateral displacements as received with the rigid case. The response of the lateral displacement due to disturbance decreased to 0.295mm after reaching an amplitude of 1mm during the time interval 8 to 20s of the disturbing lateral force. A low damping is achieved in the lateral channel as for rigid case.

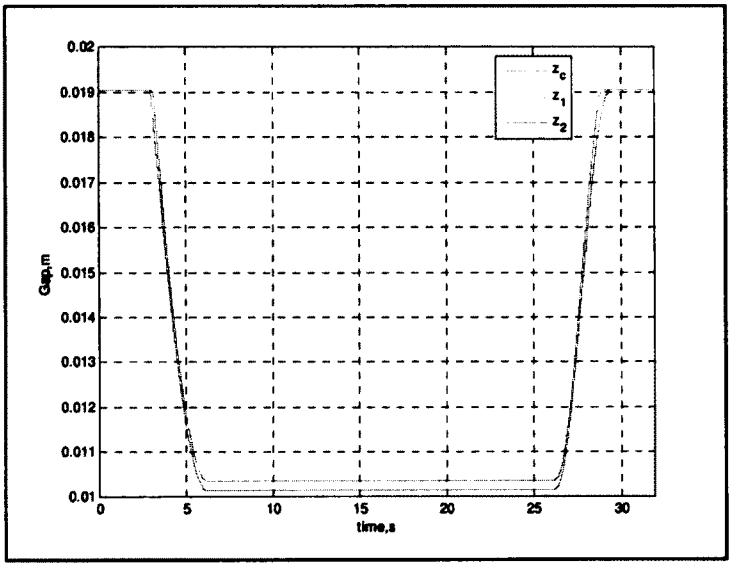

Figure 3.25. Air Gap Responses for the De-centralized Control-Flexible Case

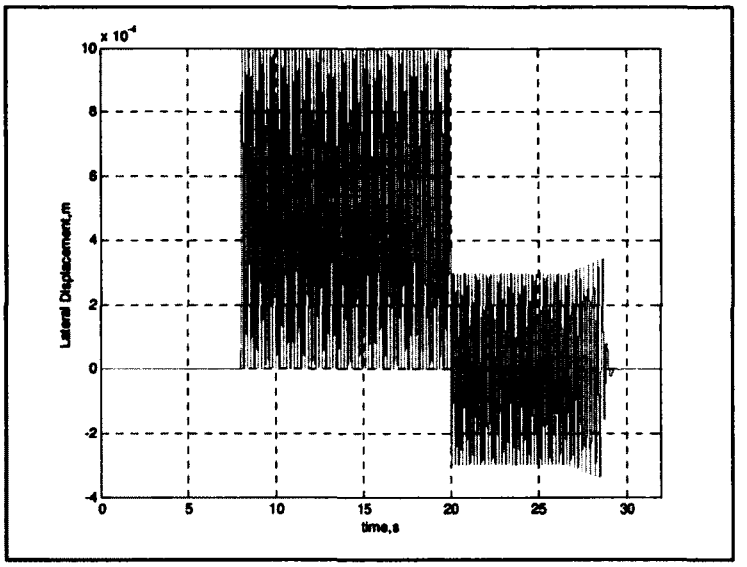

Figure 3.26. Lateral Displacement Response for the De-centralized Control-Flexible Case

Figures 3.27, and 3.28 show the air gap and lateral responses of the 2-DOF Maglev system-flexible case when PD centralized control is utilized. The centralized controllers attain stable behavior, good performance and overcome the lateral displacement that results from the lateral disturbance force, but with some damped oscillations that are due to the flexibility of the system as shown in Figure 3.28. This result coincides with the MIMO root loci of the PD centralized control with the flexible system case.

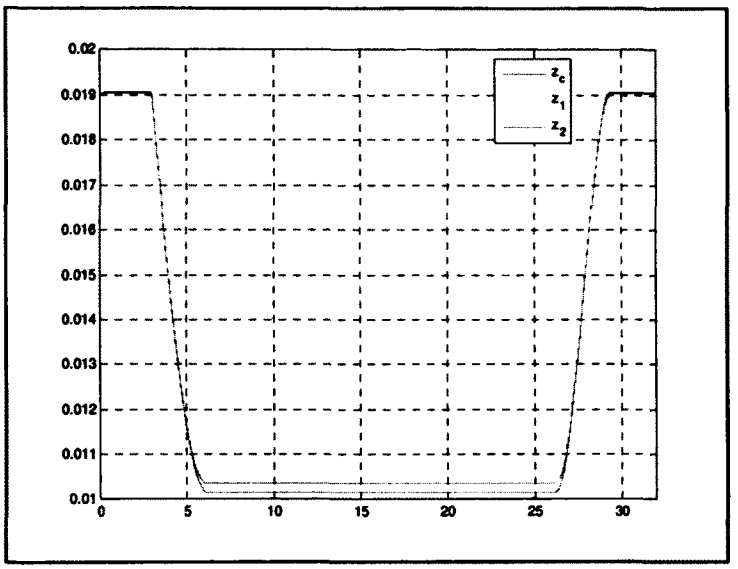

Figure 3.27. Air Gap Responses for the Centralized Control-Flexible Case

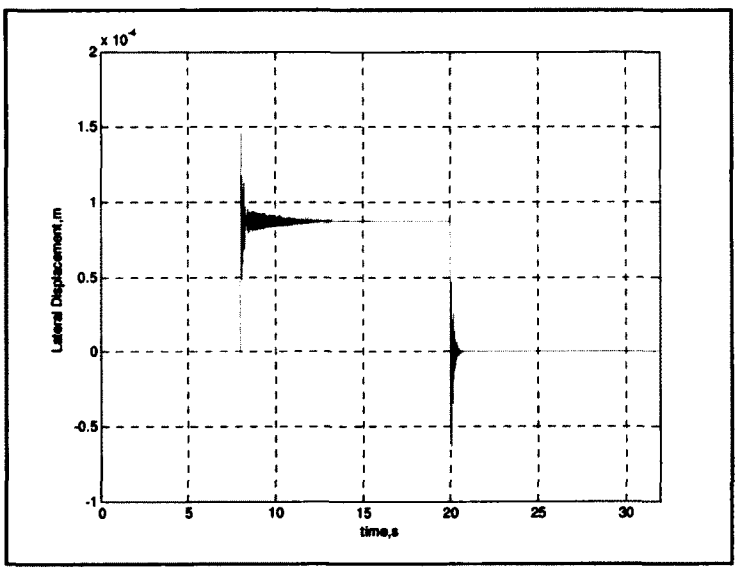

Figure 3.28. Lateral Displacement Response for the Centralized Control-Flexible Case

For both controller schemes when applied on the rigid and flexible cases, the air gap response was not affected by the lateral disturbance force although there is a considerable coupling between heave and lateral channels. This is due to the appropriate design of the controllers.

The responses achieved with both schemes can be practically enhanced when an integrator term is added to each controller to have PID control instead that reduces the steady state error.

3.6 Conclusions

In this chapter, a linearized model for the 2-DOF EMS Maglev system for an inverted U-rail is introduced. The PD de-centralized and centralized control schemes are applied on that model for rigid and flexible cases. For the de-centralized scheme, RGA Bode plots are made for zero stagger, and the controller is able to control the flexible case easier than the rigid due to reduced interactions received with the flexible case. For the centralized scheme, RGA Bode plots are made for different staggers, the heave and lateral channels are decoupled, and the controller is able to control system rigid and flexible cases. The multivariable controller design procedure used for the uncoupled systems is applied on the de-centralized controller design but with some tuning to overcome interaction. The linear stability investigation for the system uncoupled channels is introduced. This analysis shows that the lateral channel can be stabilized by negative feedback control unlike the heave channel that needs positive feedback control to be stabilized. A sketch for the MIMO root loci for the system with the PD de-centralized control is shown to stabilize the system by moving the heave unstable pole to left, but has no effect on the lateral poles that are stable by nature. A sketch for the MIMO root loci for the system with the PD centralized control is shown to stabilize the system by moving the heave unstable pole to left, and also affects the marginally stable lateral poles by making them more stable.

An LQR gradient like search algorithm for the MIMO PID controller gain tuning is introduced. This optimal algorithm is useful to tune the PD de-centralized and centralized controller gains on a unified criterion to have fair comparison.

The simulation results for the nonlinear 2-DOF EMS Maglev system rigid and flexible cases with the PD de-centralized and centralized controllers show that the PD centralized controller is better than the de-centralized one when the system is exposed to a lateral disturbing force such as wind gusts. This is due to the effectiveness of the centralized control on the lateral poles than the de-centralized control that has no effect on the lateral poles.

As a matter of fact, when using de-centralized control, lateral motion control is attained passively while with the centralized control, lateral motion control is achieved actively. This lateral control is achieved by having magnet staggers, so each magnet will provide with a lateral force in the direction opposite to the stagger that diminishes the lateral displacements due to the lateral disturbance.

Finally, insight on the difference between these two commonly used control schemes, especially if a particular concern is given to lateral control, is provided. The centralized control was shown to achieve better lateral control than the de-centralized control for both rigid and flexible cases of the Maglev system. This study is useful for real systems like the ODU Maglev and can be generalized to decide which control scheme to be utilized considering the conditions that the real EMS Maglev system is exposed to.

CHAPTER 4

DE-CENTRALIZED AND CENTRALIZED CONTROL FOR ODU EMS MAGLEV TEST BOGIE

4.1 Introduction

In this chapter, de-centralized and centralized control for the ODU EMS Maglev test bogie is presented. A full description on the ODU Maglev test bogie experimental setup that describes the bogie structure and the utilized hardware is introduced. The complete structural model for the ODU EMS Maglev bogie is presented. The EMS Maglev electrodynamics and track/girder dynamics modeling are introduced. A detailed description on the de-centralized and centralized control for that typical system is introduced. Numerical simulation and experimental results for the system with these controllers are also shown. Details on flux feedback control technique and how to combine with de-centralized and centralized controllers for stability improvement and noise reduction are described. Numerical simulation results for the combined flux feedback/de-centralized and combined flux feedback/centralized controllers with the Maglev bogie are shown.

4.2 ODU Maglev Test Bogie Experimental Setup

The ODU Test bogie, shown in Figure 4.1, is a welded aluminum structure [3]. This test bogie is equipped with amplifiers, filters, sensors, actuators and on board computer. Power amplifiers feed current to each of the six electromagnet coils. Eddy-current based position sensors and accelerometers are used to measure the vertical positions and vertical accelerations of the magnets, respectively, two laser sensors are used to measure the lateral positions, and an 8-pole Butterworth anti-aliasing filter along with a digital

low-pass filter is used to filter the noise in the measurement signals. A National Instruments data acquisition card installed in a PC104-Plus computer is used for data acquisition and control. The data acquisition system is operated through MATLAB/SIMULINK, using the xPC Target environment. Relevant system parameters are listed in Table 4.1. The sampling rate is 10 kHz.

Table 4.1 ODU Test Vehicle Parameters

Detail	Value	Units
Mass	2.267×10^{3}	Kg
Length	3.65	m
Width	1.52	m
Height	0.91	m
Mass moment of Inertia (I_{xx})	2.955×10^{3}	$Kg.m^2$
Mass moment of Inertia (I_{yy})	3.842×10^{3}	$Kg.m^2$
Mass moment of Inertia (I_{zz})	1.207×10^{3}	$Kg.m^2$
Desired Magnetic Gap	0.01	m
No. of Magnets	6	-
No. of Amplifiers	6	-
No. of LIMs	2	-
No. of Turns per magnet	596	turns
Resistance of the magnet coil	1.83	Ohm
Inductance of the magnet coil	0.68	H
Electromagnet pole length	0.381	m
Electromagnet pole width	0.051	m
Air permeability constant	$4\pi\times10^{-7}$	N/A^2
Gauge number	10	-

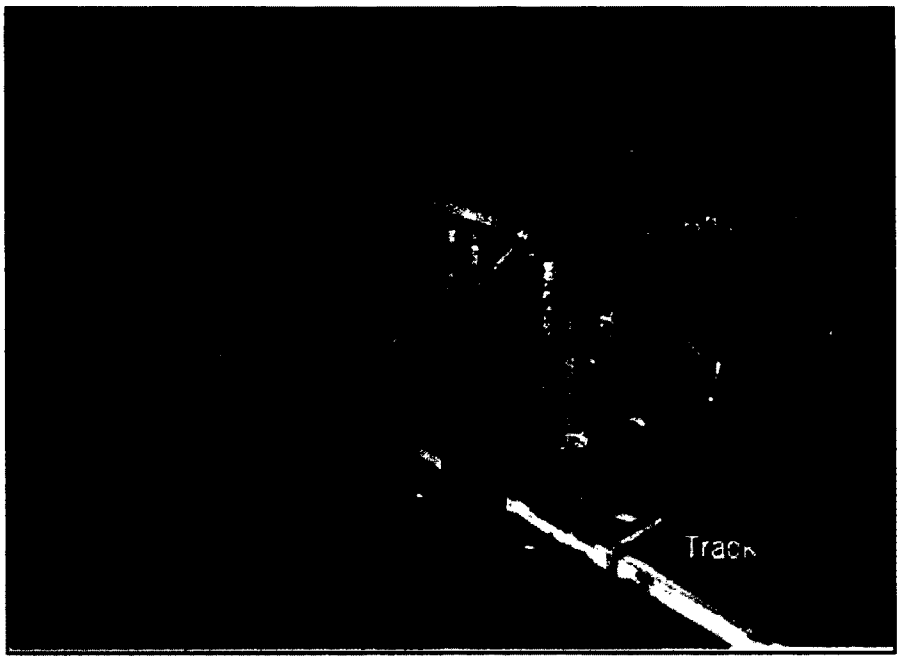

Figure 4.1. ODU Maglev Test Bogie in Lab

4.3 Structural Model

4.3.1 Models for Rigid Body and Flexible Systems

The test bogie model that is utilized in this chapter is based on the previous research work conducted in [3-4]. The dynamic model of the bogie includes rigid body and structural vibration modes. The rigid body dynamic model has five degrees of freedom – two translational and three rotational. The sixth degree of freedom that represents the forward motion is not modeled. The flexible body dynamic model has infinite degrees of freedom (modes). However, only a few flexible modes need to be considered for model development. The test bogie uses six electromagnets that are located under the tracks for levitation, and for modeling considerations, the levitation and lateral forces generated by each magnet are considered. The moments generated by these forces around the bogie's center of mass are also considered. A Finite Element (FE) structural model for the

vehicle has been developed, from which the mass and inertia properties, basic geometry, and location of the magnets with respect to the center of mass are obtained. The mode shapes and eigenvalues of the bogie for selected modes are also obtained from the FE model. The dynamical model for a generic flexible structure with rigid body modes and a finite number of flexible modes of vibration is [3-4][48]:

$$A_s\ddot{p} + B_s\dot{p} + C_s p = -\Gamma^T u \tag{4.1}$$

where, A_s is the mass-inertia matrix (always positive definite) given by

$$A_s = \begin{bmatrix} m_s & 0 & 0 \\ 0 & J_s & 0 \\ 0 & 0 & I_{nq} \end{bmatrix} \tag{4.2}$$

m_s is the total mass of the structure and it is a 3×3 diagonal matrix (for translational motions along x, y and z directions), J_s is a 3×3 moment of inertia matrix, I_k denotes the $k\times k$ identity matrix, and n_q is the number of flexible modes of vibration considered. The reason for the negative sign on right hand side of Eq. (4.1) is because the applied force is opposite to that of the measured gap.

$$p^T = \begin{bmatrix} x_{rb}^T & q_v^T \end{bmatrix},\ x_{rb} = \begin{bmatrix} \xi^T & \gamma^T \end{bmatrix}^T \tag{4.3}$$

where, ζ and γ represent the rigid body translation and rigid body rotation vectors, respectively. q_v is the $n_q\times1$ modal amplitude vector (modal co-ordinate vector). Thus, p represents all the modeled degrees of freedom (rigid and flexible) of the structure.

$$B_s = diag\begin{bmatrix} 0_{3\times3} & 0_{3\times3} & D_{n_q\times n_q} \end{bmatrix} \tag{4.4}$$

where, D is $n_q \times n_q$ symmetric matrix that represents the inherent structural damping, and $0_{k\times k}$ is the null matrix. The modal matrix is assumed to be mass normalized, therefore

each element in the D has the form $D_{ii} = 2\xi_i\omega_i$, where ξ_i and ω_i represent the inherent damping ratio and natural frequency of the i^{th} flexible mode. As D is always assumed to be greater than zero for any structural damping, then B_s is positive semi-definite. Similarly, is also C_s positive semi-definite:

$$C_s = diag\begin{bmatrix} 0_{3\times3} & 0_{3\times3} & \Lambda_{n_q\times n_q} \end{bmatrix} \tag{4.5}$$

where, Λ is the diagonal matrix of squared flexible mode frequencies with $\Lambda_i = \omega_i^2$, the mode shape matrix is:

$$\Gamma^T = \begin{bmatrix} I_{3\times3} & I_{3\times3} & \cdots & I_{3\times3} \\ \tilde{R}_1 & \tilde{R}_2 & \cdots & \tilde{R}_m \\ \Psi_1^T & \Psi_2^T & \cdots & \Psi_m^T \end{bmatrix} \tag{4.6}$$

In Eq. (4.6), m is the number of applied forces, Ψ_i^T is the modal matrix. $\tilde{R}_i$ is the cross product matrix of position vector of the i^{th} force applying actuator. The number of rows of Ψ_i^T is equal to the number of flexible modes selected to be modeled. Each Ψ_i^T has two columns since each electromagnetic force has two components: levitation and lateral. The moment generated by the i^{th} force f_i about the center of gravity of the vehicle can be written as:

$$M_i = r_i \times f_i = \begin{bmatrix} 0 & -r_{zi} & r_{xi} \\ r_{zi} & 0 & r_{yi} \\ -r_{xi} & r_{yi} & 0 \end{bmatrix} \begin{bmatrix} f_{x_i} \\ f_{y_i} \\ f_{z_i} \end{bmatrix} \tag{4.7}$$

where, $r_i = \begin{bmatrix} r_{xi} & r_{yi} & r_{zi} \end{bmatrix}^T$ represents the position vector to the i^{th} force f_i.

If the levitation and lateral forces are only considered, then Eq. (4.7) will be

$$M_i = \begin{bmatrix} R_i \end{bmatrix} \begin{bmatrix} f_{yi} \\ f_{zi} \end{bmatrix} \tag{4.8}$$

where, $[R_i]=\begin{bmatrix} -r_{zi} & -r_{xi} \\ 0 & -r_{yi} \\ r_{yi} & 0 \end{bmatrix}$ represents the columns of the cross-product rotation matrices that correspond to the i^{th} force f_i, and the force $f_i=\begin{bmatrix} f_{yi} \\ f_{zi} \end{bmatrix}$.

The control input vector u of the applied levitation and lateral forces then is

$$u=\lfloor f_{y1} \quad f_{z1} \quad \cdots \quad f_{ym} \quad f_{zm} \rfloor = F \tag{4.9}$$

The outputs are considered to be the vertical positions of the magnets, and two lateral positions of the vehicle. Therefore, the outputs are

$$y_o = \Gamma p \tag{4.10}$$

The relation between the air gaps and the magnet positions is

$$z = y_o - y_t \tag{4.11}$$

where, y_o is the position to the magnet and y_t is the position to the track.

Eq. (4.1) is combining the rigid body and flexible modes together and they can split by considering the equations for rigid body modes (translation and rotation), and equation for the flexible modes.

A conventional method for modeling the test bogie dynamics is by using Newton's laws. So, the dynamics of the rigid body translation dynamics are found via the following equations of motion [3]:

$$m_s \ddot{\sigma} = \sum_{i=1}^{6} f_i \tag{4.12}$$

m_s is the mass of the test-bogie and σ represents the two rigid body translation vector (heave and lateral). The summation is up to six elements because, the test bogie has six electromagnets.

In the same way, the rigid body rotation dynamics are:

$$I_r\ddot{\varepsilon} = \begin{bmatrix} R_1 f_1 & R_2 f_2 & \dots & R_6 f_6 \end{bmatrix} \cong Rf \tag{4.13}$$

where, ε represents the three rigid body rotation vectors (roll φ , pitch ϑ ,and yaw ψ). R_i represent the columns of the cross-product rotation matrices corresponding to the i^{th} force f_i. The flexible modes (elastic motion) can be modeled in similar manner as in [48]:

$$\ddot{q}_v + D_t\dot{q}_v + \Lambda_t q_v = \Psi^T F \tag{4.14}$$

where q_v represents the modal co-ordinates, or modal vectors. The matrix Ψ is

$$\Psi^T = \begin{bmatrix} \phi_{z_1}^T & \phi_{z_2}^T & \dots & \phi_{z_6}^T \end{bmatrix} \tag{4.15}$$

where, $\phi_{z_i}^T$ are the z-columns of the mode shape matrix corresponding to the i^{th} force applying actuator.

D_t is the $n \times n$ diagonal matrix representing the inherent damping in the structure. This modal matrix is also assumed to be mass-normalized; therefore, each element in D_t matrix can be written as $D_{t_i} = 2\varsigma_i\omega_i$, where ς_i and ω_i represent the inherent damping ratio and natural frequency of the i^{th} flexible mode. Λ_t is the diagonal matrix of the squared flexible mode frequencies, with $\Lambda_{t_i} = \omega_i^2$.

For the ODU Maglev bogie, four flexible modes are considered in modeling. Eqs. (4.12-14) represent the complete model of the bogie that includes rigid and flexible modes.

4.3.2 State Space Representation

The state space model of a flexible structure can be expressed as [3]:

$$\begin{aligned} \dot{x} &= Ax + Bu \\ y &= Cx \end{aligned} \tag{4.16}$$

where,

$$x = \begin{bmatrix} x_{rb}^T & q_v^T & \dot{x}_{rb}^T & \dot{q}_v^T \end{bmatrix}^T \tag{4.17}$$

x is the state vector that define the states of the rigid body, flexible displacements and the corresponding velocities.

The control input vector u in Eq. (4.16) is the applied force vector as in Eq. (4.9). The outputs in Eq. (4.16) represent the magnet positions. For the co-located sensor and actuator configuration the outputs have the form:

$$y = \Gamma p = Cx \tag{4.18}$$

then, the state space matrices are

$A = \begin{bmatrix} A_r & 0 \\ 0 & A_f \end{bmatrix}$ is the dynamics matrix.

where, $A_r = \begin{bmatrix} 0 & 0 & I & 0 \\ 0 & 0 & 0 & I \\ 0 & 0 & 0 & 0 \\ 0 & 0 & 0 & 0 \end{bmatrix}$, and $A_f = \begin{bmatrix} 0 & I \\ -\Lambda & -D \end{bmatrix}$

$B = \begin{bmatrix} B_r \\ B_f \end{bmatrix}$ is the input matrix.

where, $B_r = \begin{bmatrix} 0 & 0 & \dots & 0 \\ 0 & 0 & \dots & 0 \\ m_s^{-1} & m_s^{-1} & \dots & m_s^{-1} \\ I_s^{-1}R_1 & I_s^{-1}R_2 & \dots & I_s^{-1}R_6 \end{bmatrix}$, and $B_f = \begin{bmatrix} 0 & 0 & \dots & 0 \\ \Psi_1^T & \Psi_2^T & \dots & \Psi_6^T \end{bmatrix} \equiv \begin{bmatrix} 0 \\ \Psi^T \end{bmatrix}$

$C = \begin{bmatrix} C_r & C_f \end{bmatrix}$ is the output matrix.

where $C_r = \begin{bmatrix} I & \tilde{r}^T & 0 & 0 \end{bmatrix}$ and $C_f = \begin{bmatrix} \Psi & 0 \end{bmatrix}$

The parameters shown above are obtained using the finite element model of the test bogie that is described in [3].

4.4 Electrodynamics

The electromagnets' electrodynamics are included here as described in section 2.3.3. The magnet inductance in terms of y and z is has the following relationship:

$$L_{m_i}(y,z) = \frac{\mu_o N^2 Lw}{2z_i}\left\{1 + \frac{2z_i}{\pi w}\left[1 + \frac{1}{2}\ln\left(1 + \left(\frac{y_j}{z_i}\right)^2\right) - \frac{y_j}{z_i}\tan^{-1}\frac{y_j}{z_i}\right]\right\} \quad \begin{matrix} i = 1,2..,6 \\ j = 1,2 \end{matrix} \tag{4.19}$$

From Eq. (4.19), it is noted that the magnet inductance is a function in y and z, but z has more influence on the inductance than y as shown in the equation.

Using Kirchhoff's voltage law, the voltage applied to the coil of each electromagnet is

$$V_i = RI_i + L_{m_i}(y,z)\frac{dI_i}{dt} - L_{mi}(y,z)\frac{I_i}{z_i}\frac{dz_i}{dt}, \; i = 1,..,6 \tag{4.20}$$

In fact, each electromagnet is driven by current amplifier that is intended to track a current command I_{c_i} with an amplifier feedback gain K_A.

$$V_i = K_A(I_{c_i} - I_i), \; i = 1,..,6 \tag{4.21}$$

Combining Eq. (4.21), and Eqs. (4.19-20), the final current loop is:

$$\dot{I} = \frac{K_A}{L_{m_i}}\left(I_{c_i} - I_i\right) - \frac{R_i I_i}{L_{m_i}} - \frac{I_i \dot{z}_i}{z_i}, i = 1,2,...,6 \tag{4.22}$$

The linearized format of the current equation is:

$$\dot{I} = \frac{K_A}{L_{m_i}} I_{c_i} - \left(\frac{K_A + R_i}{L_{m_i}}\right) I_i, i = 1,2,...,6 \tag{4.23}$$

and for large magnets, L_{m_i} can be considered as constant.

4.5 Track/Girder Dynamics

The dynamics of the ODU concrete girder is shown in Figure 4.2 as a frequency response (Bode) diagram [3]. As in [3], the data that plotted in the Figure is obtained

using (a) the FE model of the girder, (b) experimentally by testing the girder, and (c) analytically for a simply-supported-beam model. The ODU girder can be reasonably modeled as a simply supported beam for which the equations of motion are very well known [21]. More details on the girder modeling are in Chapter 5.

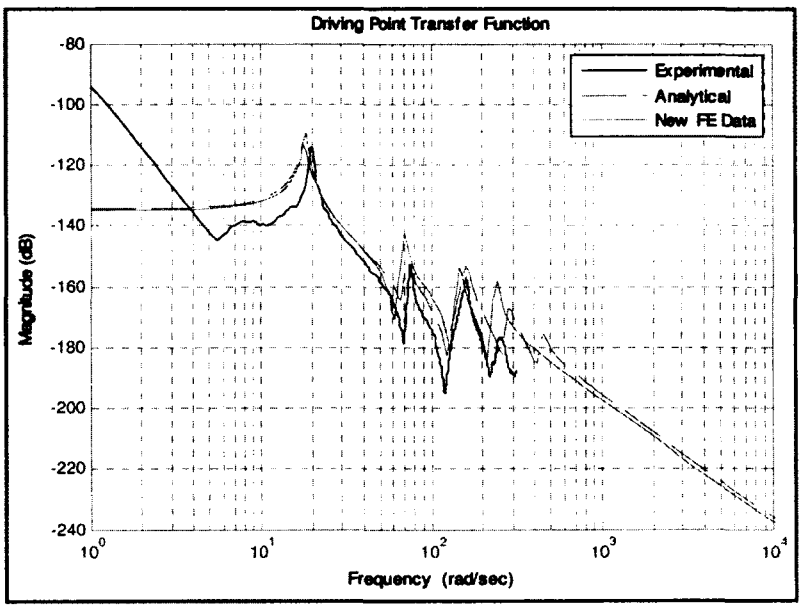

Figure 4.2. ODU Girder Frequency Response Comparison

4.6 De-centralized Controller Design

4.6.1 De-centralized Controller Scheme

In the de-centralized control scheme, controllers are designed locally for each input-output pair as co-located actuators and sensors as shown in Figure 4.3. De-centralized control means that each magnet has its own control loop that is independent of other control loops [2-4,13,46]. Each controller is based on the magnet's vertical position, vertical velocity and vertical acceleration, and has been designed to have sufficient damping. The control logic aims to maintain the magnetic gap to a pre-set value z_c. In this

approach, the outputs (local measurements) are fed back into local PID controllers; one for each magnet. These controllers are:

$$I_{c_i} = K_{P_{i_z}} e_n + K_{I_{i_z}} \int e_i dt + K_{D_{i_z}} \dot{e}_i, i = 1,2,..,n$$
$$e_i = z_{ci} - z_i \tag{4.24}$$

where n is the number of electromagnets, z_c: is the command air gap and the controller's proportional, integral and derivative gains are $K_{P_{n_z}}$, $K_{I_{n_z}}$, and $K_{D_{n_z}}$, respectively. In Figure 4.3, the E.M block represents the electromagnetic dynamics as in Eq. (4.22).

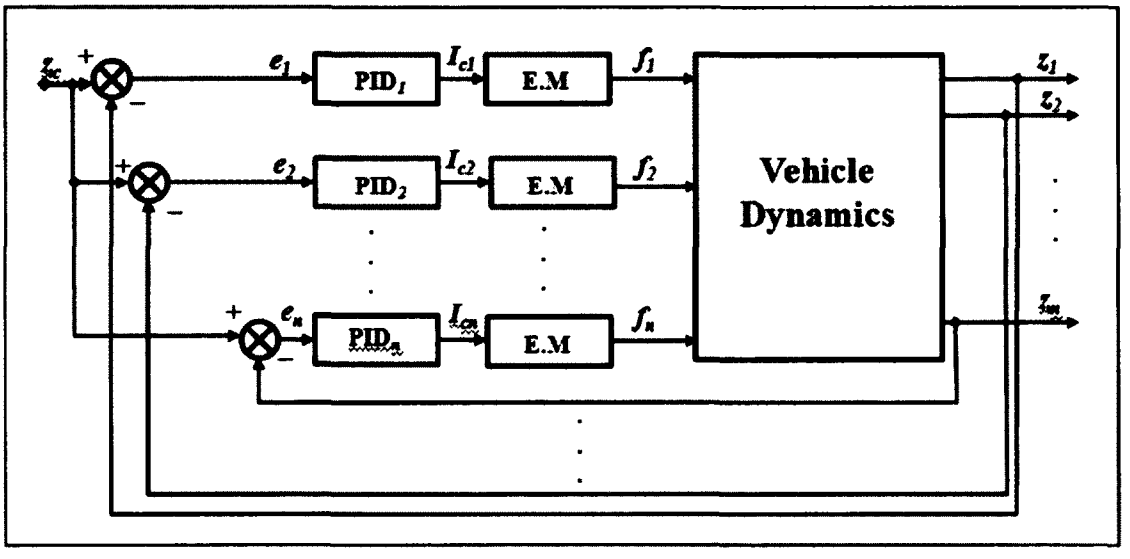

Figure 4.3. De-centralized Controller

Since the EMS Maglev system is an open loop unstable by nature, the utilized individual controllers have positive feedback configuration. This configuration has proven a guaranteed stability for rigid and flexible EMS Maglev systems [2,7,9]. The trial and error method is used to determine the gains of the PID controllers using MATLAB/SIMULINK simulation.

4.6.2 Combined De-centralized-Flux Feedback Control

In this section, the combined de-centralized-flux feedback is considered. A minor modification on Eq. (2.53) that is used in Chapter 2 to calculate the magnetic field density is utilized to include the lateral measurement y. Then the nonlinear expression for the magnetic field density measurement is:

$$B = \frac{P(y,z)NI}{A} = \frac{\mu_o NI}{2z}\left\{1 + \frac{2z}{\pi w}\left[1 + \frac{1}{2}\ln\left(1 + \left(\frac{y}{z}\right)^2\right) - \frac{y}{z}\tan^{-1}\frac{y}{z}\right]\right\} \tag{4.25}$$

In order to calculate the linearization coefficients $k_{\Phi I i}$, and $k_{\Phi z i}$, i=1,2,...,6 that are necessary for the flux feedback gain k_{Φ_i} calculation, the steady state currents $I_{o_1}, I_{o_2}, ..., I_{o_6}$, and gaps $z_{o_1}, z_{o_2}, ..., z_{o_6}$ are to be used. Having suitable flux feedback gains calculated as in Chapter 2, the inner loops for the flux measurements are closed as shown in Figure 4.4. The output of the flux controller block $I_{B_1}, I_{B_2}, ..., I_{B_6}$ is fed back in the inner loops as shown in Figure 4.4 to make the system marginally stable. The command currents to the amplifiers $I_{c_1}, I_{c_2}, ..., I_{c_6}$ are the result of subtracting the output of the flux controller from the PID controllers output $I_{co_1}, I_{co_2}, ..., I_{co_6}$ as shown in Figure 4.4.

In order to complete the controller design, the trial and error method is used to determine the gains of the PID controllers in the outer loops via MATLAB/SIMULINK simulation environment. The gains of the combined de-centralized flux feedback PID controllers are totally different than those used for the de-centralized control. In Figure 4.4, the block diagram of the combined de-centralized flux feedback control is shown.

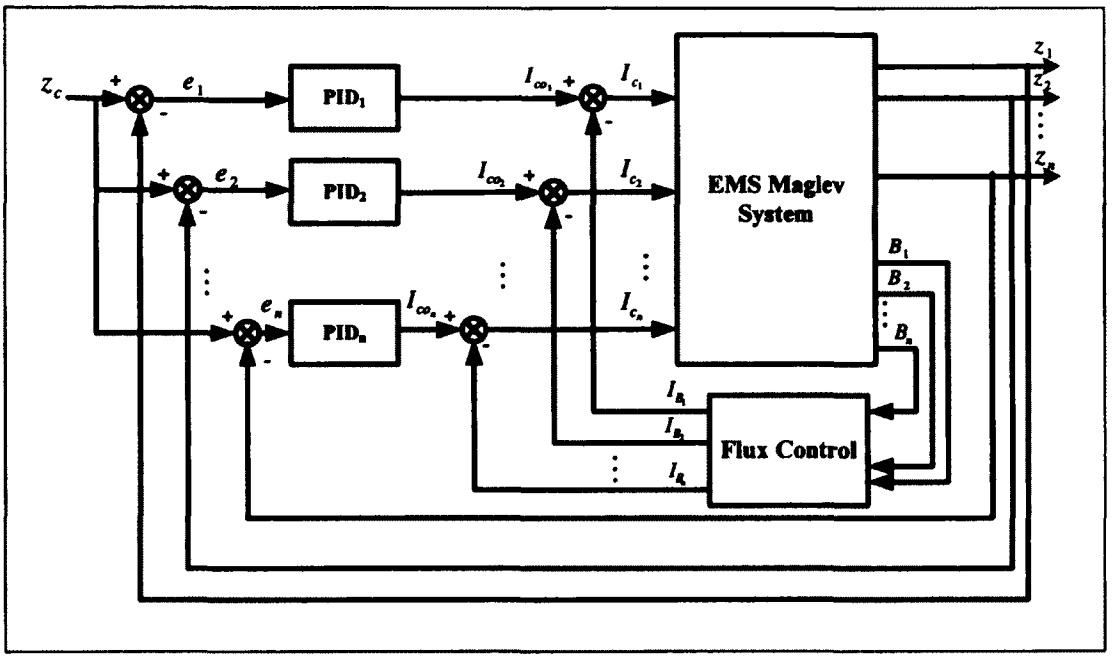

Figure 4.4. Combined De-centralized-Flux Feedback Control

4.6.3 Maglev Real-Time Control

The real-time control of the ODU Maglev system is performed based on xPC Target environment. xPc Target enables to execute SIMULINK models on target computer for the hardware-in-the loop (HIL) simulation, control prototyping, and other real-time testing applications. It is possible to add I/O blocks to models, automatically generate code with Real-Time Workshop, and download the code to a second PC running the xPC Target real-time kernel [76].

The SIMULINK model that is used for the system's simulation purposes is now modified to consider the I/O blocks. In Figure 4.5, the SIMULINK code used to implement de-centralized control for the ODU Maglev bogie is shown.

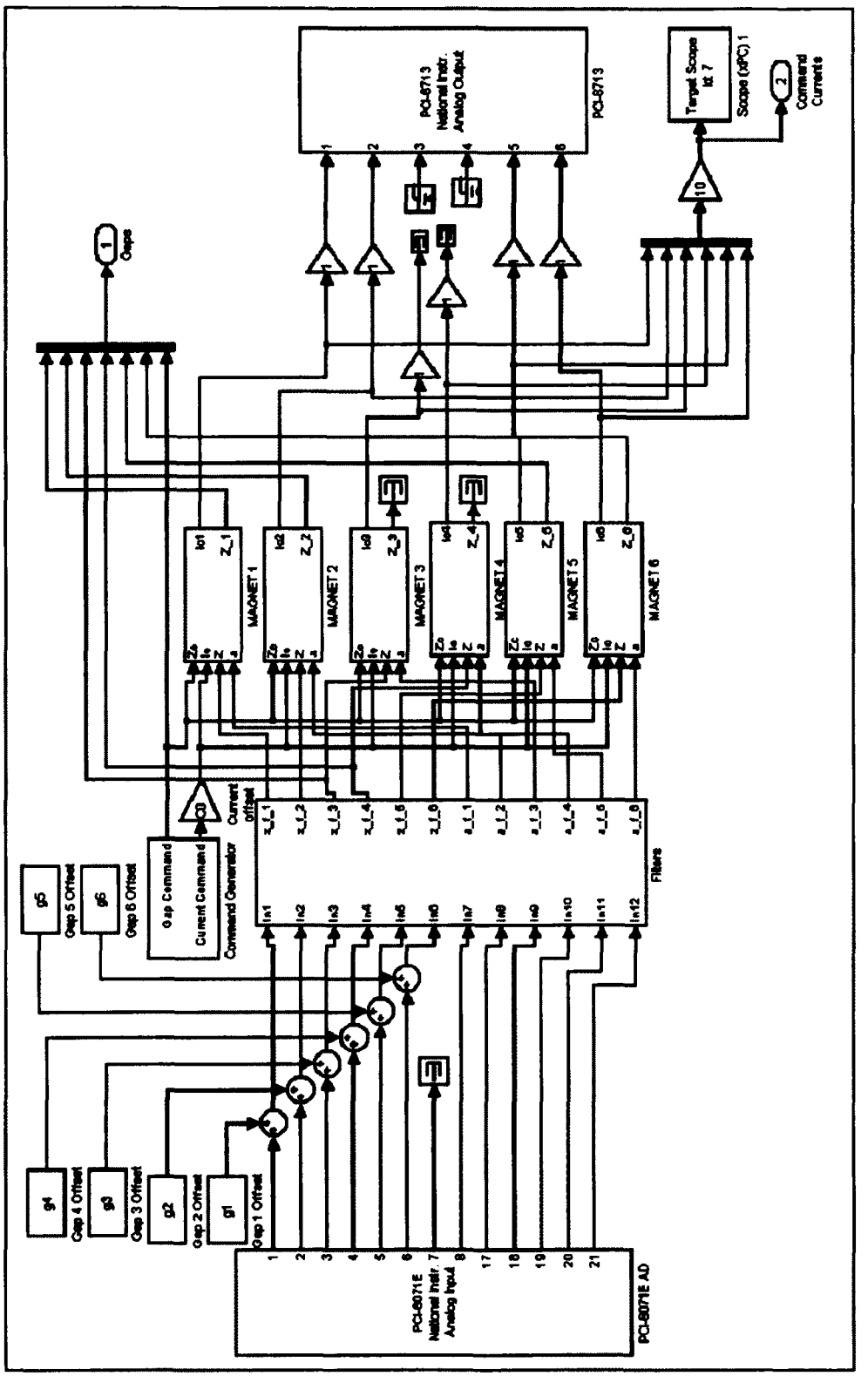

Figure 4.5. The xPC Target-SIMULINK Block Diagram Used for Test Bogie Levitation

On the left, the data acquisition input block PCI-6071E is used to acquire both position and acceleration data. The first six outputs of this block are the air gaps measured by position sensors (voltages). The last six outputs are the accelerometer measurements (voltages). The filters' block is next to PCI-6071E and used to filter the air gap and accelerometer signals from exciting the first bending mode of the track, which is around 57 Hz. The command generator block generates the command signals for the levitation gaps as well as the nominal currents [3]. These command signals and the filtrated signal are input to the de-centralized PID controller blocks (MAGNET 1 to MAGNET 6).

The output of these PID controller blocks are input to the amplifiers through another data acquisition card PCI-6713. In the diagram shown, only 4 magnets (Magnets #1, 2, 5 and 6) were used for levitation.

4.6.4 Simulation and Experimental Results

Case 1-a

In this section, case 1-a, in which normal levitation for the ODU EMS Maglev system with de-centralized control, is studied. The simulation results for the ODU EMS Maglev vehicle with the de-centralized control for case 1-a are shown in Figures 4.6- 4.7. In the de-centralized control, the Maglev bogie mass distribution is considered as each air gap is controlled individually. This means that each PID controller is multiplied with a certain weight that is related to the bogie mass distribution. The simulation results show that the PID de-centralized controller is capable of stabilizing the EMS Maglev system.

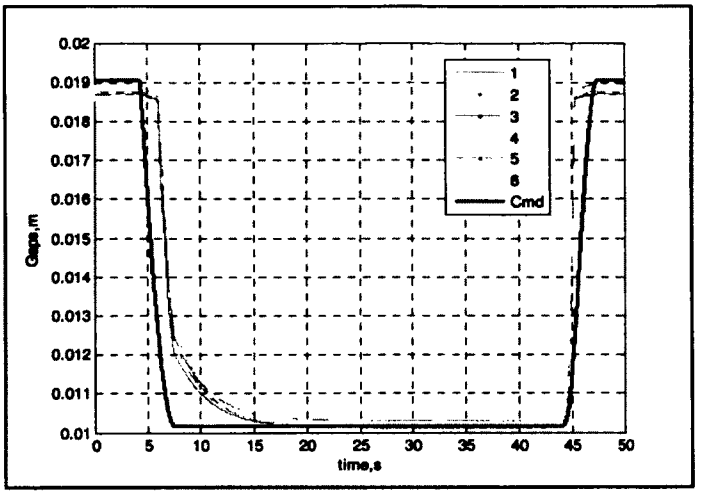

Figure 4.6. ODU Vehicle Air Gap Response with the De-centralized Control (Case 1-a)

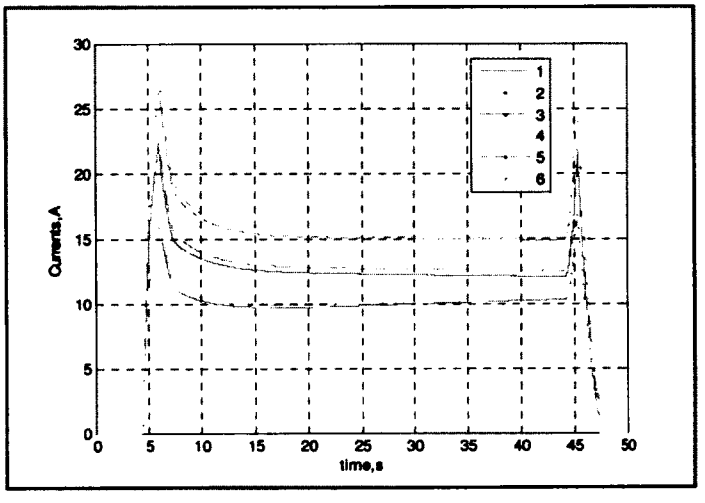

Figure 4.7. Currents in Electromagnets for De-centralized Control (Case 1-a)

Case 2-a

In this section, case 2-a is considered in which a lateral offset of 2mm is considered as initial condition and the Maglev system is released after 6 seconds. To have that, the effect of the lateral stiffness is neglected in the time interval from 0 to 6s. The simulation results for the ODU EMS Maglev vehicle with the de-centralized control is shown in

Figures 4.8, and 4.9. The air gap response is affected due to the interaction between heave and lateral dynamics. The lateral motion response starts at 2mm and starts to decay slowly by the end of levitation at t=45s when it still has a value of 0.45mm peak to peak [77]. The current in electromagnets are shown in Figure 4.10.

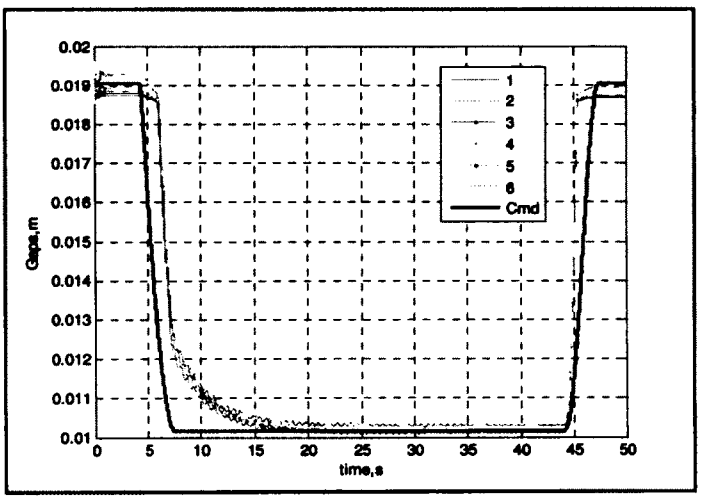

Figure 4.8. ODU Vehicle Air Gap Response with the De-centralized Control

(Case 2-a)

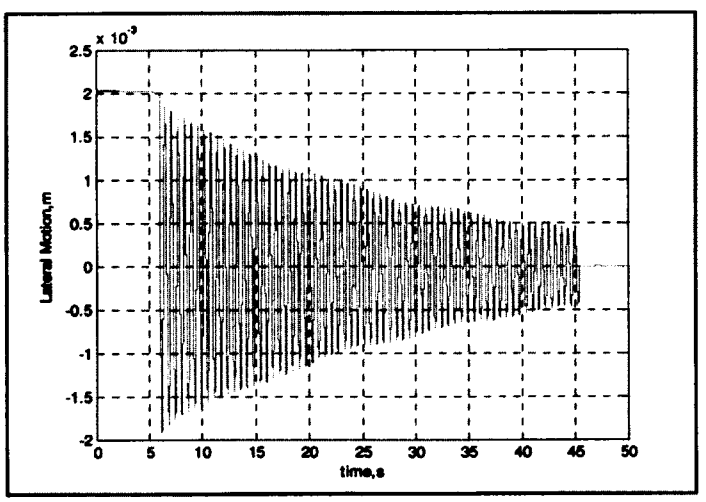

Figure 4.9. ODU Vehicle Lateral Motion Response with the De-centralized Control

(Case 2-a)

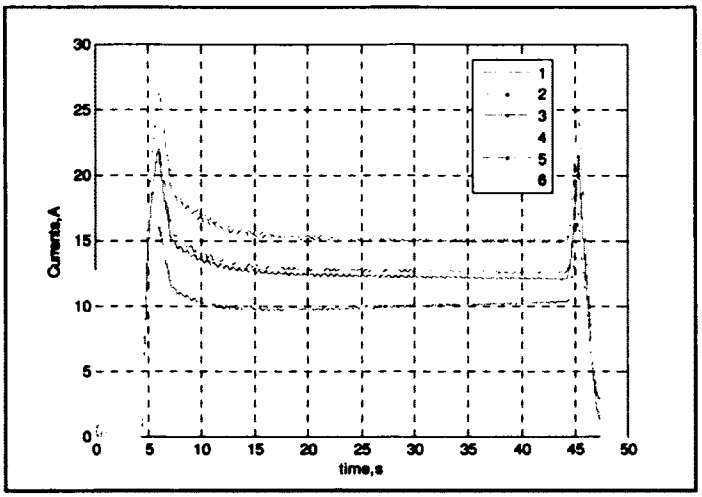

Figure 4.10. Currents in Electromagnets for De-centralized Control (Case 2-a)

The simulation results of the ODU EMS Maglev system when de-centralized control is utilized similar to the 2-DOF EMS Maglev system results with slow lateral suppression as it is attained passively.

Case 3-a

In this section, case 3-a, in which normal levitation for the ODU EMS Maglev system with combined de-centralized flux feedback control, is studied. The simulation results for the ODU EMS Maglev vehicle with that controller are shown in Figures 4.11-4.13.

For the simulation purposes and by the aid of MATLAB/SIMULINK, the magnetic field density measurements are generated and shown in Figure 4.13. The order of the magnetic field density measurements is 0.25-0.62T.

The simulation results show that the combined de-centralized-flux feedback controller is capable of stabilizing the EMS Maglev system.

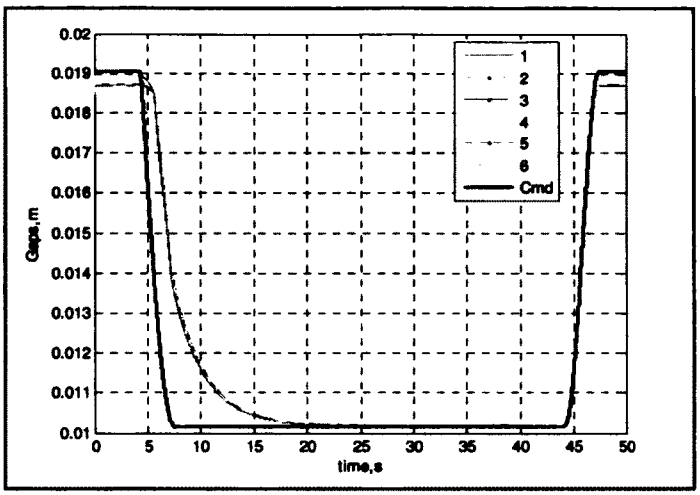

Figure 4.11. ODU Vehicle Air Gap Response with the De-centralized Control (Case 3-a)

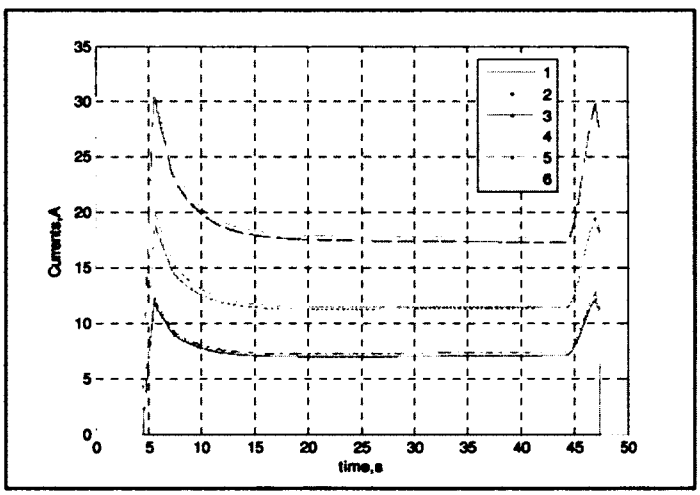

Figure 4.12. Currents in Electromagnets for De-centralized control (Case 3-a)

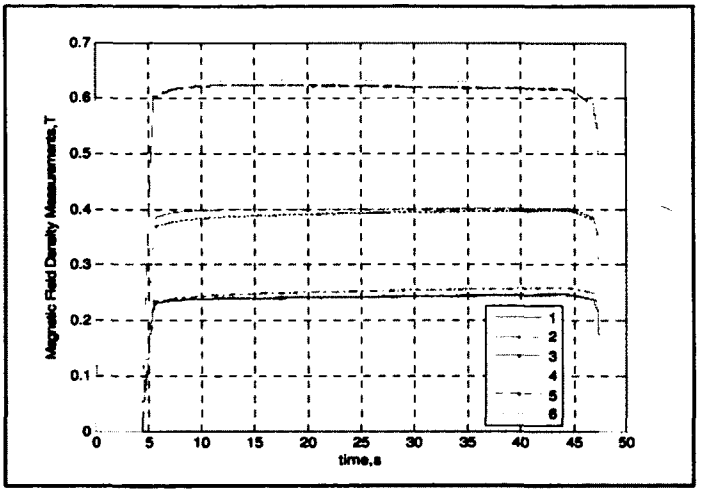

Figure 4.13. Magnetic Field Density Measurements for De-centralized control (Case 3-a)

Case 4-a

In this section, a comparison between the de-centralized and combined de-centralized-flux feedback controllers is made when the ODU Maglev system is exposed to a sinusoidal signal for an interval of 20 seconds that simulates the condition of air gap variation. In Figure 4.14-4.18, the simulation results are shown.

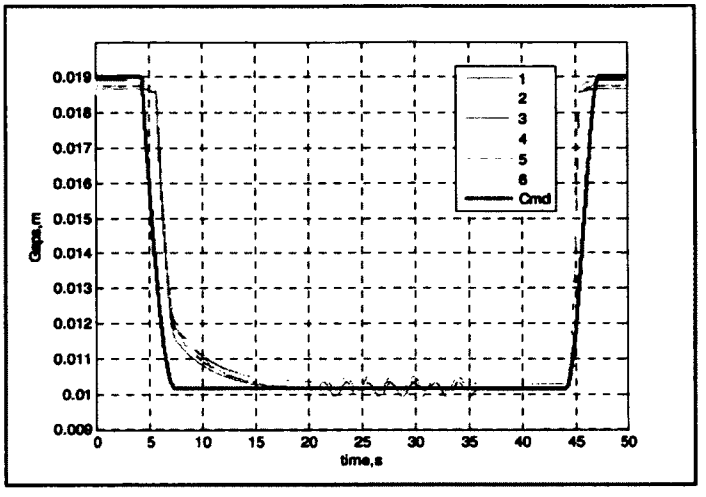

Figure 4.14. ODU Vehicle Air Gap Response with the De-centralized Control (Case 4-a-1)

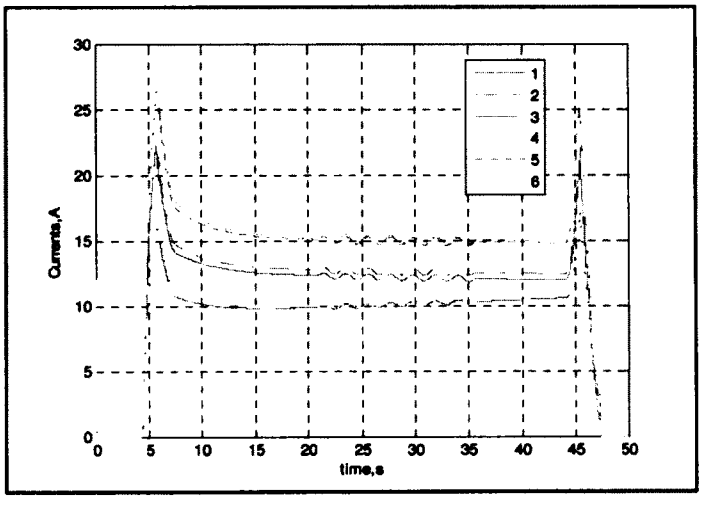

Figure 4.15. Currents in Electromagnets for De-centralized Control (Case 4-a-1)

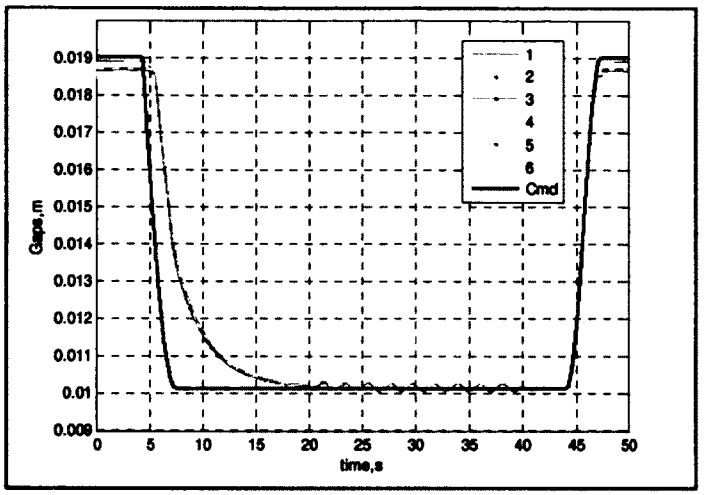

Figure 4.16. ODU Vehicle Air Gap Response with the De-centralized Control (Case 4-a-2)

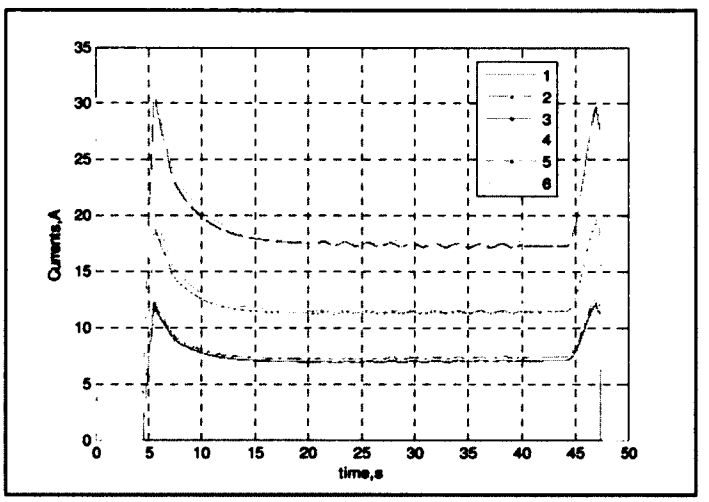

Figure 4.17. Currents in Electromagnets for De-centralized Control (Case 4-a-2)

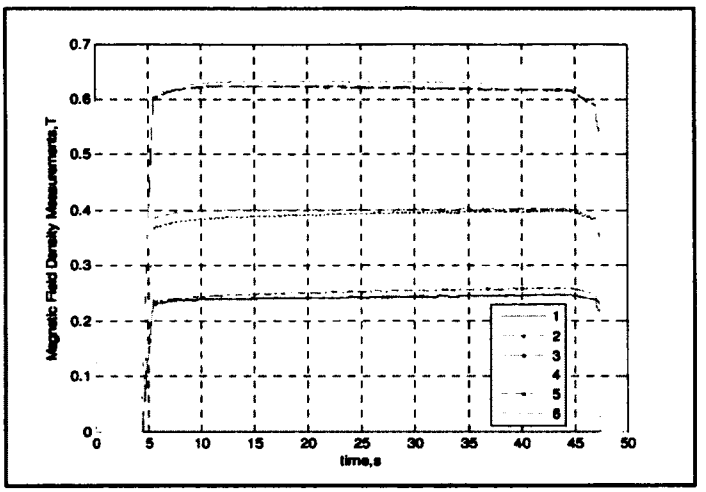

Figure 4.18. Magnetic Field Density Measurements for De-centralized control (Case 4-a-2)

Comparing the air gap responses in Figures 4.14, and 4.16, it is clear that the combined de-centralized-flux feedback controller has a smoother response and more resistance to air gap variations than the de-centralized one, or so it appears in the electromagnets currents as in Figures 4.15, and 4.17. The combined de-centralized flux feedback controller enhances the air gap response, resists the air gap variations and enhances the response with 45.45% than the de-centralized one.

Case 5

In this section, the simulation and experimental results for the ODU Maglev System when four magnets (1,2, 5, and 6) are used is shown. The experimental results are according to description introduced in section 4.6.3. Figures 4.19, and 4.20 are for simulation results while Figures 4.21, and 4.22 are for the experimental results.

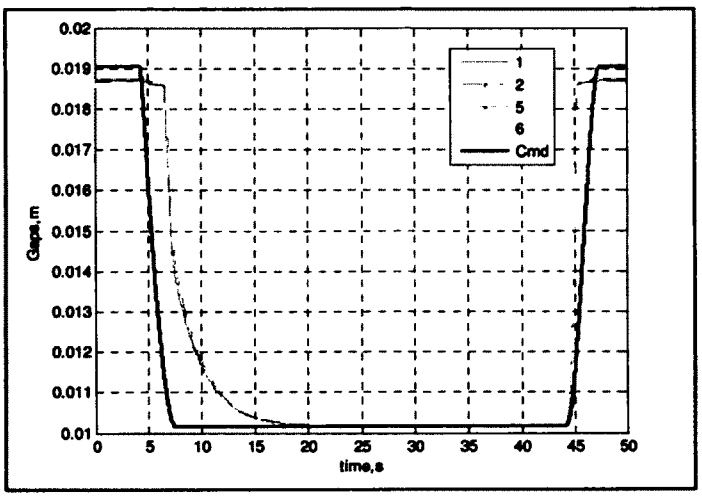

Figure 4.19. ODU Vehicle Air Gap Response with the De-centralized Control (Case 5)

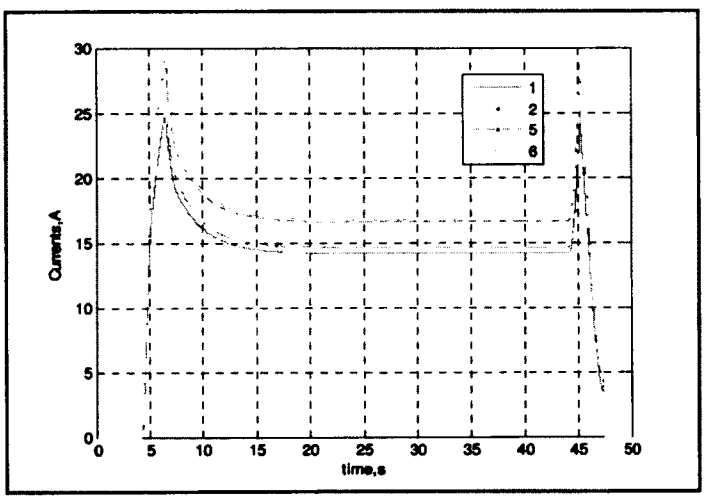

Figure 4.20. Currents in Electromagnets for De-centralized Control (Case 5)

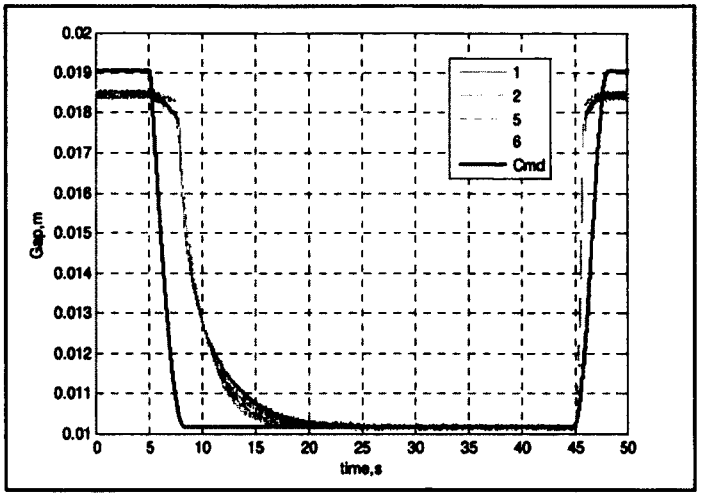

Figure 4.21. Actual ODU Vehicle Air Gap Response with the De-centralized Control (Case 5)

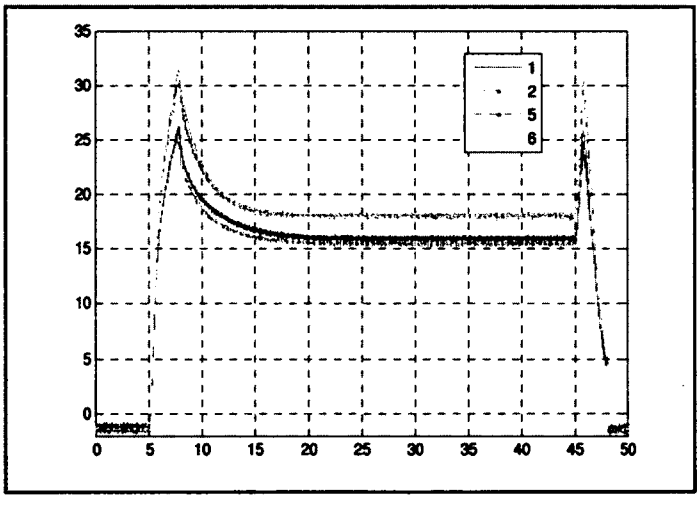

Figure 4.22. Actual Currents in Electromagnets for De-centralized Control (Case 5)

The experimental results in Figures 4.21, and 4.22 are pretty similar to the simulation results in Figure 4.19, and 4.20, which validate the de-centralized controller design for the Maglev system.

4.7 Centralized Controller Design

4.7.1 Centralized Controller Scheme

The centralized controller aims to control the bogie's degrees of freedom. The theory of centralized control enables one to control the system as a whole by measuring the local variables (air gaps and lateral displacements) and then converting them into the vehicle's modes using a transformation matrix. The vehicle's modes are controlled to provide the modal forces and torques. These modal forces and torques are transformed to local forces. The command currents are generated from the local forces and the measure gaps via a third transformation.

A significant note on the centralized control is that *n*-actuators must be used to control *n*-modes or *n*-variables of interest. This means that the number of magnets used as inputs decides the number of modes to be controlled. The block diagram of the centralized controller is shown in Figure 4.23.

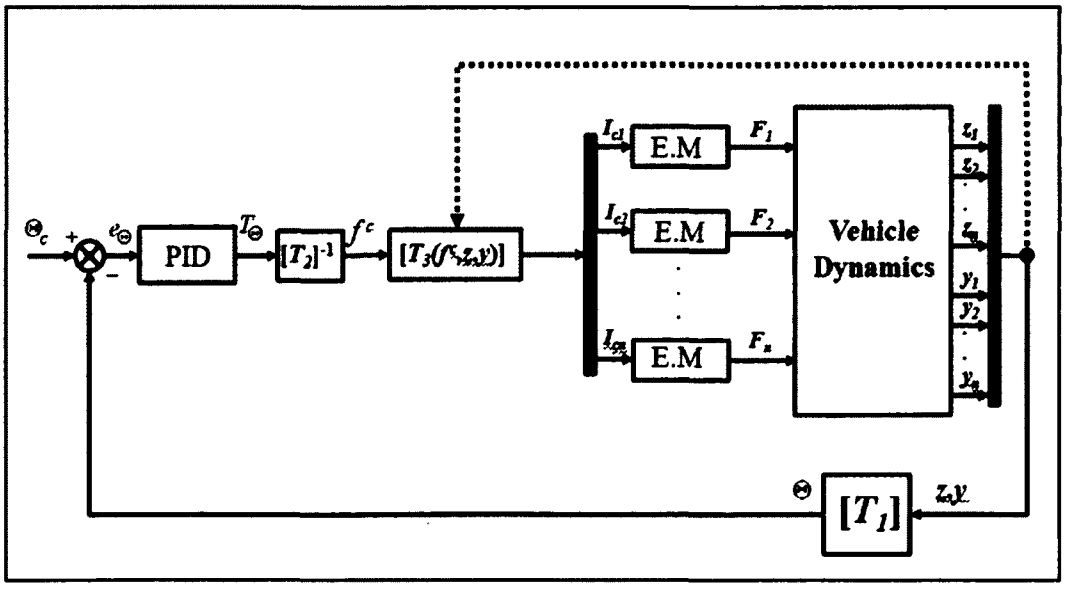

Figure 4.23. Centralized Controller

Using simple geometric relationships, the transformation T_1 is used to convert the local variables into the vehicle's modes and it depends on the geometry of vehicle:

$$\Theta=[T_1]Z \tag{4.26}$$

where,

Θ are the vehicle's rigid and flexible modes, and $Z=[z_1 \quad z_2 \quad . \quad . \quad z_n \quad y_1 \quad y_2 \quad . \quad . \quad y_n]^T$ are the measured airgaps and lateral displacements.

In Figure 4.24, a general sketch for the Maglev bogie on the guideway tracks with the six electromagnets distribution is shown. The three magnets 1, 3, and 5 are aligned with the magnets 2, 4, and 6 by a distance L_v around x-axis, while the two magnets 1 and 2 are aligned with the magnets 5 and 6 with a distance W_v. D_v is the diagonal distance between magnets 1 and 6.

The transformation that used to convert the local variables (electromagnet positions) into the bogie's modes is:

$$\underbrace{\begin{bmatrix} z \\ \phi \\ \theta \\ \zeta \\ y \\ \psi \end{bmatrix}}_{\Theta} = \underbrace{\begin{bmatrix} \frac{1}{4} & \frac{1}{4} & \frac{1}{4} & \frac{1}{4} & 0 & 0 \\ \frac{-2}{W_v} & \frac{2}{W_v} & \frac{-2}{W_v} & \frac{2}{W_v} & 0 & 0 \\ \frac{2}{L_v} & \frac{2}{L_v} & \frac{-2}{L_v} & \frac{-2}{L_v} & 0 & 0 \\ \frac{2}{W_v} & \frac{-2}{W_v} & \frac{-2}{W_v} & \frac{2}{W_v} & 0 & 0 \\ 0 & 0 & 0 & 0 & \frac{1}{2} & \frac{1}{2} \\ 0 & 0 & 0 & 0 & \frac{2}{D_v} & \frac{-2}{D_v} \end{bmatrix}}_{T_1} \begin{bmatrix} z_1 \\ z_2 \\ z_5 \\ z_6 \\ y_1 \\ y_5 \end{bmatrix} \tag{4.27}$$

where, z_1, z_2, z_5, and z_6 are the electromagnets vertical positions. y_1, and y_5 are the electromagnets lateral positions. z, y, φ, θ, and ψ are the bogie's rigid body modes heave, lateral, roll, pitch and yaw respectively. ξ, is the twist mode (one flexible mode

is considered for control). W_v, L_v and D_v are the vehicle's width, length and diagonal, respectively.

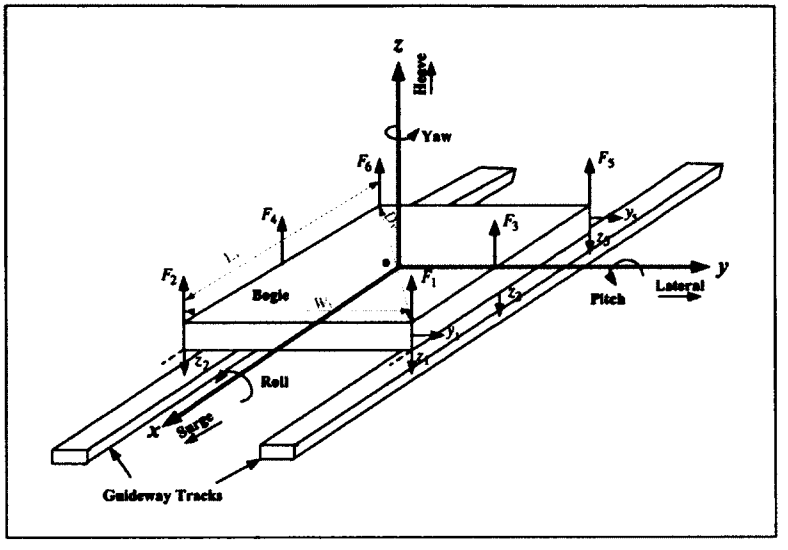

Figure 4.24. Sketch of Bogie on Tracks with Six Electromagnets Distribution

Since the inputs of the vehicle are the electromagnetic forces, the modal forces and torques (commands), which are the outputs of the centralized controller, need to be converted into the local magnetic forces via a transformation matrix T_2:

$$T_\Theta = [T_2] f^c \tag{4.28}$$

where,

T_Θ is the vehicle's model forces and torques, and

f^c is the vehicle's local forces.

Eq. (4.28) when re-written in detail:

$$\underbrace{\begin{bmatrix} F_z \\ T_\phi \\ T_\theta \\ T_\xi \\ F_y \\ T_\psi \end{bmatrix}}_{T_0} = \underbrace{\begin{bmatrix} 1 & 1 & 1 & 1 & 1 & 1 \\ W_v & -W_v & W_v & -W_v & W_v & -W_v \\ L_v & L_v & 0 & 0 & -L_v & -L_v \\ W_v & -W_v & 0 & 0 & -W_v & W_v \\ -1 & 1 & -2 & 2 & -1 & 1 \\ D_v & -D_v & 0 & 0 & -D_v & D_v \end{bmatrix}}_{T_2} \underbrace{\begin{bmatrix} f_1 \\ f_2 \\ f_3 \\ f_4 \\ f_5 \\ f_6 \end{bmatrix}}_{f} \tag{4.29}$$

Magnet staggering is important to achieve lateral and yaw control when combined magnet set is utilized. The staggering of magnets that is used for the Maglev test vehicle in order to achieve maximum lateral and yaw control is made by offsetting the magnets 1,2,5, and 6 to be in the direction outwards the rail by an offset distance Δ. An offset distance of 2Δ for magnets 3, and 4 in the direction towards the rail as shown in Figure 4.25. These staggering offsets form the last two rows in matrix T_2 by which lateral and yaw control of the vehicle is performed.

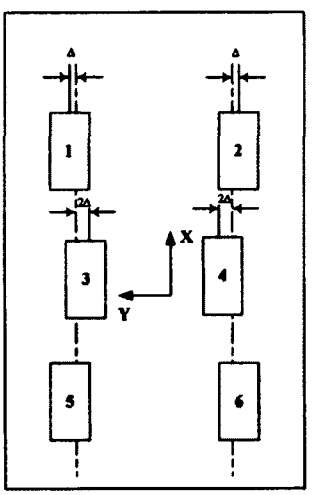

Figure 4.25. Test Bogie Magnets Distribution with Staggering

In order to verify that the suggested stagger distances will be suitable, the same method that is used in Chapter 2 is used. The intersection of $y/z = 2$ with the normalized

levitation force at 0.75, as in Figure 4.26, corresponds to a stagger distance of $\Delta \leq 0.75z$ for the ODU Maglev system according to the suggested magnets distributions in Figure 4.25. In Figure 4.26 the levitation and lateral forces vs lateral displacement for various stagger separations are shown.

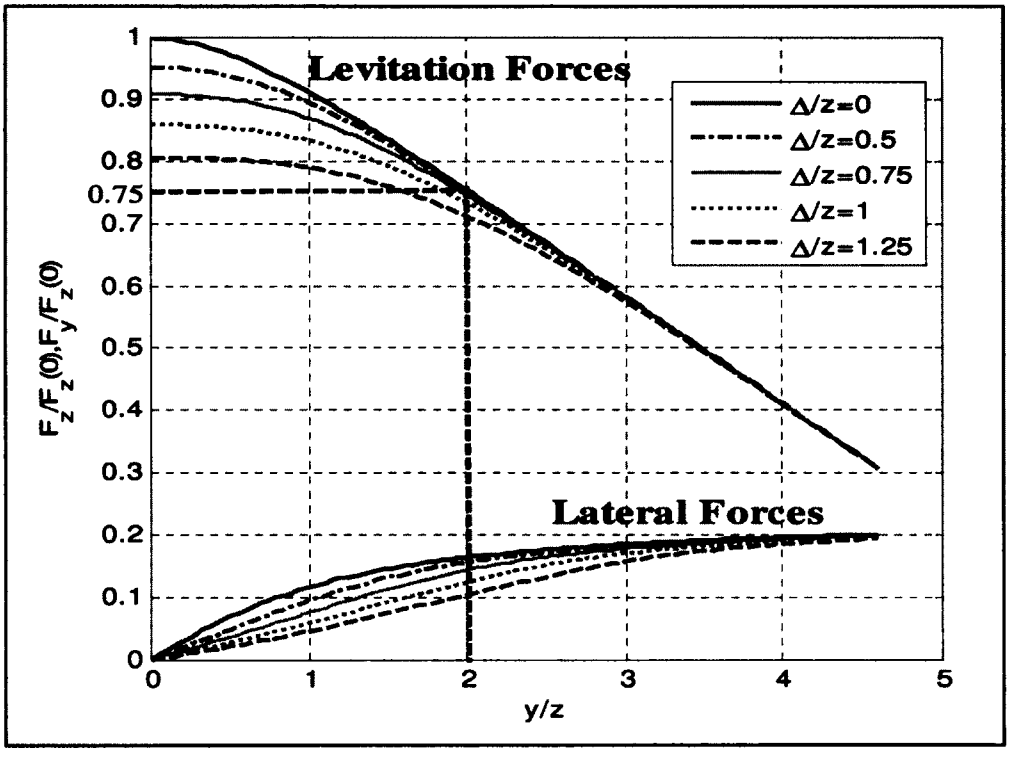

Figure 4.26. Levitation and Lateral Forces vs Lateral Displacement for Various Stagger Separations

To find out the command currents fed to the amplifiers, the force nonlinear expression with respect to z_i, y_j and I_{c_i} is linearized as:

$$I_{c_i} \cong \frac{f_i^c + k_{z_i} z_i + k_{y_j} y_j}{k_{i_i}} \quad \begin{matrix} ,i = 1,2,...,n \\ j = 1,2,...,m \end{matrix} \tag{4.30}$$

where constants k_{z_n}, k_{y_n} and k_{i_n} are

$$k_{z_n} = \left.\frac{\partial F_{z_n}}{\partial z_n}\right|_{z_o, y_o, I_o} = \frac{1}{2}\frac{\mu_o N^2 L_m W_m I_o^2}{z_o^3}\left(1+2\frac{z_o}{\pi W_m}\right) - \frac{\mu_o N^2 L_m I_o^2}{2\pi z_o^2} \tag{4.31}$$

$$k_{y_n} = \left.\frac{\partial F_{z_n}}{\partial y_n}\right|_{z_o, y_o, I_o} = \frac{1}{2}\frac{\mu_o N^2 L_m W_m I_o^2}{\pi z_o}\left(\frac{\tan^{-1}\left(\frac{y_o}{z_o}\right)}{z_o} + \frac{y_o}{\left(z_o^2 + y_o^2\right)}\right) \tag{4.32}$$

$$k_{i_n} = \left.\frac{\partial F_{z_n}}{\partial I_n}\right|_{z_o, y_o, I_o} = \frac{1}{2}\frac{\mu_o N^2 L_m W_m I_o}{z_o^2}\left(1+2\frac{z_o}{\pi W_m}\right) \tag{4.33}$$

where z_o, y_o and I_o are the nominal air gap, lateral displacement, and current of each magnet, respectively. The expression given in Eq.(4.30) can be written in a matrix form, as

$$I_c = T_3(f^c, z_i, y_j) \tag{4.34}$$

where $T_3 = \text{diag}(\lfloor I_{c_1} \quad I_{c_2} \quad \dots \quad I_{c_i} \rfloor)$.

The command model forces and torques are then

$$\begin{aligned} T^c &= K_{P_{n\Theta}} e_\Theta + K_{I_{n\Theta}} \int e_\Theta dt + K_{D_{n\Theta}} \dot{e}_\Theta \\ e_\Theta &= \Theta_c - \Theta \end{aligned} \tag{4.35}$$

where Θ_c is the mode's command, and the controller's proportional, integral and derivative gains are $K_{P_{n\Theta}}$, $K_{I_{n\Theta}}$, and $K_{D_{n\Theta}}$, respectively.

As already noted for the de-centralized controller in the previous section, any individual controller for the EMS Maglev system must have a positive feedback configuration in order to stabilize the system. It should be noted that the centralized controller will have some controllers that have positive feedback configurations while

others will have negative feedback configurations. This depends on the specific mode that is under control. The vehicle's modes that are originated from the air gap measurements alone will need a controller with a positive feedback configuration to be stabilized (e.g. heave, roll, pitch, and flexible twist mode), otherwise it will need a controller with a negative feedback configuration (e.g. lateral and yaw modes). This note is deduced from the nature of inherent stability of the heave mode unlike the lateral mode which is stable [11-12].

There are some operational challenges for the centralized control technique when the EMS Maglev system possesses some flexible modes. The PD centralized control is not suitable to control some flexible modes as in [2], although the 2-DOF EMS Maglev system that was used in this work did not include the electrodynamics part of the system model. It should be noted that these controllers are not widely used. This may be due to their restrictions to Maglev systems with flexible structures as every mode that is under control needs an accurate transformation (measurements to modes), which is difficult to achieve especially if the EMS Maglev system of significant flexibility.

4.7.2 Combined Centralized-Flux Feedback Control

In this section, the combined centralized-flux feedback is considered. Eq. (4.25) is used is used to calculate the magnetic field density as described in section 4.6.2.

In a similar manner, the linearization coefficients $k_{\Phi I_i}$, and $k_{\Phi z_i}$, i=1,2,...,6 that are necessary for the flux feedback gain k_{Φ_i} calculation are calculated from the steady state currents $I_{o_1}, I_{o_2}, ..., I_{o_6}$, and gaps $z_{o_1}, z_{o_2}, ..., z_{o_6}$. Having suitable flux feedback gains calculated as in Chapter 2, the inner loops for the flux measurements are closed as shown in Figure 4.18. The output of the flux controller block $I_{B_1}, I_{B_2}, ..., I_{B_6}$ is fedback in the

inner loops as shown in Figure 4.4 to make the system marginally stable. The command currents to the amplifiers $I_{c_1}, I_{c_2}, ..., I_{c_6}$ are resulted by subtracting the output of the flux controller from the output of the transformation matrix [T3], $I_{co_1}, I_{co_2}, ..., I_{co_6}$ as shown in Figure 4.28.

In order to have a complete controller design, the trial and error method is used to determine the gains of the PID controllers in the outer loops of the modes via MATLAB/SIMULINK simulation environment. It should be noted that the combined centralized flux feedback PID controllers' gains have different values than those used for the centralized control.

In Figure 4.27, the block diagram of the combined centralized flux feedback control is shown.

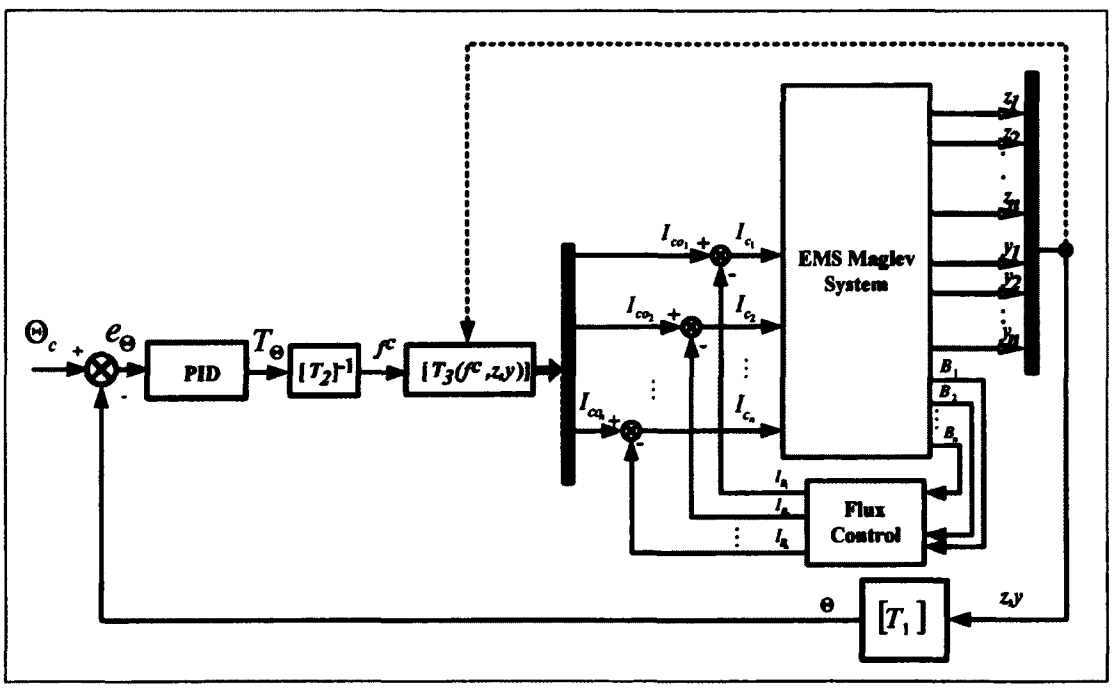

Figure 4.27. Combined Centralized-Flux Feedback Control

4.7.1 Simulation Results

Case 1-b

In this section, case 1-b in which normal levitation for the ODU EMS Maglev system with centralized control is studied. The simulation results for the ODU EMS Maglev vehicle with the centralized control for case 1-a are shown in Figures 4.28- 4.29.

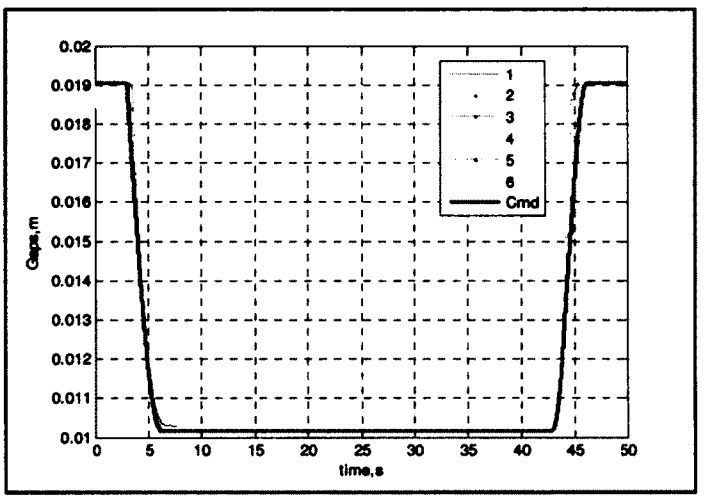

Figure 4.28. ODU Vehicle Air Gap Response with the Centralized Control (Case 1-b)

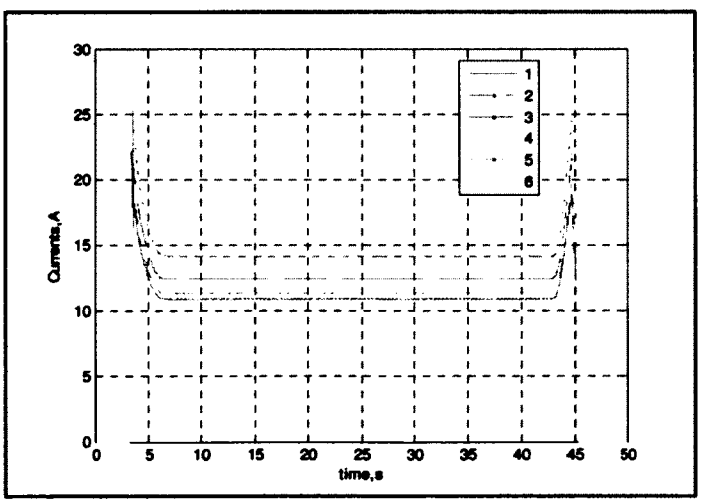

Figure 4.29. Currents in Electromagnets for Centralized Control (Case 1-b)

With the centralized control, the system is controlled as a whole, and the Maglev bogie mass distribution is not considered while controllers design as in case of the de-centralized controller.

The simulation results show that the PID centralized controller is capable of stabilizing the EMS Maglev system.

Case 2-b

In this section, case 2-b is considered similar to case 2-a. The simulation results for the ODU EMS Maglev vehicle with the centralized control is shown in Figures 4.30, and 4.31. The current in electromagnets are shown in Figure 4.32.

The airgap response affected more than in case of centralized control due to the interaction between heave and lateral dynamics and due to the calculation of the magnet forces as in $[T_3]$ based on the gap and lateral displacements measurements. The lateral motion response starts at 2mm and starts to decay faster than for the de-centralized control till the end of levitation at t=45s when it has a value of 0.022mm peak to peak, which represents approximately 99% damping of the maximum value of the lateral displacement [77]. The lateral motion decays to 0.05mm peak to peak at t=25s and due to that the airgap response appears smooth unlike the de-centralized control.

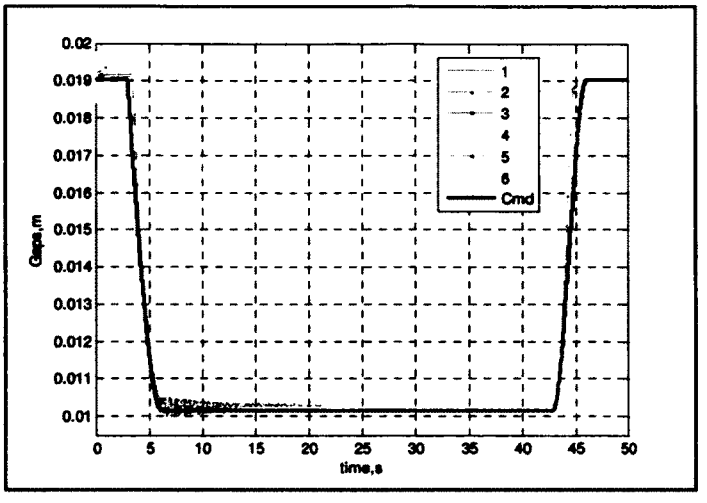

Figure 4.30. ODU Vehicle Air Gap Response with the Centralized Control (Case 2-b)

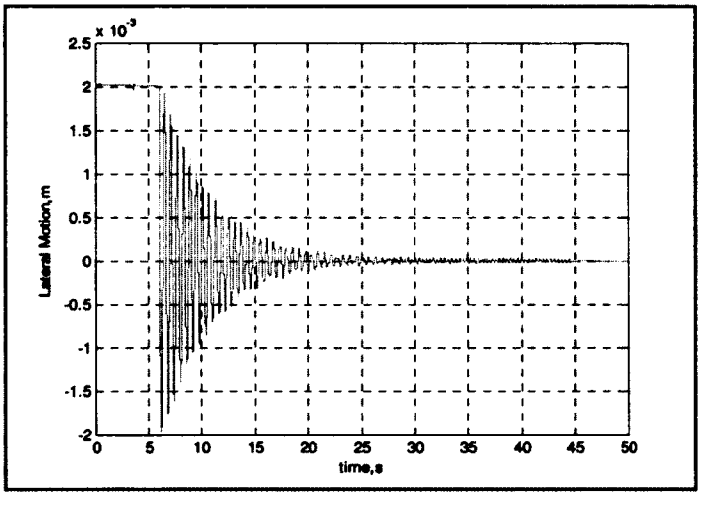

Figure 4.31. ODU Vehicle Lateral Motion Response with the Centralized Control

(Case 2-b)

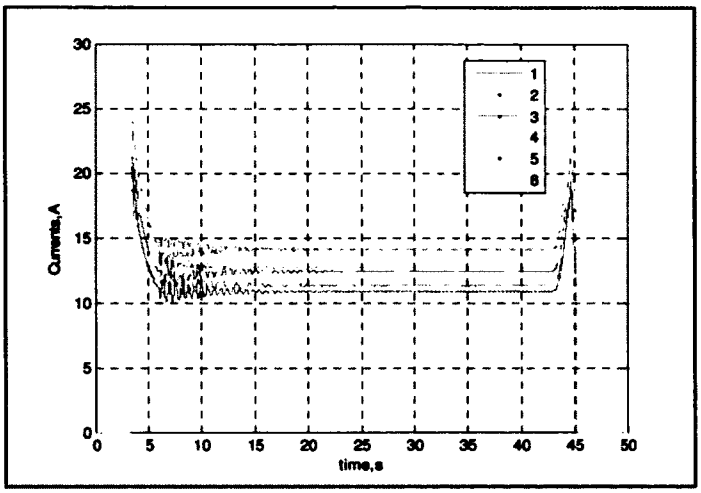

Figure 4.32. Currents in Electromagnets for Centralized Control (Case 2-b)

Case 3-b

In this section, case 3-b, in which normal levitation for the ODU EMS Maglev system with combined centralized flux feedback control, is studied. The simulation results for the ODU EMS Maglev vehicle with that controller are shown in Figures 4.33-4.35. For the simulation purposes and by the aid of MATLAB/SIMULINK, the magnetic field density measurements are generated as shown in Figure 4.35, with the order of 0.37-0.5T.

The simulation results show that the combined centralized-flux feedback controller is capable of stabilizing the EMS Maglev system. The results for the air gap measurements are similar to those of the combined de-centralized-flux feedback control.

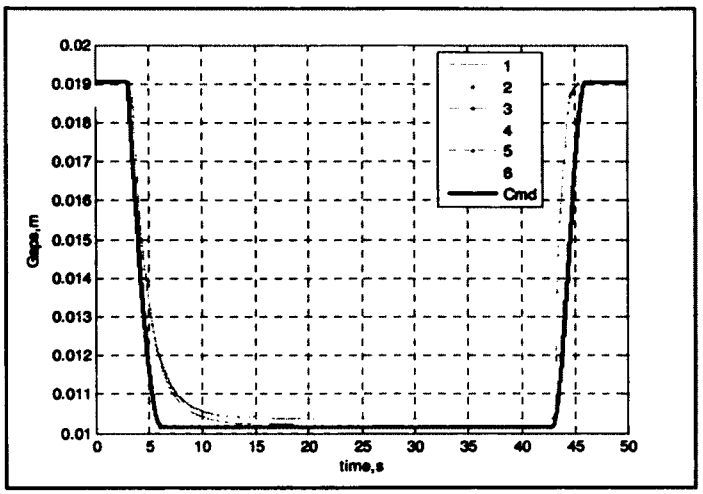

Figure 4.33. ODU Vehicle Air Gap Response with the Centralized Control (Case 3-b)

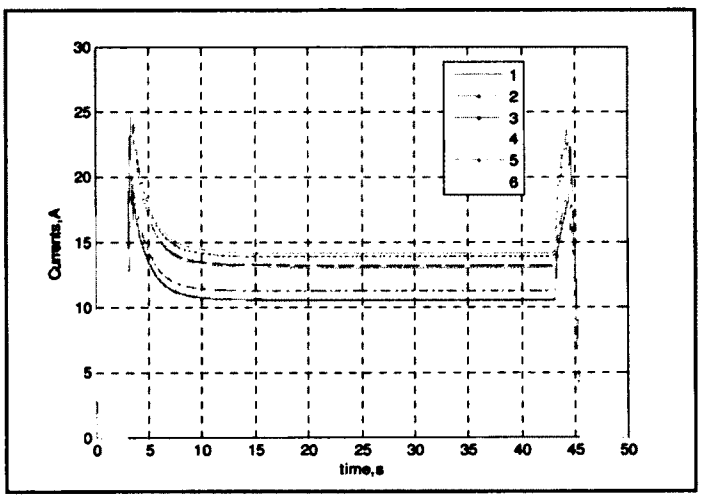

Figure 4.34. Currents in Electromagnets for Centralized Control (Case 3-b)

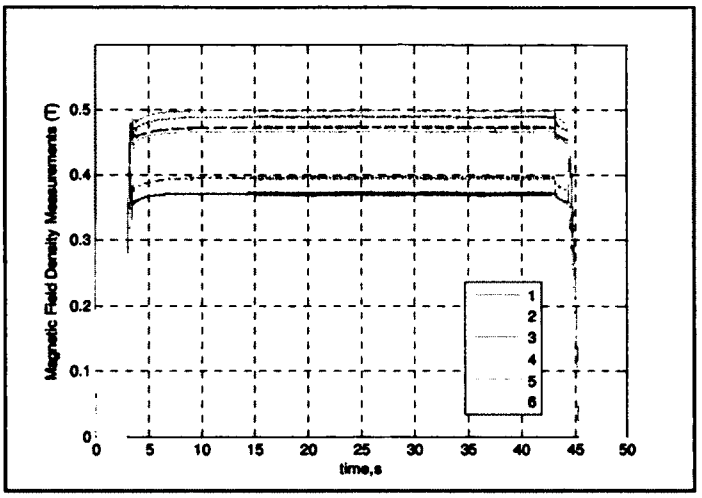

Figure 4.35. Magnetic Field Densities Measurements for Centralized Control (Case 3-b)

Case 4-b

In this section, a comparison between the centralized and combined centralized-flux feedback controllers is made using the same conditions as in case 4-a. The simulation results for the ODU EMS Maglev vehicle with those controllers are shown in Figures 4.36- 4.40.

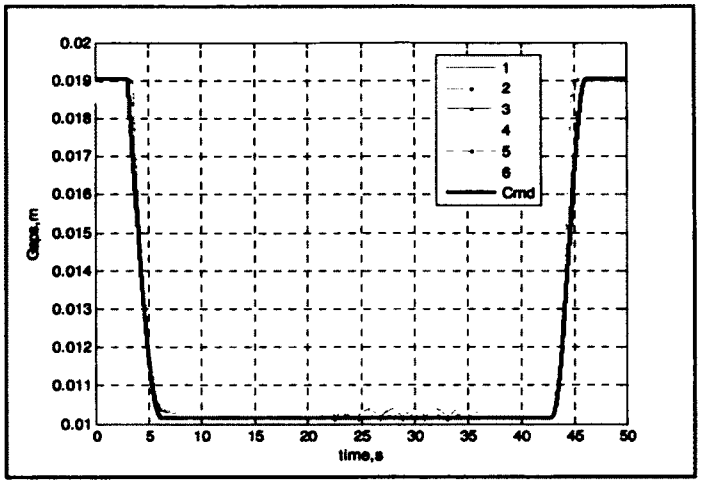

Figure 4.36. ODU Vehicle Air Gap Response with the Centralized Control

(Case 4-b-1)

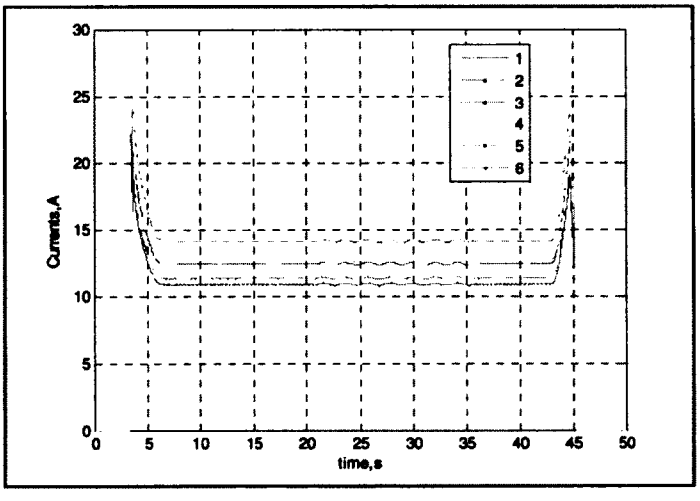

Figure 4.37. ODU Vehicle Air Gap Response with the Centralized Control

(Case 4-b-1)

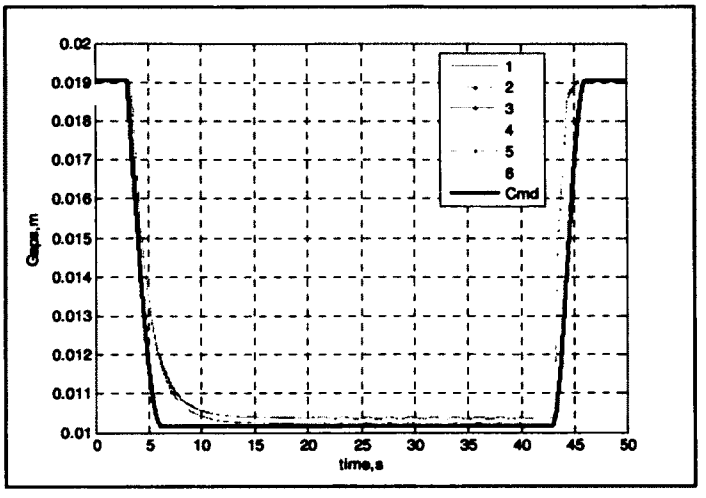

Figure 4.38. ODU Vehicle Air Gap Response with the Centralized Control (Case 4-b-2)

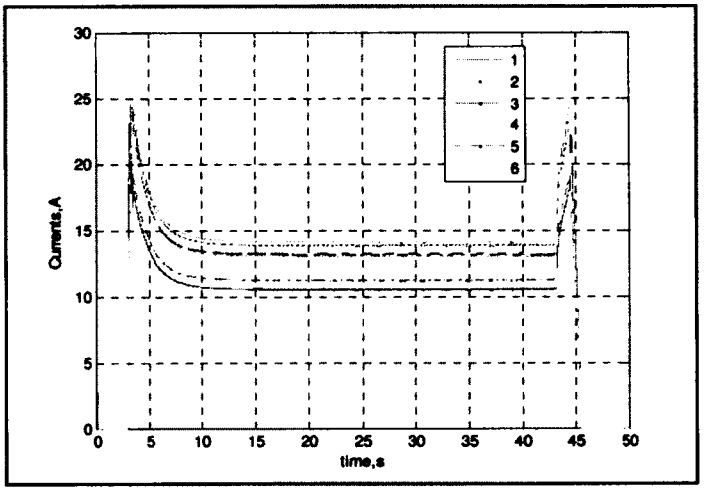

Figure 4.39. Currents in Electromagnets for Centralized Control (Case 4-b-2)

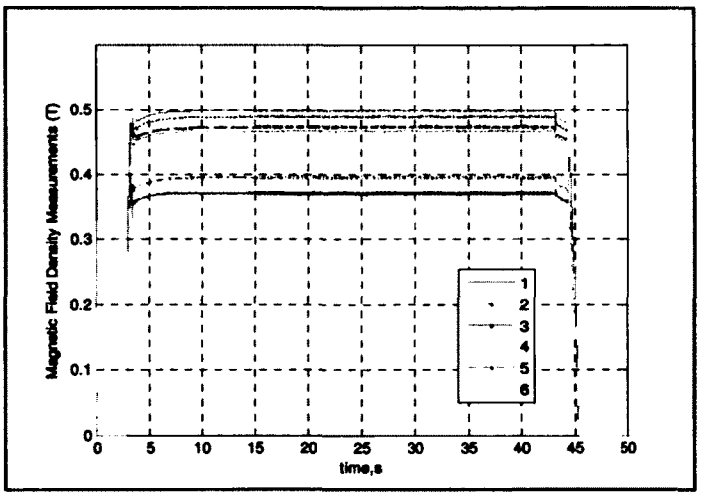

Figure 4.40. Magnetic Field Density Measurements for Centralized control

(Case 4-b-2)

Comparing the air gap responses in Figures 4.36, and 4.38, the combined centralized-flux feedback controller does smooth the air gap response and is more resistant to gap variation than the centralized one. The variations in the electromagnets currents for the combined controller in Figure 4.39 are less than of the centralized controller in Figure 4.37. The combined centralized- flux feedback controller enhances the air gap response, resists the air gap variations and enhances the response with 48.5% than the centralized one.

4.8 Conclusions

In this chapter, the complete model for the ODU EMS Maglev bogie is presented. The de-centralized and centralized controllers for that system are introduced. Also the combined de-centralized-flux feedback and centralized-flux feedback are presented.

The experimental results of the ODU Maglev system with the de-centralized control are presented. The same control scheme for Maglev simulation system is used but with

four magnets instead of six magnets. The experimental results match the simulation results, and hence validate the design of the de-centralized controller. In the centralized controller, and according to the suggested magnets distribution, the stagger distance is designed to be $\Delta=0.75z$ from forces' curves.

The simulation results for the ODU Maglev system have shown that the centralized controller is better than the de-centralized one when the system is exposed to a lateral disturbing force such as wind gusts and coincides with the results shown in Chapter 3 for the 2-DOF EMS Maglev system.

It can be easily proven that in the centralized control, the roll, and pitch modes can be controlled (if necessary) by defining a pre-set value for these modes unlike the de-centralized control that has only pre-set value for the air gaps only with a pre-set value of zero to roll and pitch modes.

Since the Maglev system is controlled as a whole in the centralized control, the bogie mass distribution is not considered in controller design as already done with the de-centralized controller.

It should be noted that in the centralized control it is not possible to receive an accurate transformation from local measurements to modes and the number of controlled modes should be less than or equal to the number of magnets used. This could be a problem if the Maglev system has a significant flexibility as it is not possible to control all modes.

Flux feedback control in combination with the de-centralized and centralized control for the system is described in detail. The PID controller gains used for the outer loops in the de-centralized-flux feedback and centralized-flux feedback controllers are

not the same as for the de-centralized and centralized controllers. The results for the air gap measurements of the combined de-centralized-flux feedback control are similar to those of the combined centralized-flux feedback control. This may be due to the nature of the marginal stable dynamics of the EMS Maglev system that results due to the feedback of the flux measurements.

Both de-centralized-flux feedback and centralized-flux feedback controllers do enhance the air gap response in comparison to the de-centralized and centralized controllers. The flux feedback control when used in combination with de-centralized or centralized controllers does improve the air gap response and more resistant and robust to the air gap variations.

The significance of flux feedback appears for the Maglev systems that suffer from the problem of frequent air gap variations. It should be noted that having flux sensors added to the Maglev system is cost wise, which means that we should not decide to use flux feedback control unless it is required.

CHAPTER 5

DE-CENTRALIZED AND CENTRALIZED CONTROL FOR ODU TEST BOGIE WHEN INTERACTING WITH GIRDER

5.1 Introduction

When a Maglev vehicle moves on a flexible girder, an inevitable interaction occurs. The significance of that was highlighted by issues discovered in 2002 when American Maglev Inc. tested its Maglev vehicle on the ODU flexible girder. The Maglev onboard controller failed to obtain stable levitation partially due to interaction with structural flexibility.

The objective of this chapter is to study the dynamic effect of a flexible girder on the Maglev system with the de-centralized or centralized controller schemes, and compare them for different vehicle's velocities based on the achieved performance and ride quality. In this chapter, the Maglev-girder interaction model is introduced. A generalized LPV model for the Maglev-girder system, 2-DOF Maglev-girder model, and pole-zero map with de-centralized and centralized control schemes are introduced. Then the MIMO root loci with the de-centralized and centralized control schemes are shown. A brief note on ride quality is also presented. The de-centralized and centralized control schemes with the ODU Maglev-girder system are introduced after applying controller gains' tuning using on LQR search algorithm. The simulation results are then discussed based on the performance and ride quality. Finally, the conclusions on the work presented in this chapter are presented. Figure 5.1 shows the ODU test vehicle (bogie), and Figure 5.2 shows the test vehicle being placed on the girder for testing.

Figure 5.1. ODU Maglev Test Vehicle (Bogie)

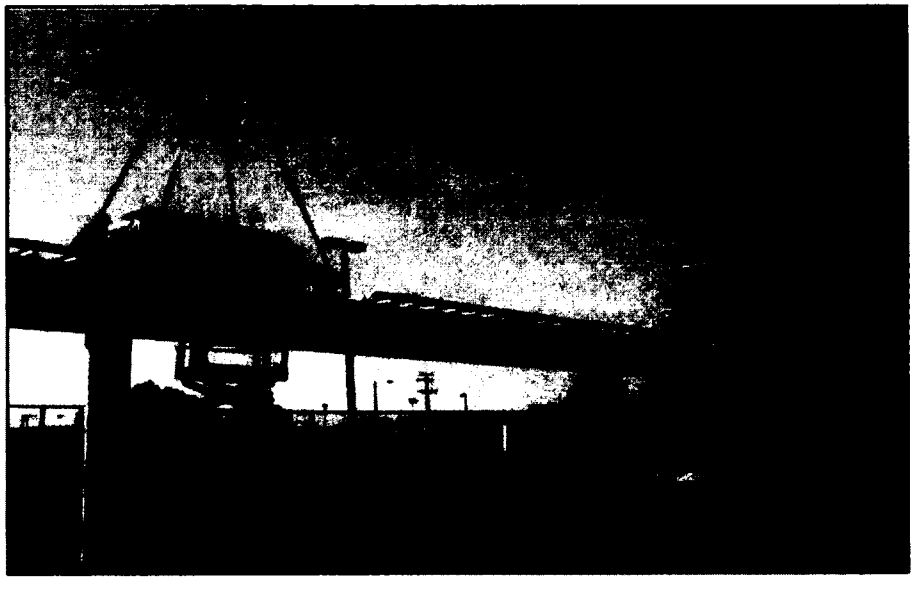

Figure 5.2. ODU Maglev System on Girder

5.2 Maglev-Girder Interaction

5.2.1 Introduction

In this section, the interaction between the vehicle and girder is considered in the presence of control action. The simulation scenario starts at an equilibrium condition while the required forces to lift the vehicle are equal to the weight of the vehicle. When

the vehicle moves over the girder, the generated vibration (w) of the girder changes the measured air gap (z) and the measured air gap rate (dz/dt). The controller then tries to keep the air gap (de-centralized) or the heave motion (centralized) at a constant value by changing the electromagnet current that consequently changes the forces acting over the girder.

The full girder span has two parts: the rigid part which is over a column of length L_s and the flexible part which is the girder span of L (beam length) as shown in Figure 5.3. When the vehicle moves on the rigid portion, the vibration of the girder is zero.

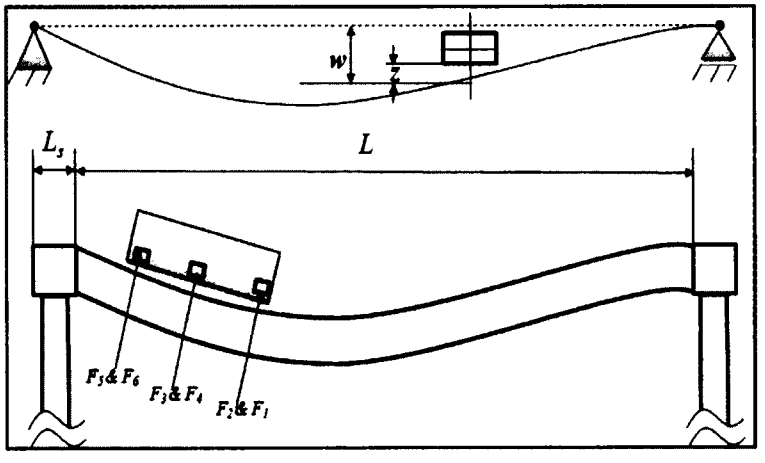

Figure 5.3. Schematic Diagram of Bogie-Girder Interaction

The ODU Maglev test vehicle has six magnets with magnetic levitation forces F_i, where i = 1,2,..., 6. These magnets are symmetrically distributed around the x and y axes of the bogie. As shown in Figure 5.3, the six moving forces F_i, i =1,2,...,6 have the same velocity v. Thus, these forces are separated from each other by a constant distance. In the simulation, the controller generates magnetic forces idealized as point forces F_i, i=1,2,...,6. These forces are uniformly distributed over the magnet length L_m. The model

of the guideway computes the girder displacement w_i, i = 1,2,..,6 at the middle of each magnet. Each girder displacement is then added to the equivalent gap sensor z_i, i = 1,2,..,6 and passed to the control feedback loop. The next Sections discuss the mathematical models of the girder, test vehicle, electrodynamics, and control schemes for simulation purposes.

5.2.2 Girder Model

The girder is a pre-stressed concrete structure. The individual girder spans are supported by concrete pillars at both ends. The track has a welded steel structure with aluminum cover plates as shown in Figure 5.4.

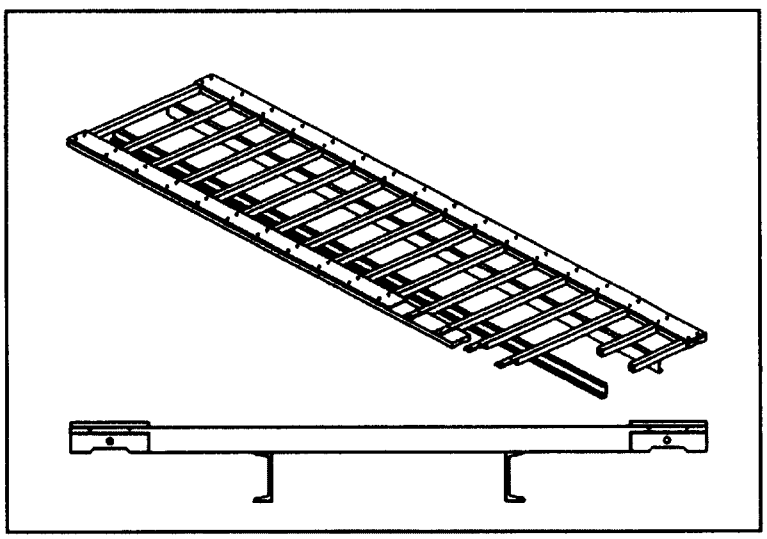

Figure 5.4. ODU Track

The girder spans have different lengths. However, for uniformity in the simulation, we choose to have constant length for all spans. The flexible part of the span is considered

as a simply supported beam with a length L and a flexural rigidity EI. The equation of motion is [13]:

$$EI\frac{\partial^4 w}{\partial x^4}+C\frac{\partial w}{\partial t}+m_b\frac{\partial^2 w}{\partial t^2}=\sum_{i-1}^{6}F_i(x,t) \tag{5.1}$$

Consider the boundary conditions as

$$\begin{aligned} w(0,t)&=0 \qquad & w(L,t)&=0 \\ \frac{\partial^2 w}{\partial x^2}(0,t)&=0 \qquad & \frac{\partial^2 w}{\partial x^2}(L,t)&=0 \end{aligned} \tag{5.2}$$

and the initial conditions as

$$w(x,0)=0 \qquad \frac{\partial w}{\partial t}(x,0)=0 \tag{5.3}$$

The eigenvalue problem assumes the solution is a product of separate functions of t and x as

$$w(x,t)=\sum_{n=1}^{\infty}q_n(t)\phi_n(x) \tag{5.4}$$

where q_n is the beam normal co-ordinate of the n^{th} mode. By substitution in Eq. (5.1), in the case of free motion ϕ_n is given by

$$\phi_n(x)=\sqrt{2}L\sin\left(\frac{n\pi x}{L}\right) \qquad n=1,2,... \tag{5.5}$$

The n^{th} mode q_n is the solution of the following equation:

$$\ddot{q}_n(t)+2\xi\omega_n\dot{q}_n(t)+\omega_n^2 q_n(t)=\frac{1}{m_b}\sum_{i=1}^{6}\Im_i(t) \tag{5.6}$$

where

$$\Im_i(t) = \int_0^L \phi_n(x) F_i(x,t) dx$$

$$\omega_n = \left(\frac{n^2\pi^2}{L^2}\right)\sqrt{\frac{EI}{m_b}} \text{ and } \varsigma_n = \frac{C}{2m_b\omega_n}$$

ω_n and ς_n are the natural frequency of the nth mode, and the corresponding modal damping ratio.

m_b : is the beam mass per unit length.

The first critical velocity is $v_c = \pi/L\sqrt{EI/m_b}$. When $v = v_c$, the crossing frequency (v_c/L) is equal to twice the natural frequency of the fundamental mode f_1. Using Eqs. (5.4-5.6), the beam displacement can be calculated at any location and at any time. Note, the model in Eqs. (5.4-5.6), considers that the force $F_i(x,t)$ is uniformly distributed over the magnet length L_m.

A finite element (FE) model of a girder span was built. Modal analysis was conducted to obtain the natural frequencies (eigenvalues) and mode shapes (eigenvectors). In addition to this, experimental testing was performed to validate these models. The frequency response (Bode) plots obtained through experimental testing, the FE model, and the analytical model (in Eqs. (5.4-5.6)) are compared in Figure 4.2 in Chapter 4. It can be seen that all three graphs match up well. This indicates that the girder model has been validated, and can be used for simulation case studies. Since the analytical model is computationally inexpensive, this model is used in the simulation.

5.2.3 Vehicle Dynamics

The input of the test vehicle's dynamic model is the electromagnetic forces F_i, i = 1,2,..., 6 and the output are the degrees of freedom that the mathematical model accounts for. The actual model in theory has infinite degrees of freedom, which can be

approximated by finite degrees of freedom, omitting higher frequency modes. In this section, the test vehicle is modeled to have six rigid body modes (surge, heave, lateral, roll, pitch and yaw) and a finite number of flexible modes. The test vehicle's translational equations of motion are

$$\begin{aligned} F_x &= m_s(\ddot{x} + \dot{h}\omega_y - \dot{y}\omega_z + g_x) \\ F_y &= m_s(\ddot{y} + \dot{x}\omega_z - \dot{h}\omega_x + g_y) \\ F_z &= m_s(\ddot{h} + \dot{y}\omega_x - \dot{x}\omega_y + g_z) \end{aligned} \tag{5.7}$$

In Eq. (5.7), m_s is the mass of the test vehicle and x, y, and h represent the three rigid body translation vectors (surge, lateral and heave). g_x, g_y, and g_z are the components of the gravitational acceleration on the x, y, and z axes respectively. ω_x, ω_y, and ω_z are the three rigid body rotational velocities, which are related to the Euler angle rates by

$$\begin{bmatrix} \omega_x \\ \omega_y \\ \omega_z \end{bmatrix} = \begin{bmatrix} 1 & 0 & -S_\theta \\ 0 & C_\varphi & S_\varphi C_\theta \\ 0 & -S_\theta & C_\varphi C_\theta \end{bmatrix} \begin{bmatrix} \dot{\phi} \\ \dot{\theta} \\ \dot{\psi} \end{bmatrix} \tag{5.8}$$

where ϕ is the roll angle, θ is the pitch angle, and ψ is the yaw angle.

The Euler angles are used herein to relate the gap displacements z_i, i =1, 2, ...,6 to the rigid body translational displacements (x, y, and h) in addition to relate the magnet force F_i, i=1,2,3,...,6 to the body forces (F_x, F_y, and F_z) and moments (M_x, M_y, and M_z). The rotational equations of motion of the bogie are

$$\vec{M} = [I]\frac{d\vec{\omega}}{dt} + \vec{\omega} \times ([I]\vec{\omega}) \tag{5.9}$$

where,

$$\vec{M}=\begin{bmatrix} M_x \\ M_y \\ M_z \end{bmatrix}, \vec{\omega}=\begin{bmatrix} \omega_x \\ \omega_y \\ \omega_z \end{bmatrix}, \quad [I]=\begin{bmatrix} I_{xx} & -I_{xy} & -I_{xz} \\ -I_{xy} & I_{yy} & -I_{yz} \\ -I_{xz} & -I_{yz} & I_{zz} \end{bmatrix}$$

In Eq.(5.9), [I] is the inertia matrix.

The vehicle flexible modes are modeled in a similar manner as in Chapter 4:

$$\ddot{q}_{v_j} + D_t \dot{q}_{v_j} + \Lambda q_{v\,j} = \Psi^T F \quad , j = 1,...k \tag{5.10}$$

where q_v represents the modal co-ordinates, or modal vectors. The matrix Ψ is

$$\Psi^T = \begin{bmatrix} \phi_{z_1}^T & \phi_{z_2}^T & \cdots & \phi_{z_i}^T \end{bmatrix} \tag{5.11}$$

where $\phi_{z_i}^T$ are the z-columns of the mode shape matrix corresponding to the i^{th} actuator.

5.2.4 Electrodynamics

The idea behind the levitation system is the instantaneous generation of an attractive force between an electromagnetic and ferromagnetic plate. The inclusion of the levitation force and its dynamics is important to simulate the real Maglev-girder interaction. In references [21-22], [24-31], there is no explicit definition of the Maglev levitation forces in terms of the electromagnet's electrodynamics. The levitation system model is found in reference [46] and it is almost the same as presented in Chapter 4. For the electromagnet shown in Figure 2.3, the final current loop is:

$$\frac{dI}{dt} = \frac{K_A}{L_m(z)}(I_c - I) - \frac{RI}{L_m(z)} + \frac{I}{z}\frac{dz}{dt} \tag{5.12}$$

The inner feedback loop in Eq. (5.12) provides an accurate current hold but it does not guarantee to provide a gap hold.

5.2.5 Maglev-Girder Interaction Parameter Varying Model

The Maglev-girder interaction parameter varying model is derived from the nonlinear equations of the vehicle and girder sub-models. These sub-models are connected to insure the dynamical interaction between the vehicle and girder.

5.2.5.1 A Generalized Maglev-Girder LPV Model

In this section, the LPV model of the Maglev-girder interaction system is presented. This model is decomposed into the sub-model of the test-vehicle in Eqs. (5.7-5.10) with the electrodynamics sub-model in Eq.(5.12), and the girder's vibration sub-model in Eqs. (5.4-5.6). The nonlinear state space model of the EMS Maglev vehicle is

$$\begin{aligned} \dot{x} &= f(x,u,t) = \begin{bmatrix} f_1 & \cdots & f_{12} & f_{j+12} & \cdots & f_{k+12} & f_{k+i+12} & \cdots & f_{k+n+12} \end{bmatrix}^T \\ x &= \begin{bmatrix} x_\Theta & x_{q_v} & x_I \end{bmatrix}^T \end{aligned} \tag{5.13}$$

where

$$x_\Theta = \begin{bmatrix} X & Y & h & \phi & \theta & \psi & \dot{X} & \dot{Y} & \dot{h} & \dot{\phi} & \dot{\psi} & \dot{\theta} \end{bmatrix}^T$$

$$x_{q_v} = \begin{bmatrix} q_{v_1} & q_{v_1} & \cdots & q_{v_j} & \dot{q}_{v_1} & \dot{q}_{v_2} & \cdots & \dot{q}_{v_j} \end{bmatrix}$$

$$x_I = \begin{bmatrix} I_1 & I_2 & \cdots & I_i \end{bmatrix}^T$$

The vector x_Θ represents the states of the rigid test vehicle modes, the vector x_{q_v} represents the test vehicle flexible modes, and the vector x_I represents the states of the electrodynamics. The input to this sub-model is the command currents I_{c_i} and the outputs are the gaps z_i and magnetic levitation forces F_{z_i}.

The nonlinear expressions from f_1 to f_{12} can be found from Eqs. (5.7) and (5.9). These expressions are given in [78]. The linearized expression of the electrodynamics (Eq. (5.12)) is

$$f_{i+j+12} = -\alpha I_i + \beta I_{c_i} \tag{5.14}$$

where $\alpha = \frac{K_A + R}{L_m}$ and $\beta = \frac{K_A}{L_m}$ where $i = \{1,2,\ldots,n\}$.

The linearized levitation forces expression is

$$F_{z_i} \cong -k_z z_i + k_i I_i \tag{5.15}$$

where k_z, and k_i are the air gap and current linearization coefficients as described in Chapter 2.

The girder's vibration sub-model is

$$\dot{x} = f(x,u,t) = \begin{bmatrix} \overline{f_1} & \ldots & \overline{f_m} \end{bmatrix}^T \qquad , x = \begin{bmatrix} x_q \end{bmatrix}^T \tag{5.16}$$

where $x_q = \begin{bmatrix} q_1 & \dot{q}_1 & \cdots & q_m & \dot{q}_m \end{bmatrix}^T$, and the vector x_q represents the states of the girder's vibration. The girder vibration equations are

$$\begin{aligned} &\bar{f}_l = \dot{q}_l \qquad , l = \{1,2,\cdots,m\} \\ &\bar{f}_{l+1} = -\omega_l^2 q_l - 2\xi_l \omega_l q_l + \frac{\sqrt{2}\left(F_{z_1} + F_{z_2}\right)}{m_b L_b^2} \sin\left(\frac{\pi x_1}{L_b}\right) + \frac{\sqrt{2}\left(F_{z_2} + F_{z_4}\right)}{m_b L_b^2} \sin\left(\frac{\pi x_2}{L_b}\right) + \\ &\ldots\ldots\ldots + \frac{\sqrt{2}\left(F_{z_{i-1}} + F_{z_i}\right)}{m_b L_b^2} \sin\left(\frac{\pi x_i}{L_b}\right) \end{aligned} \tag{5.17}$$

where x_1, x_2, and x_i are the locations of magnetic levitation forces on girder.

The ODU Maglev vehicle employs six electromagnets; hence, three locations of the magnetic levitation forces are considered. These locations can be combined in one variable, which is the location of the test-vehicle's center of gravity ($x_2 = x_{cg}$, $x_1 = x_{cg} - L_v/2$, and $x_3 = x_{cg} + L_v/2$). The value x_{cg} changes periodically with time from 0 to L with a velocity v.

The inputs to the girder's vibration sub-model are the magnetic levitation forces F_{z_i} and the locations of the magnetic levitation forces on girder x_i, and the outputs are the girder vibrations w_i that correspond to theses forces and their locations.

The modeling of the vehicle-girder system involves the connection of these sub-models as shown in Figure 5.5 to have the overall system input as the command currents I_{c_i} and the outputs are the measured gaps z_{m_i}.

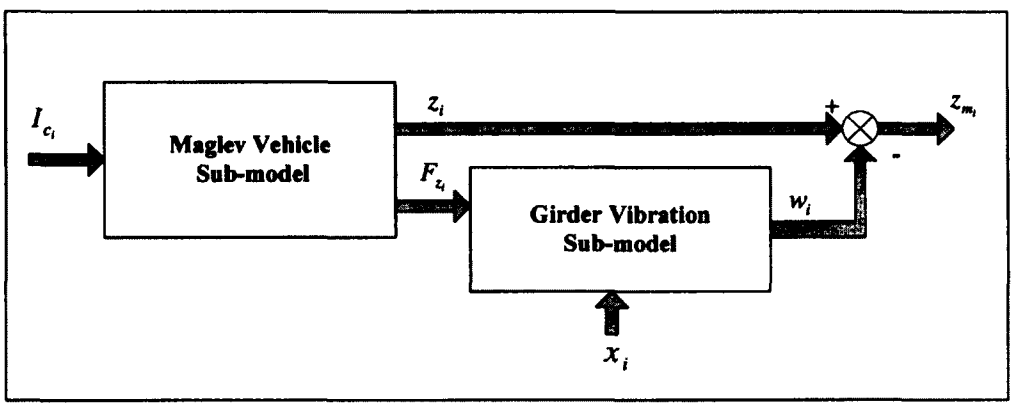

Figure 5.5. Vehicle-Girder Interaction Generalized Model

In order to find the linearized state space matrices, some manipulations must be considered in which the interconnection between sub-models should be carefully handled [79]. If x_{cg} is considered as the varying parameter of the system, the equivalent LPV of the system in Eqs. (5.13-14) and (5.17) is

$$\begin{aligned} \dot{x} &= Ax + B(p)x \quad , \quad p = x_{cg}(t) \\ y &= C(p)x \end{aligned} \tag{5.18}$$

where

$$A=\begin{bmatrix} A_1 & 0_{n_2 \times n_2} \\ B_2 C_{22} & A_2 \end{bmatrix},\ B=\begin{bmatrix} B_1 \\ 0_{n_2 \times m} \end{bmatrix},\ C(p)=\begin{bmatrix} C_{11} & -C_{22} \end{bmatrix}$$

A_1, B_1, C_1, are the state space representation of the Maglev vehicle sub-model,

$C_1 = \begin{bmatrix} C_{11} \\ C_{22} \end{bmatrix}$, where C_{11} is the output matrix of the first set of Maglev vehicle sub-model outputs (gaps), and C_{22} is the output matrix of the second set of Maglev vehicle sub-model outputs (magnetic levitation forces).

A_2, B_2, C_2, are the state space representation of the girder vibration sub-model,

$n_s = n_1 + n_2$ is the number of the overall system states , n_1 is the Maglev vehicle sub-model number of states, n_2 is the girder vibration sub-model number of states and m is the number of the overall system inputs.

The system in Eq. (5.18) has a large number of states because of the girder flexibility in addition to the electrodynamics and rigid body modes of the test vehicle. The large number of states makes it difficult to draw any conclusion from the problem. In order to simplify the analysis of the influence of the variation on the system dynamics, a simplified 2-DOF model is considered next. In the simulation section, the analysis will be numerically applied to the overall system.

5.2.5.2 A 2-DOF Maglev-Girder Model

A 2-DOF rigid Maglev-girder system is used to understand the variation of the system dynamics with change in the test vehicle's position on the girder. Figure 5.6 shows 2-DOF Maglev Vehicle on a Flexible Girder. This simplified model accounts for the heave h and pitch θ modes of the rigid body in addition to the first vibration mode of

the girder q_1. The vehicle is assumed to be levitated by two point forces F_1 and F_2 separated from each other by a distance L_v and moving with a velocity (v).

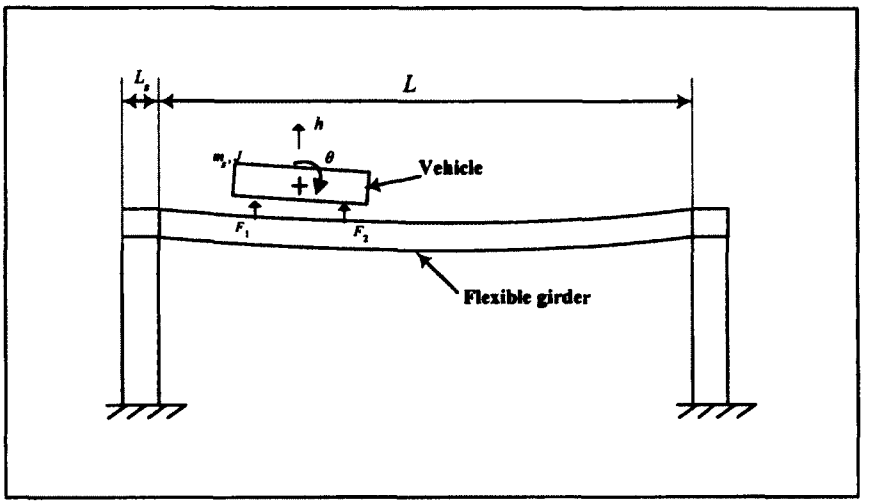

Figure 5.6. 2-DOF Maglev Vehicle on a Flexible Girder

The relation between the measured gaps z_1 and z_2 and the test-vehicle heave h and pitch θ is

$$z_1 = h - \frac{L_v}{2}\sin(\theta)$$
$$z_2 = h + \frac{L_v}{2}\sin(\theta) \tag{5.19}$$

The equivalent girder's vibrations at z_1 and z_2 are w_1, and w_2 respectively. Using Eigen theory, these vibrations are

$$w_i = \sqrt{2}\, q_1 L_b \sin\left(\frac{\pi x_i}{L_b}\right), i = 1,2 \tag{5.20}$$

where q is the normal co-ordinate of the girder's first mode given in Eq. (5.3). The nonlinear state space model of this simplified system is

Maglev Vehicle Equations:

$$\begin{aligned} f_1 &= \dot{h} & f_2 &= -(F_1+F_2)/m_v \\ f_3 &= \dot{\theta} & f_4 &= (-F_1+F_2)L_v/2J_v \\ f_5 &= -\alpha I_1 + \beta I_{c1} & f_6 &= -\alpha I_2 + \beta I_{c2} \end{aligned} \tag{5.21}$$

Girder Vibration Equations:

$$\begin{aligned} f_7 &= \dot{q}_1 \\ f_8 &= -\omega_1^2 q_1 - 2\zeta\omega_1\dot{q}_1 + \frac{\sqrt{2}F_1}{m_b L_b^2}\sin\left(\frac{\pi x_1}{L_b}\right) + \frac{\sqrt{2}F_2}{m_b L_b^2}\sin\left(\frac{\pi x_2}{L_b}\right) \end{aligned} \tag{5.22}$$

The state vector is

$$x^T = \begin{bmatrix} h & \dot{h} & \theta & \dot{\theta} & i_1 & i_2 & q_1 & \dot{q}_1 \end{bmatrix}^T$$

The LPV model in Eqs. (5.21) and (5.22) is

$$\begin{aligned} \dot{x}(t) &= Ax(t) + Bu(t) \\ y(t) &= C(p)x(t) \end{aligned} \tag{5.23}$$

where

$$A = \begin{bmatrix} 0 & 1 & 0 & 0 & 0 & 0 & 0 & 0 \\ \frac{2k_z}{m_v} & 0 & 0 & 0 & \frac{-k_i}{m_v} & \frac{-k_i}{m_v} & 0 & 0 \\ 0 & 0 & 0 & 1 & 0 & 0 & 0 & 0 \\ 0 & 0 & \frac{2k_z L_v^2}{2J_v} & 0 & \frac{k_i L_v}{2J_v} & \frac{-k_i L_v}{2J_v} & 0 & 0 \\ 0 & 0 & 0 & 0 & -\alpha & 0 & 0 & 0 \\ 0 & 0 & 0 & 0 & 0 & -\alpha & 0 & 0 \\ 0 & 0 & 0 & 0 & 0 & 0 & 0 & 1 \\ \frac{-\sqrt{2}k_z}{m_b L_b^2}s^+ & 0 & \frac{\sqrt{2}k_z L_v}{2m_b L_b^2}s^- & 0 & \frac{\sqrt{2}k_i}{m_b L_b^2}s_1 & \frac{\sqrt{2}k_i}{m_b L_b^2}s_2 & -\omega_1^2 & -2\zeta\omega_1 \end{bmatrix}$$

$$B = \begin{bmatrix} 0 & 0 & 0 & 0 & \beta & 0 & 0 & 0 \\ 0 & 0 & 0 & 0 & 0 & \beta & 0 & 0 \end{bmatrix}^T \qquad C = \begin{bmatrix} 1 & 0 & -L_v/2 & 0 & 0 & 0 & -\sqrt{2}L_b s_1 & 0 \\ 1 & 0 & L_v/2 & 0 & 0 & 0 & -\sqrt{2}L_b s_2 & 0 \end{bmatrix} \tag{5.24}$$

and

$$s_1 = \sin\left(\frac{\pi x_1}{L_b}\right) \quad s_2 = \sin\left(\frac{\pi x_2}{L_b}\right)$$
$$s^+ = s_1 + s_2 \quad s^- = s_1 - s_2$$

In the case that $x_1 = x_2 = 0$, the system characteristic equation can be easily found as:

$$(s+\alpha)^2(s^2-\omega_r^2)(s^2-\omega_t^2)(s^2+\omega_1^2)=0 \tag{5.25}$$

where, $\omega_t = \sqrt{\frac{2k_z}{m_v}}$ and $\omega_r = \frac{L_v}{2}\sqrt{\frac{2k_z}{J_v}}$ are the natural frequencies of the translation and rotation motions. Although the last row of the A matrix involves s^+, s^-, s_1, and s_2, they do not affect the system dynamics.

5.3 Maglev-Girder Interaction System Pole-zero Map with Control Schemes

5.3.1 Pole-zero Map of De-centralized Control with a 2-DOF Maglev-Girder System

The de-centralized open loop scheme has inputs as command currents to the electromagnet's amplifiers, and outputs as measured gaps as shown in Figure 5.7. The pole-zero map of the de-centralized open loop scheme is considered at positions $x = 0$ to $x = L/2$.

As shown in Figure 5.7, when $x = 0$, the poles can be easily interpreted as in Eq.(5.22), two stable poles of the electrodynamics far on the left, two stable poles of translational and rotational motion, two unstable poles of translational and rotational motion, two poles on the imaginary axis for the girder vibration and two transmission zeros that are coinciding with the girder vibration poles. This means that when $x = 0$, there is no interaction between vehicle and girder. When the vehicle travels on the girder having positions (x_1, x_2), the transmission zeros start to move in the direction to the origin on the imaginary axis, other poles stay at the same location (see Figure 5.7).

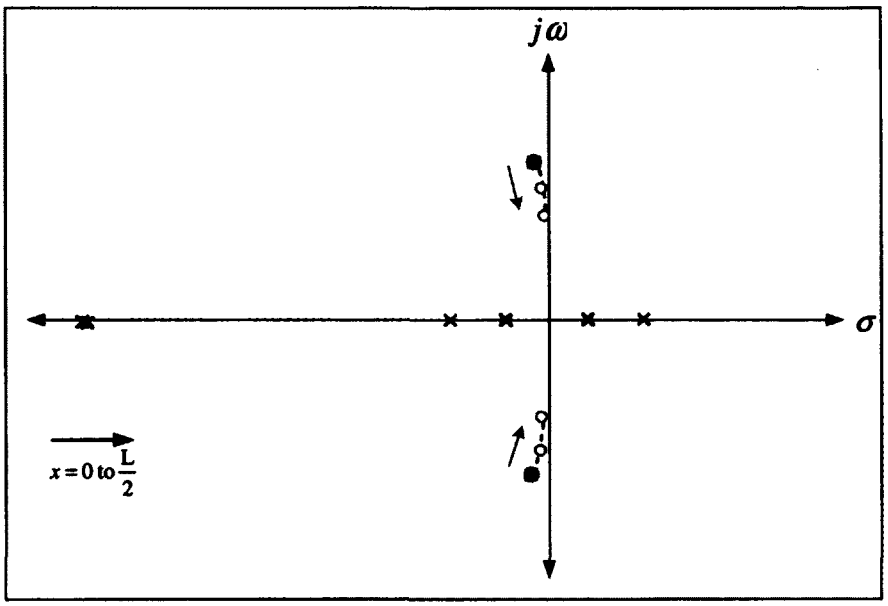

Figure 5.7. A Generic Pole-Zero Map of De-centralized Scheme

5.3.2 Pole-zero Map of Centralized Control with a 2-DOF Maglev-Girder System

The state space system on Eq. (5.23) is for the de-centralized scheme, and the state space system for the centralized scheme (A_{cen}, B_{cen}, C_{cen}, D) is formed after including the transformation matrices as follows:

$$A_{cen} = A + BHC \tag{5.26}$$

where

$$H = \frac{1}{k_i}\begin{bmatrix} k_z & 0 \\ 0 & k_z \end{bmatrix}$$

$$B_{cen} = B[T_2],\ [T_2] = \begin{bmatrix} 1/2 & 1/2 \\ 1 & -1 \end{bmatrix} \qquad C_{cen} = [T_1]C,\ [T_1] = \begin{bmatrix} 1/2 & 1/2 \\ -1/L_v & 1/L_v \end{bmatrix}$$

$$C_{cen} = \begin{bmatrix} 1 & 0 & 0 & 0 & 0 & 0 & \frac{-\sqrt{2}L_b}{2}s^+ & 0 \\ 0 & 0 & 1 & 0 & 0 & 0 & \frac{\sqrt{2}L_b}{L_v}s^- & 0 \end{bmatrix}$$

Figure 5.8 shows the generic open loop pole-zero map of the centralized controller. There is some difference between the centralized and decentralized pole zero maps. The transformation matrices used to convert from gaps to modes and from modal forces and torques to magnet forces are changing the open loop dynamics, as shown in Eq. (5.26). So the unstable heave and pitch poles are relatively distant from each other than the stable ones as shown in figure 5.8. One of the electrodynamics poles (far on the left) is moving to left. The girder poles moves up a little bit as $x = L/2$. The transmission zeros on the $j\omega$ move down as $x = L/2$.

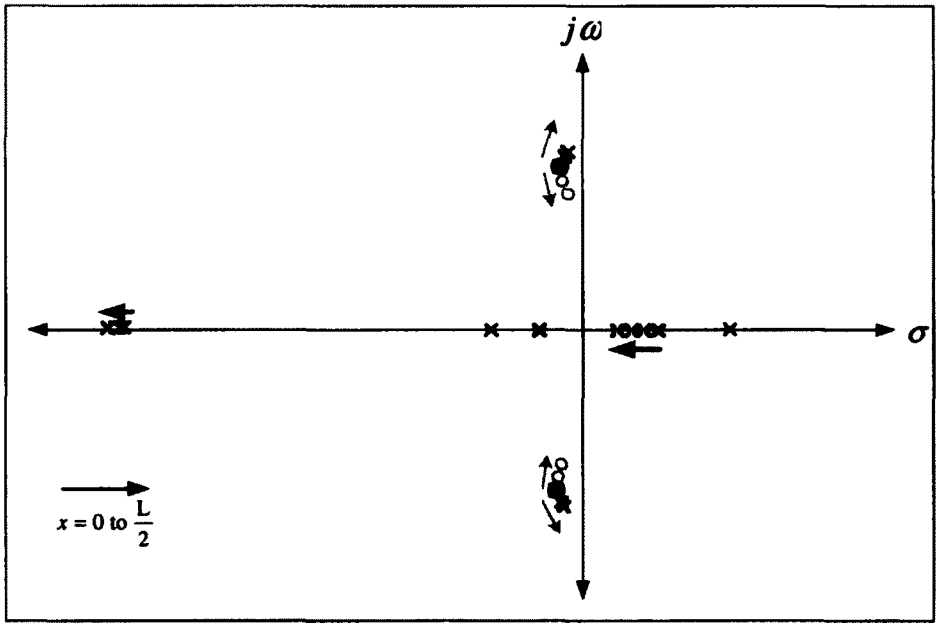

Figure 5.8. A Generic Pole-Zero Map of Centralized Scheme

The locations of the poles change periodically with time $T = L/v$ that the vehicle spend on one span. The vehicle's velocity affects the rate of change of the girder pole movement; on the other hand, it affects their movements more or less strongly depending on its value hence, this in fact affects the girder vibration shape.

5.4 MIMO Root Loci with Control Schemes

In this section, the technique that is utilized for plotting the generalized Multi Input Multi Output root loci is recalled. This technique was illustrated in Chapter 2 section 2.5.

5.4.1 MIMO Root Loci of De-centralized Control with a 2-DOF Maglev-Girder System

In order to plot the MIMO root loci for the 2-DOF Maglev-girder system with each controller, an important check should be performed, since different root loci can be achieved when the controller gains or scheme are changed. Each controller scheme should have a similar response when exposed to a step input. This will ensure that the de-centralized controller gains have a similar effect on the system as those of the centralized controller.

A Single Input Single Output (SISO) Maglev-girder system can be found from the generalized equation of motion in Eqs. (5.8-5.12) and the linearized SISO model from the generalized equations as in Eq. (5.18). A SISO Maglev-girder system has one force that is acting on a flexible girder with one vibration mode. This SISO system will possess five states that also vary with the vehicle's position on girder.

The PD controller for this system can be designed using the SISO-tool command in MATLAB, and the root locus is shown in Figure 5.9. The controller gains are then selected in order to yield stable closed loop poles. The selected controller gain based on

the SISO root locus is then used as an initial guess for the MIMO controller as shown next.

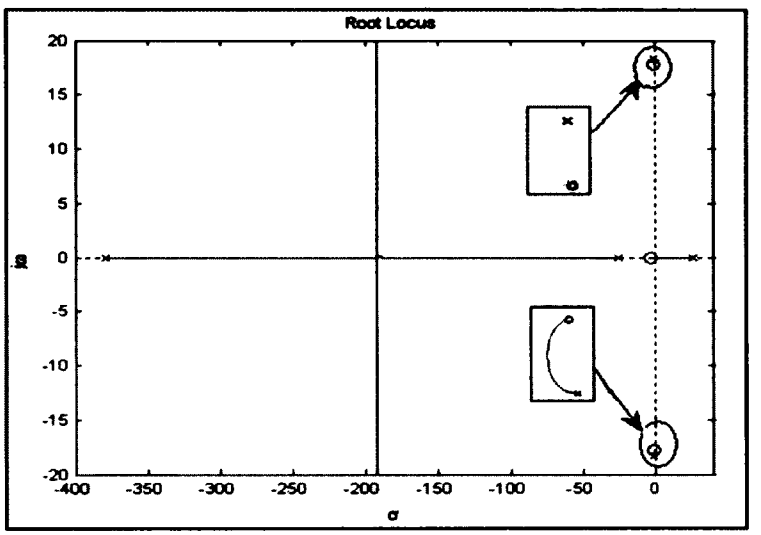

Figure 5.9. A SISO Root Locus

The MIMO root loci analysis for the 2-DOF Maglev-girder system is presented when de-centralized and centralized controllers are utilized. The idea is based on placing a scalar gain k with the controllers and varying it from zero to infinity in order to draw the root loci of the system as whole by the aid of MATLAB. The root loci of the system with the PD de-centralized control are shown in Figure 5.10. The PD de-centralized control does stabilize the system at different vehicle position locations ($x=0$, $x=L/4$, and $x=L/2$).The closed loop poles are marked by small squares that appear in the left hand plane.

When $x=0$, the interaction is not considered, and the girder poles coincide with the transmission zeros. Increasing the gain k leads to move the unstable translational and

rotational poles of the test-vehicle toward the left hand plane to become stable. On the other hand, increasing the gain k moves the electrodynamics poles toward the right side. At certain value of $k = k_{1d}$, the stable pole representing the translational motion along with one of the electrodynamics poles leaves the real axis from the same location (breakaway point). Thus, one track is heading up and the other track is heading down to infinity asymmetrically with an angle 90°. While the stable pole of the rotational motion leaves the real line with the other electrodynamics poles at $k = k_{2d}$ where the value k_{1d} is less than the value k_{2d}. The two asymptotic lines are located at σ_{s1} and σ_{s2} respectively on the right hand side of these breakaway points. The two unstable poles of the translational and rotational motions keep moving to the left side as k increases. When k tends to infinity, these two poles settle down in the left hand plane.

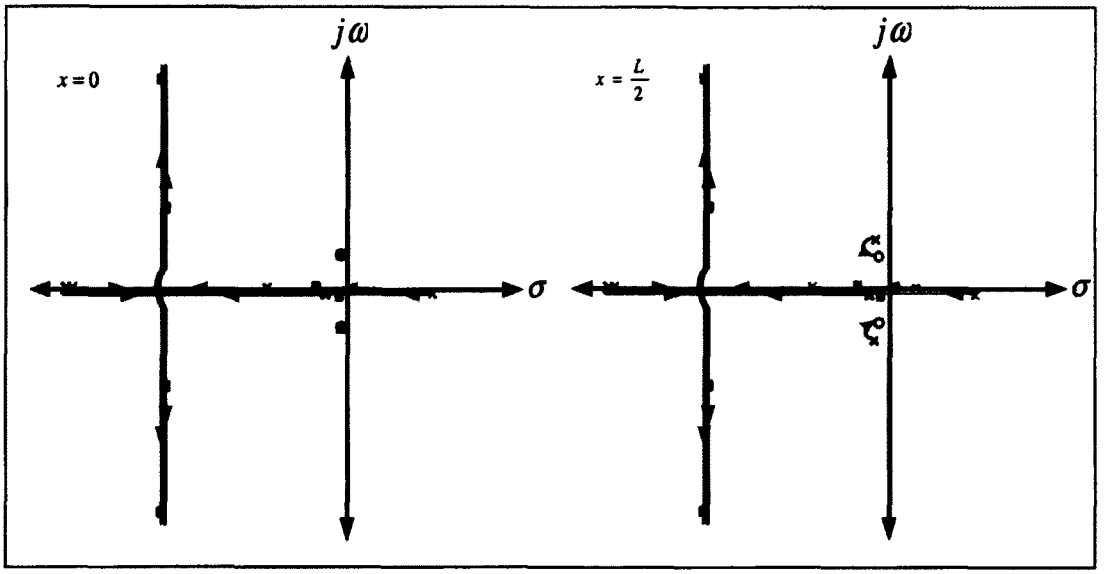

Figure 5.10. Root Loci of the PD De-centralized Control with 2-DOF Maglev-Girder System

When $x=L/2$ which is similar to $x=L/4$ ($x=3L/4$), increasing the gain k leads to move the translational and rotational poles of the test vehicle toward the left side. Other translational and rotational poles behave similarly as for $x=0$, and increasing the value of the gain k moves the girder vibration poles toward the transmission zeros, which represents the location of the vibration poles at $x=0$.

5.4.2 MIMO Root Loci of Centralized Control with a 2-DOF Maglev-Girder System

The root loci of the system with the PD centralized control are shown in Figure 5.11. The PD centralized control does stabilize the system at different vehicle position locations ($x=0$, $x=L/4$, and $x=L/2$). Similar to the de-centralized control, when $x=0$, the interaction is not considered, the girder poles coincide with the transmission zeros. As the gain k increases, the unstable heave and pitch poles of the test vehicle move toward the left hand plane to become stable. The electrodynamics poles toward the right. At certain value of $k=k_{1d}$, the stable pole presenting the pitch rotation along with one of the electrodynamics poles leave the real axis from the same location (breakaway point). Thus, one track is heading up and the other track is heading down to infinity asymmetrically with an angle 90°. While the stable pole of the heave motion leaves the real line with the other electrodynamics poles at $k=k_{2d}$ where the value k_{1d} is less than the value k_{2d}. The two asymptotic lines are located at σ_{s1} and σ_{s2} respectively on the right hand side of these breakaway points. The two unstable poles of the heave and pitch keep moving to the left side as k increases. When k tends to infinity, these two poles settle down in the left hand plane.

The root loci when $x=L/2$ is similar to the other cases as $x=L/4$ ($x=3L/4$). The same root loci behavior for the mechanical with the electrodynamics poles is received as for $x=0$, but the girder vibration poles move toward the transmission zeros, which represents the location of the vibration poles at $x=0$ as the gain k increases.

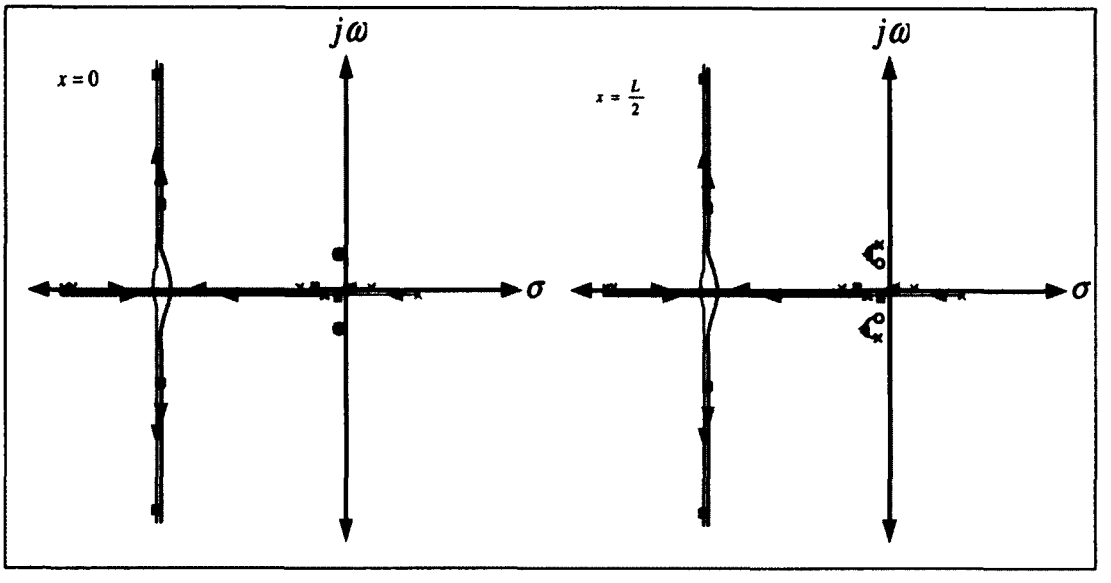

Figure 5.11. Root Loci of the PD Centralized Control with 2-DOF Maglev-Girder System

There are some notes to be drawn on the root loci of the de-centralized and centralized control:

- The root loci for the de-centralized and centralized controller are made for a unified step response.
- The root loci of the centralized control is different than of the de-centralized control as the open loop poles for both schemes are different as shown in figures 5.7 and 5.8.

5.5 Ride Quality

Ride quality is defined as the degree of human comfort offered by a moving vehicle [13, 80]. A rigorous analysis for ride comfort is difficult as it can be determined by changes in motion in all directions, effected by internal (physiological) and external factors (environmental) as well as human perception of vibrational motion, which is highly subjective and difficult to measure accurately.

Experimental studies in ergonomics have shown that acceleration is the primary quantity of vibration magnitude on which the human perception of vibrations depends on [80, 81]:

$$K = f(a) \tag{5.27}$$

where K is a nondimensional perception measure and a is the absolute value of the acceleration in horizontal or vertical direction, respectively. Vibration measurements are conducted according to a coordinate system originating at point from which vibration is considered to enter human body [81]. In addition, the position of the human body (seated, standing, and recumbent) is of importance. Figure 5.12 shows the coordinate system used to measure whole-body human vibration, adopted from [82].

The human body is sensitive to vibration in the frequency order of 0.5-20Hz because, most body-organ resonances occur in this range. The significance of ride quality is in that it could lower the initial investment costs if a design is not highly conservative with ride quality, and the perception of a smooth ride is important to establish the potential of Maglev systems [80].

For Maglev systems, ride quality is ultimately determined by horizontal and vertical surface profile of the guideway and by the levitation and guidance systems. Some aspects

that define this profile are known as surface roughness, and the levels of tolerable whole-body vibration [13].

A vehicle's velocity, acceleration, jerking, and other factors like noise, and temperature can also affect the ride quality.

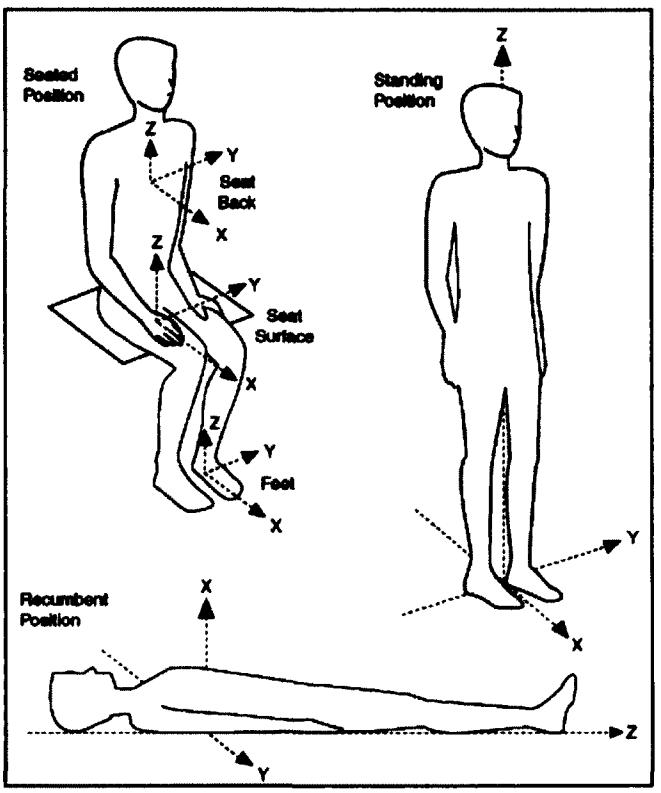

Figure 5.12. Direction of Response to Vibration of a Seated, Standing and Recumbent Position(c)

(c) ISO. This material is reproduced from ISO 2631-1:1997 with permission of the American National Standards Institute (ANSI) on behalf of the International Organization for Standardization (ISO). No part of this material may be copied or reproduced in any form, electronic retrieval system or otherwise or made available on the Internet, a public network, by satellite or otherwise without the prior written consent of ANSI. Copies of this standard may be purchased from ANSI, 25 West 43rd Street, New York, NY 10036, (212) 642-4900, http://webstore.ansi.org"

In practice, ride quality can be determined from the power spectrum plots for the vehicle's acceleration in the desired direction. These power spectrum plots to be implemented using the MATLAB Fast Fourier Transform (FFT) algorithm in which the single sided amplitude spectrum of the desired vehicle's acceleration are plotted [46].

5.6 De-centralized Control for ODU Maglev-Girder System

5.6.1 Controller Scheme

Figure 5.13 shows the de-centralized controller with the girder dynamics. The Maglev-girder interaction is implemented by a parallel connection between the EMS Maglev system block and the girder dynamics block.

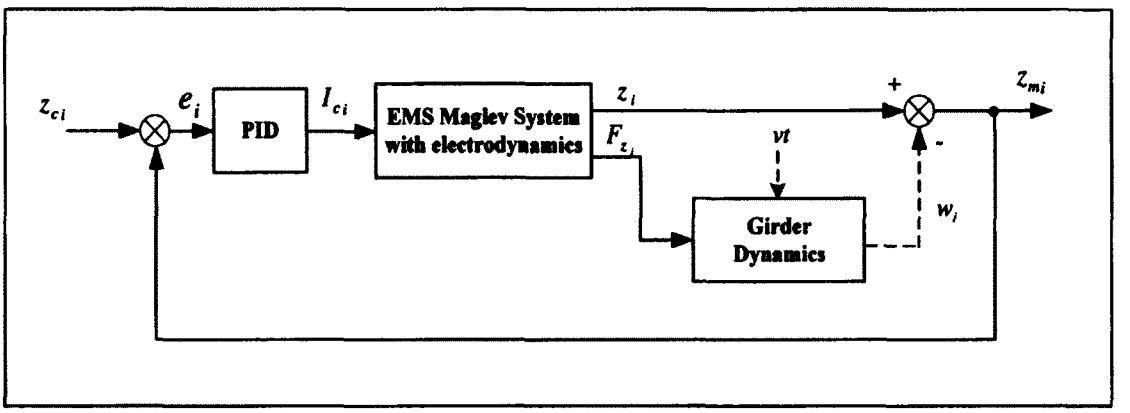

Figure 5.13. De-centralized Control Scheme with Girder Interaction

The magnet forces that are used for levitation are also input to the girder dynamics block, and the output of the girder dynamics block is the girder's vibration that is added with the airgap outputs from the EMS Maglev system block to have the measured actual airgaps. To have the effect of the vehicle's velocity on the overall system dynamics, the vehicle's velocity is also input to the girder dynamics block.

In the de-centralized control scheme, controllers are designed locally for each input-output pair as co-located actuators and sensors. The control logic aims to maintain the magnetic gap to a pre-set value z_c. These controllers are

$$I_{c_n} = K_{p_n} e_n + K_{I_n} \int e_n dt + K_{d_n} \dot{e}_n \quad , \quad e = z_c - z \tag{5.28}$$

where n =1,2,...,6 is the number of electromagnets, z_c is the command air gap.

5.6.2 Controller Gain Tuning using LQR Search Algorithm

The LQR based gradient like search algorithm for MIMO PID controller gains is used to tune the controller gain [74]. To apply this algorithm, the system original state vector should include the integration of the states because PID controller is used and the corresponding vehicle sub-model state vector x_d is:

$$x_d^T = \left[z_1 \quad \dot{z}_1 \quad \int z_1 dt \quad \dots \quad z_6 \quad \dot{z}_6 \quad \int z_6 dt \quad q_{v_1} \quad \dot{q}_{v_1} \dots \dot{q}_{v_4} \quad \dot{q}_{v_4} \quad I_1 \quad \dots \quad I_6 \right]$$

The generalized gain matrix K_{dec} for the de-centralized scheme is:

$$K_{dec} = \begin{bmatrix} k_{pz_1} & k_{dz_1} & k_{iz_1} & 0 & \cdots & & & \cdot & \cdot & 0 & \\ 0 & 0 & 0 & k_{pz_2} & k_{dz_2} & k_{iz_2} & & & & \vdots & \\ \vdots & \vdots & \vdots & & & & \ddots & & & 0 & 0_{6\times 6} \\ 0 & 0 & 0 & \dots & & & \cdot & k_{pz_6} & k_{dz_6} & k_{iz_6} & \end{bmatrix} \tag{5.29}$$

The PID de-centralized controller gains are the same as have been chosen in the previous chapters for the ODU Maglev vehicle but the gains are tuned to ensure stable operation when the Maglev vehicle runs on a flexible girder.

5.7 Centralized Control for ODU Maglev-Girder System

5.7.1 Controller Scheme

Figure 5.14 shows the centralized controller scheme for the vehicle-girder system, which is the same as in the previous section but after adding some necessary

transformation matrices to implement the centralized control. In the case of the centralized control, the local variables (air gaps) are measured and then converted into the test vehicle's rigid body modes (in this case heave, roll, and pitch) using a transformation matrix $[T_1]$. The vehicle's modes are controller to provide by the modal forces and torques. These modal forces and torques are transformed to local forces by $[T_2]^{-1}$. The command currents are generated from the local forces and the measured gaps via a transformation $[T_3]$ as shown in Figure 5.14. The expressions of these transformation matrices are given by the authors in [46].

These controllers are

$$F_{\Theta_i} = K_{p_i} e_{\Theta i} + K_{I_i} \int e_{\Theta i} dt + K_{d_i} \dot{e}_{\Theta i} \quad , \quad e_{\Theta_i} = \Theta_{c_i} - \Theta_i \tag{5.30}$$

where, F_{Θ_i} are the modal forces and torques command, $i = 1,2,\ldots,6$ is the number of modes, Θ_{c_i} : is the mode command.

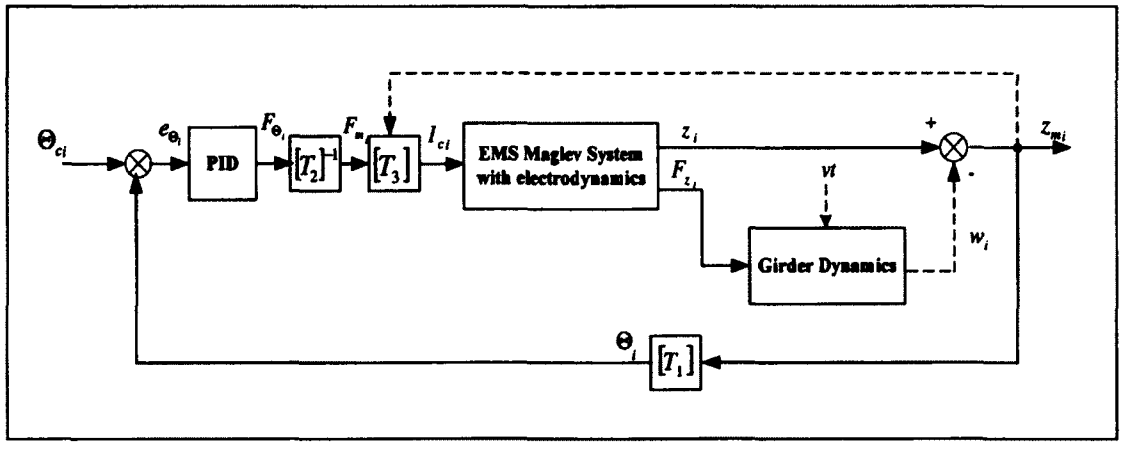

Figure 5.14. Centralized Control Scheme with Girder Interaction

5.7.2 Controller Gain Tuning using LQR Search Algorithm

Similarly, the algorithm that is used for MIMO PID controller gain tuning is incorporated. The LQR gradient like search algorithm, presented in section 3.5.1 and was found originally in [74] is used. Six states that representing the integration of the states to be added to the original state vector due to inclusion of the integrator term within the PID controller. Then the corresponding vehicle sub-model state vector x_c is

$$x_c^T = \begin{bmatrix} x & \dot{x} & \int x dt & \dots & \psi & \dot{\psi} & \int \psi dt & q_{v_1} & \dot{q}_{v_1} \dots \dot{q}_{v_4} & \dot{q}_{v_4} & I_1 & \dots & I_6 \end{bmatrix}$$

The generalized gain matrix K_{cen} for the centralized scheme is:

$$K_{cen} = \begin{bmatrix} k_{px} & k_{dx} & k_{ix} & 0 & \cdots & & & \cdot & \cdot & 0 & \\ 0 & 0 & 0 & k_{py} & k_{dy} & k_{iy} & & & & \vdots & \\ \vdots & \vdots & \vdots & & & & \ddots & & & 0 & 0_{6\times 6} \\ 0 & 0 & 0 & \dots & & & \cdot & k_{p\psi} & k_{d\psi} & k_{i\psi} & \end{bmatrix} \tag{5.31}$$

The PID centralized controller gains are the same as have been chosen in the previous chapters for the ODU Maglev vehicle but with the gains are tuned to ensure stable operation when the Maglev vehicle runs on a flexible girder.

5.8 Simulation Results

In this section, the simulation results for the ODU EMS Maglev system are presented. The Maglev system for both schemes including the vehicle and girder sub-models has 28 states. The girder vibration modes that are considered in the simulation are five. For the de-centralized control scheme, the controlled states are six airgap measurements, their derivatives, and their integrals. In order to calculate the proper optimized gain matrix by the search algorithm for both control schemes, a unified model configuration should be established. For the centralized control scheme, the states used

for control are the heave, the derivative of heave, the integral of heave, the pitch, the derivative of pitch, and the integral of pitch. Other states are not used for control because, the system controlled modes are heave and pitch. Two system configurations are assumed to have unified state space matrices *A, B,* and *C* for both schemes. In the first system configuration, the control inputs are the command currents I_{ci} ,the outputs are the airgaps z_i, and the search algorithm will optimize the performance index $J(I_{ci}, z_i)$ for both schemes to calculate the gain matrix. The resulting gain matrix is used directly with the de-centralized scheme, but for the centralized scheme, transformations should be applied to attain the proper gain matrix. In the other system configuration, the control inputs are the command currents I_{ci}, the outputs are the modes θ_i, and the search algorithm will optimize the performance index $J(I_{ci}, \theta_i)$ for both schemes to calculate the gain matrix. In order to use the optimized gain matrix for both schemes, the resulting gain matrix should be transformed by considering specific transformation matrices for each scheme individually.

In order to achieve good results, the algorithm should be initialized properly, which is a bit challenging. The necessity of having the same *J(K)* for both de-centralized and centralized after *n* iterations is very difficult and requires changing the weights until receiving the required result.

The simulation parameters include: ODU EMS Maglev bogie parameters like mass, moments of inertias, length, width, magnet parameters, girder parameters etc are as in [3]. Other simulation parameters, e.g. the initial conditions for simulation are zero except the initial airgap value which is 0.01m. The simulation is performed first on the centralized

controller on the Maglev system with the tuned gains at different velocities of 10, 20, 30 m/s.

Two simulation scenarios are made: one is based on the first configuration that minimizes the performance index $J(I_{ci}, z_i)$; and the other one of the second configuration minimizes the performance index $J(I_{ci}, \theta_i)$.

In the first simulation scenario, the system configuration inputs are the command currents, and the outputs are the gaps; therefore, the minimization is performed on the performance index $J(I_{ci}, z_i)$. Figures 5.15-19 show the first scenario results of the numerical simulation of both de-centralized and centralized controllers. In these figures, the time histories of the girder vibration w, bogie heave motion h_b, bogie measured air gap z_m at the magnets 1-2 , bogie measured air gap z_m at the magnets 3-4 and bogie measured air gap z_m at the magnets 5-6 are plotted. Note X^d, denotes the case of the de-centralized controller, while X^c, denotes the case of the centralized controller and $X = \{w, h_b, z_m\}$. The results presented are the steady state results after the vehicle has passed ten girders. In figures 5.14 and 5.16, the girder vibration and the bogie steady heave motion for both controllers are similar at low velocity. Increasing the bogie's velocity changes the girder vibration shape, hence the heave motion of the bogie is changed. In Figure 5.16-5.18, the bogie steady measured gaps at magnets 1-2, 3-4 and 5-6 for both controllers at different velocities for both configurations are shown. The variation in the measured gaps, when the centralized controller is employed, is greater than in case of the de-centralized controller.

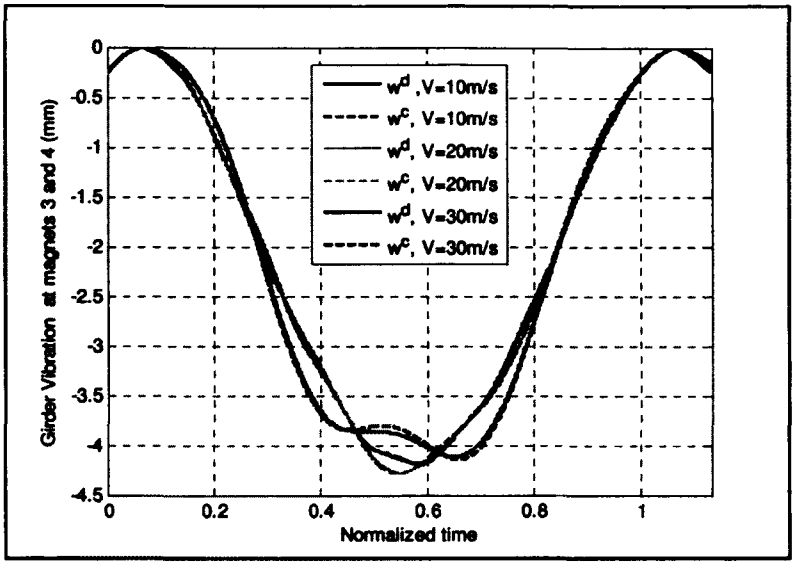

Figure 5.15. Girder Steady Vibration at Magnets 3 and 4 (Configuration 1)

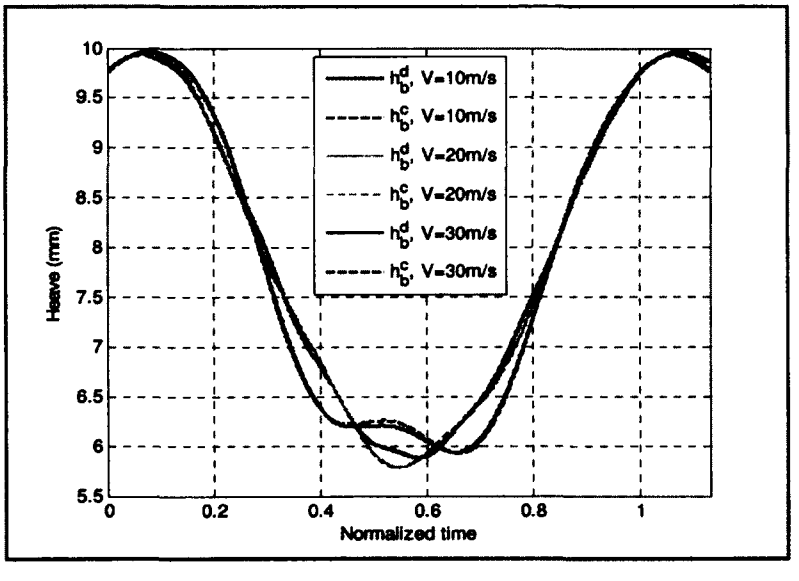

Figure 5.16. Bogie's Steady Heave Motion (Configuration 1)

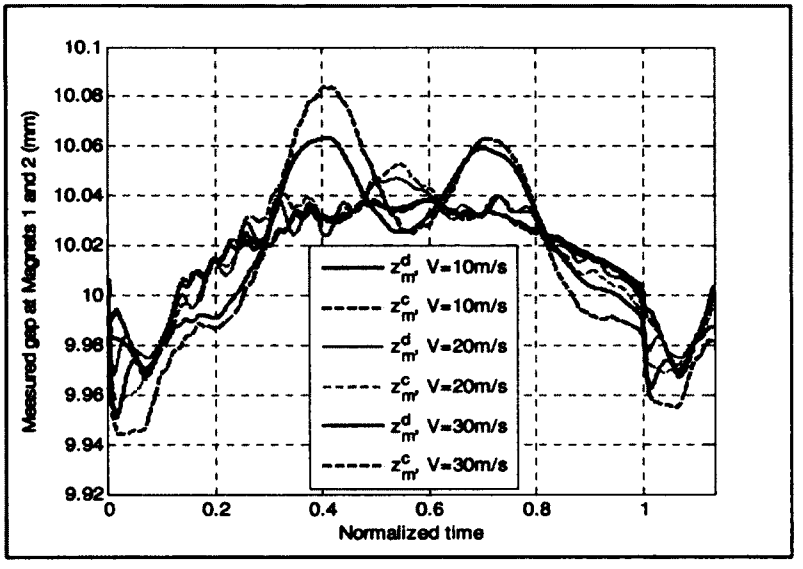

Figure 5.17. Bogie's Steady Measured Gaps at Magnets 1 and 2 (Configuration 1)

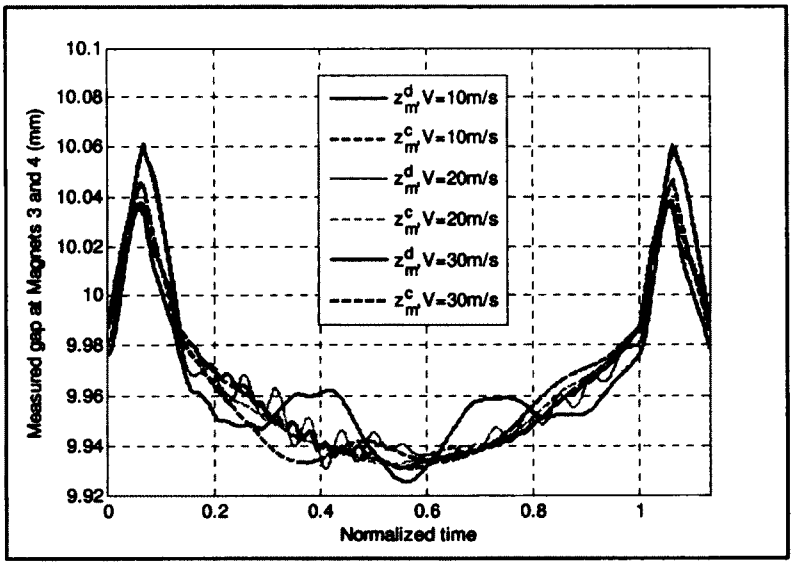

Figure 5.18. Bogie's Steady Measured Gaps at Magnets 3 and 4 (Configuration 1)

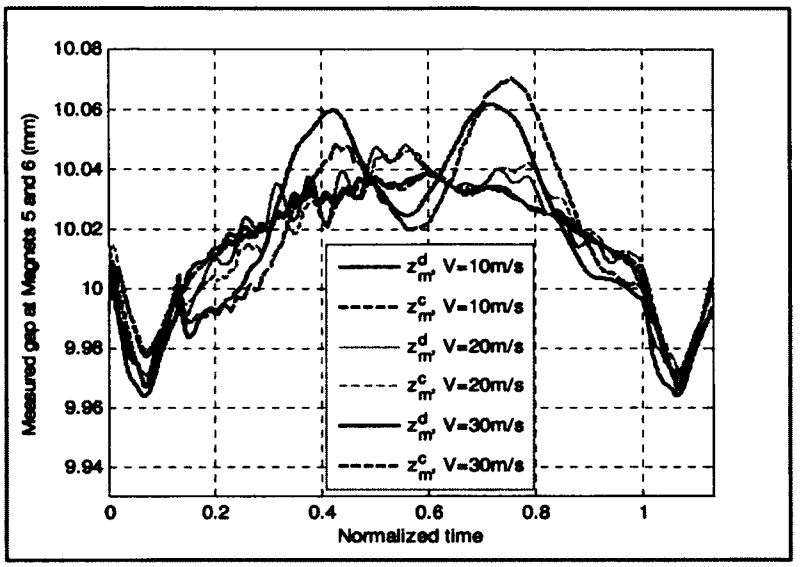

Figure 5.19. Bogie's Steady Measured gaps at Magnets 5 and 6 (Configuration 1)

In the second simulation scenario, the system configuration inputs are the command currents and the outputs are the modes; therefore, the minimization is performed on the performance index $J(I_{ci}, \theta_i)$. Figures 5.20-5.24 show the second scenario results of the numerical simulation of both centralized and de-centralized controllers. In these figures, the time histories of the girder vibration w, bogie heave motion h_b, bogie measured air gap z_m at the magnets 1-2 , bogie measured air gap z_m at the magnets 3-4 and bogie measured air gap z_m at the magnets 5-6 are plotted.

In figures 5.20 and 5.21, the girder vibration and the bogie steady heave motion for both controllers are similar at low velocity. Increasing the bogie's velocity changes the girder vibration shape, hence the heave motion of the bogie is changed.

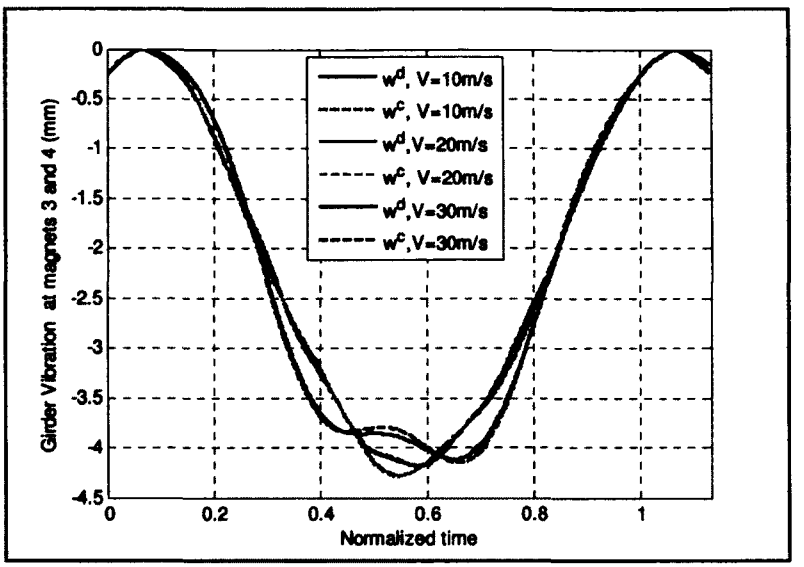

Figure 5.20. Girder Steady Vibration at Magnets 3 and 4 (Configuration 2)

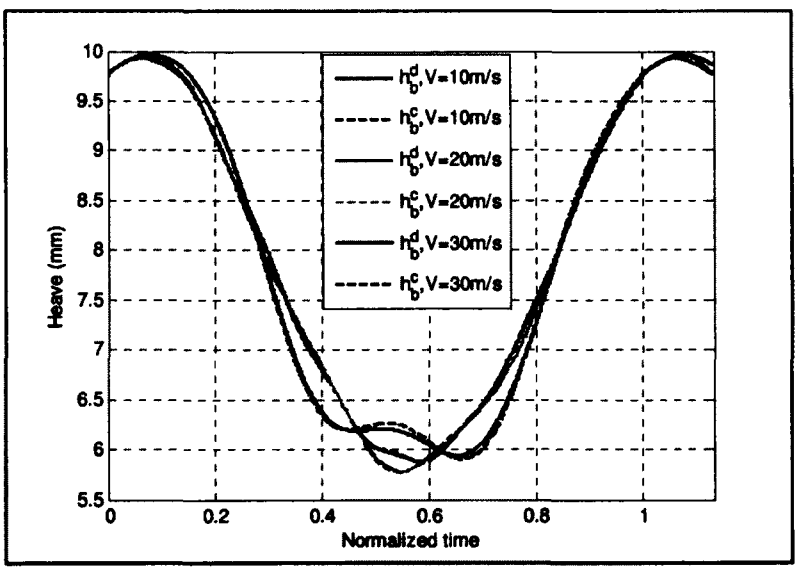

Figure 5.21. Bogie's Steady Heave Motion (Configuration 2)

In Figure 5.20-5.22, the bogie steady measured gaps at magnets 1-2, 3-4 and 5-6 for both controllers at different velocities for both configurations are shown.

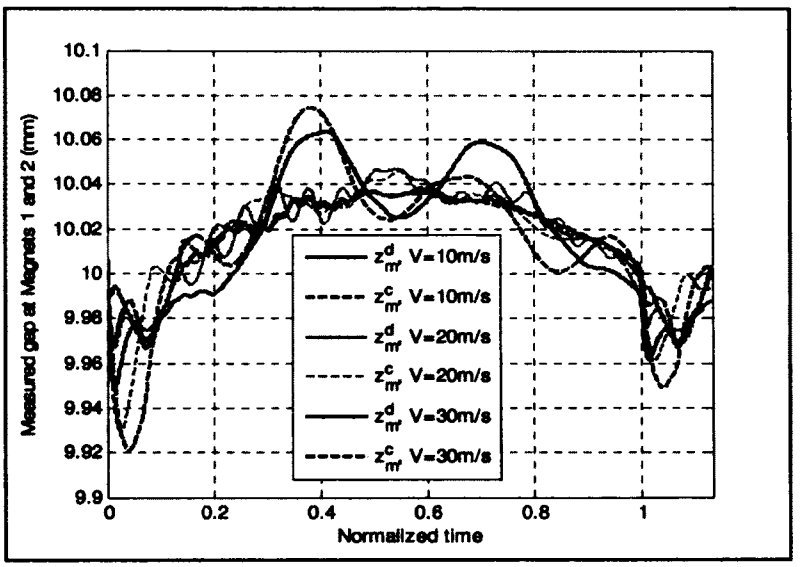

Figure 5.22. Bogie's Steady Measured Gaps at Magnets 1 and 2 (Configuration 2)

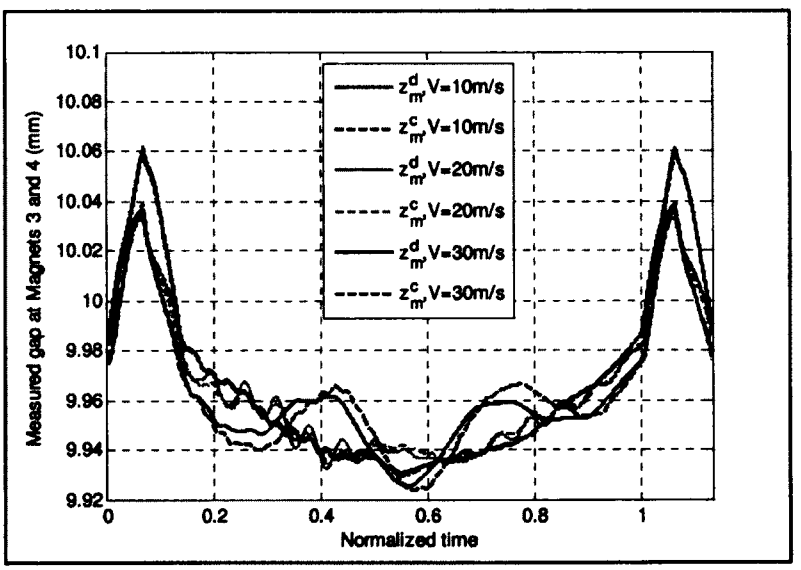

Figure 5.23. Bogie's Steady Measured Gaps at Magnets 3 and 4 (Configuration 2)

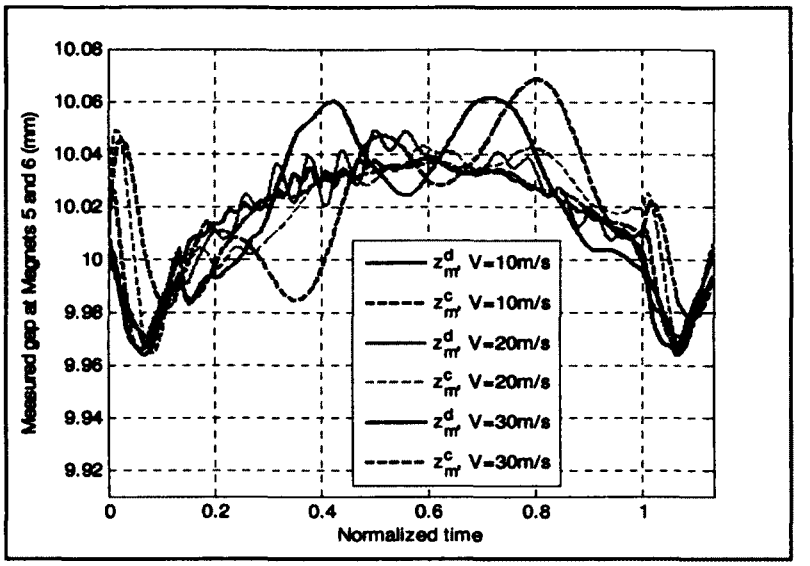

Figure 5.24. Bogie's Steady Measured Gaps at Magnets 5 and 6 (Configuration 2)

The ride quality analysis of both de-centralized and centralized controllers are performed based on the ISO2631 International Standard for evaluating mechanical vibration and shock for human body exposure [81]. According to ISO2631 International Standards for ride quality [81], the comfort reactions to vibrations for similar types of public transport are shown in Table 5.1.

Table 5.1 Comfort Reactions to Vibrations

Vibrations' Level	Comfort Reactions
Less than 0.315 m/s^2	Comfortable
From 0.315 m/s2 to 0.63 m/s^2	Little Uncomfortable
From 0.5 m/s2 to 1 m/s^2	Fairly Uncomfortable
From 0.8 m/s2 to 1.6 m/s^2	Uncomfortable
From 1.25 m/s2 to 2.5 m/s^2	Very Uncomfortable
Greater than 2 m/s^2	Extremely Uncomfortable

This standard is often represented based on a table of frequency weightings for the vertical acceleration at different frequencies. Figures 5.25, and 5.26 show the Power Spectrum Diagram (PSD) of the heave acceleration versus frequency for both controllers at velocity v = 30m/s for each configuration. The power spectrum plots are implemented using the MATLAB Fast Fourier Transform (FFT) algorithm by plotting the single sided amplitude spectrum of the bogie's vertical acceleration.

The maximum vertical acceleration for the first configuration that is observed in case of the centralized controller is at f = 3Hz and equals to 0.0497m/s^2 while in the case of the de-centralized controller, the maximum vertical acceleration is 0.0447 m/s^2 at the same frequency. While the maximum vertical acceleration for the second configuration that is observed in case of the centralized controller is at f = 3Hz and equals to 0.0522m/s^2, while in the case of the de-centralized controller, the maximum vertical acceleration is 0.0447 m/s^2 at the same frequency.

This could be due to the fact that the girder's first vibration mode is close to the heave frequency of the bogie. It is noted that for both de-centralized and centralized controllers, the requirement of having vertical accelerations below 0.315m/s^2 is satisfied, which implies smooth ride quality.

Based on comfort ride quality, it is noticed that the results received in the first scenario when the minimization is based on the command currents and airgaps $J(I_{ci}, z_i)$, are a little bit better than the other case.

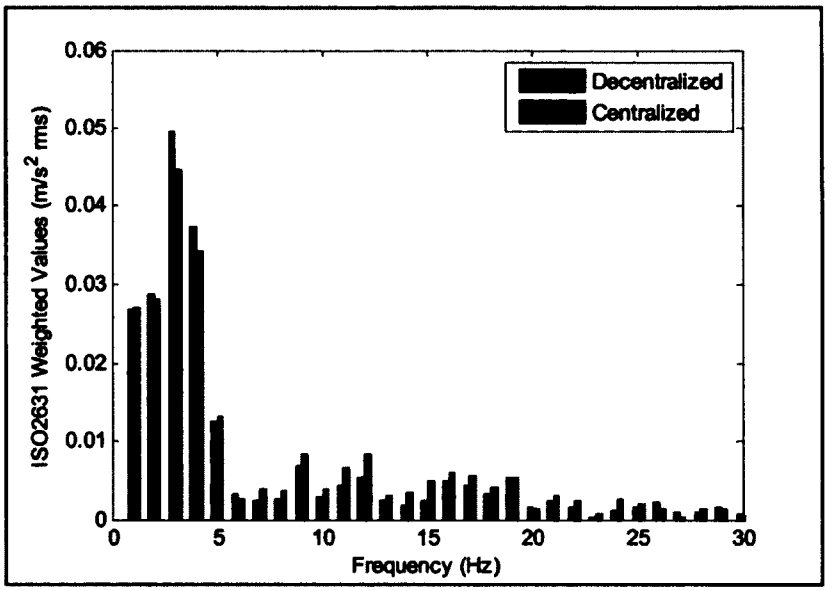

Figure 5.25. PSD Performance of De-centralized and Centralized Controllers

(Configuration 1)

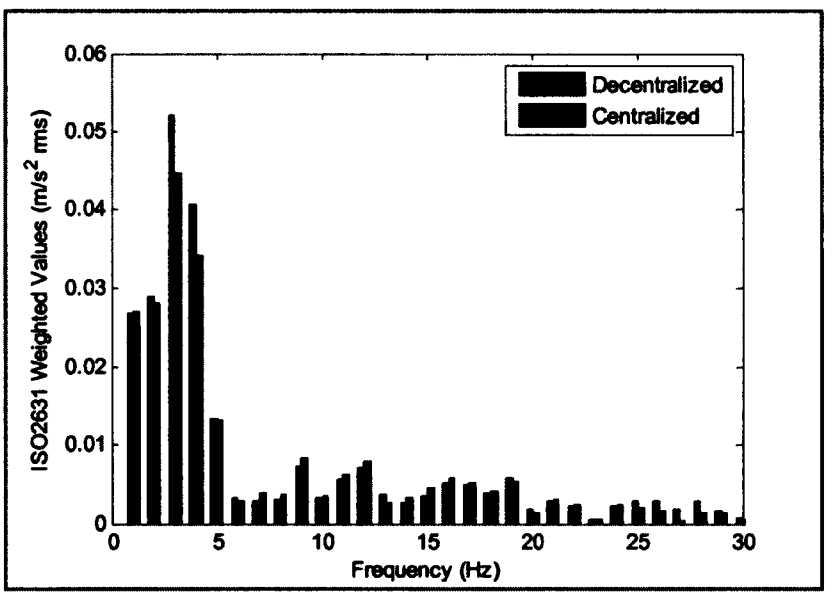

Figure 5.26. PSD Performance of De-centralized and Centralized Controllers

(Configuration 2)

5.9 Conclusions

In this chapter, the dynamic effect of the de-centralized and centralized controllers with a magnetically levitated vehicle when interacting with the girder is studied. The generalized Maglev-girder interaction LPV model, then a simple 2-DOFs Maglev-girder interaction model and their open loop pole zero map with centralized and de-centralized schemes are introduced. The MIMO root loci of the de-centralized and centralized controllers with the 2-DOFs Maglev-girder system are shown. The de-centralized and centralized controllers stabilize the Maglev system when interacting with a girder if their gains are chosen properly. The interaction between the vehicle and girder depends on the vehicle's position. This interaction changes the location of the whole system transmission zeros. By increasing (decreasing) the operating vehicle's velocity, the rate of change of the transmission zeros movement increases (decreases) which affects the overall system dynamics and hence changing the girder vibration shape and the heave motion of the vehicle.

A detailed simulation for the interaction between the vehicle and girder is also introduced. This simulation accounts for: vehicle dynamics, vehicle velocity, electromagnetic actuator dynamics, girder vibration, and controller schemes. A unified criterion for tuning of the PID controller gains for both schemes is established by utilizing a gradient like search algorithm that is based on an LQR technique. Two simulation scenarios are made; one is based on the first configuration that minimizes the performance index $J(I_{ci}, z_i)$ and the other one of the second configuration that minimizes the performance index $J(I_{ci}, \theta_i)$. Based on the numerical simulation, increasing the operating vehicle's velocity changes the girder vibration shape and the heave motion of

the vehicle. When the de-centralized control is utilized, the variation in the measured gaps is a little bit better than utilizing the centralized control. Due to the fact, that the de-centralized control is based on multiple individual controllers that minimize the error in the airgaps directly while the centralized control is designed to control the modes. The results received for the first configuration when the minimization is carried out on the performance index $J(I_{ci}, z_i)$ are a little bit better than the other one as it provides with better ride quality.

Both controller schemes (de-centralized and centralized) satisfy the ISO2631 standard. Thus, their maximum observed accelerations are much less than 0.315m /s^2, which satisfy the standard, ride quality comfort-range. The heave acceleration for the centralized control is a bit more than the de-centralized control especially at low frequencies, but it will not affect the ride quality and its smoothness significantly as it is much lower than the maximum limit found in the standard.

The comparison between the centralized and de-centralized controllers when equipped with EMS Maglev vehicle that interacts with a girder is complete. No significant difference is noticed between these two control schemes in their performance or ride quality, but the de-centralized control provides with a smoother ride quality in the heave direction.

CHAPTER 6

CONCLUSIONS AND RECOMMENDATIONS

In this chapter, conclusions from this research work are presented. Recommendations for future research that may be conducted on the ODU EMS Maglev system as a continuation of this endeavor are also introduced.

6.1 Conclusions

In the culmination of this Ph.D. research, I achieved some significant notes and results were achieved on de-centralized and centralized controllers used for EMS Maglev systems levitation, guidance, and when interacting with flexible girders. The analysis made by MIMO root loci for the 2-DOF EMS Maglev system (that utilized an inverted U-rail) levitation and guidance when using U-inverted rails proved that the de-centralized controller has no effect on the lateral poles, while the centralized control affects the lateral poles effectively. This is due to the fact that with de-centralized control lateral motion control is attained passively while with centralized control, lateral motion control is achieved actively by staggering the magnets. The simulation results for the 2-DOF EMS Maglev system coincide with the MIMO root loci analysis and when the work is generalized for the ODU Maglev system the same results are found. Centralized control is show to provide better lateral control than the de-centralized control for both rigid and flexible cases.

The experimental results of the ODU Maglev system with the de-centralized control are presented. The same control scheme for Maglev system simulation is used but with four

magnets instead of six magnets. The experimental results match the simulation results, and hence validate the design of the de-centralized controller.

The simulation results for the ODU Maglev system have shown that the centralized controller is better than the de-centralized one when the system is exposed to a lateral disturbing force such as wind gusts.

An important note on the centralized control is that it is not possible to achieve an accurate transformation from local measurements to modes and the number of controlled modes should be less than or equal to the number of magnets used. It could be a problem if the Maglev system has significant flexibility as it will not be possible to control all modes.

The centralized control does stabilize the rigid EMS Maglev system once the heave motion (unstable) is stabilized as already proven with the 2-DOF rigid EMS Maglev system.

Both de-centralized-flux feedback and centralized-flux feedback controllers do enhance the air gap response in comparison to the baseline de-centralized and centralized controllers. The flux feedback control when is in combination with de-centralized or centralized controllers does improve the air gap response and provides more resistance and robustness to air gap variations.

The significance of flux feedback appears for the Maglev systems that suffer from the problem of frequent air gap variations. It should be noted that having flux sensors added to the Maglev system is costly which means that we should not decide using flux feedback control unless it is required.

A generalized LPV Maglev-girder interaction model is established. The Maglev-girder interaction is depending on the vehicle's position on girder and the velocity changes the rate of the dynamics change of the overall system that changes the girder vibration shape. The change in the vehicle's position on girder moves the girder zeros on the $j\omega$ axis up and down and hence affects the girder vibration shape.

Both controller schemes (de-centralized and centralized) comply with the ISO2631 standard. Thus, their maximum observed accelerations are much less than 0.315m /s^2, which satisfy the standard ride quality comfort-range. The heave acceleration for the centralized control is a little higher than the case of the de-centralized control, especially at low frequencies, but it will not significantly affect the ride quality and its smoothness as it is much lower than the maximum limit found in the standard.

The conclusion is that the de-centralized and centralized control for EMS Maglev systems that interact with a flexible girder both provide similar ride quality, although the de-centralized control provides for less variation in the air gap measurements.

Centralized control with flux feedback could be the best controller for the ODU Maglev system when operating on the girder in the future. The centralized control will guarantee the suppression of the undesired lateral displacements; hence it will provide smoother ride quality. Flux feedback will suppress the air gap variations due to the track discontinuities.

6.2 Recommendations

According to the results achieved from this research work, it is recommended to use centralized controller rather than the de-centralized ones for EMS Maglev systems that

utilize inverted U-rails. These controllers provide both levitation and lateral control to an EMS Maglev system rigid or flexible with co-located sensors and actuators properly.

The stability of the centralized controllers are not guaranteed or investigated in detail, although a brief investigation that based on channels decoupling is introduced in this dissertation for a 2-DOF Maglev system. Further investigation is necessary especially when EMS Maglev system has significant flexibility. The effect of the flexibility on the EMS Maglev system stability and will the centralized controller cope with these effects is a big question.

The robustness of the de-centralized and centralized controllers when applied on the EMS Maglev system (rigid and flexible) can also be investigated versus parameters change as weight, and electromagnets' dimensions.

Ride quality for EMS Maglev systems that interact with girder is almost the same when de-centralized or centralized controllers are utilized if heave acceleration is considered. The girder model that is utilized in this dissertation considers the heave motion of the girder.

The girder dynamics model could be extended to be 3-DOF that includes the heave, roll and lateral modes instead of including only the heave mode. This will allow to study the influence of the de-centralized and centralized controllers on the lateral motion and its impact on the ride quality and stability of the EMS Maglev system. Furthermore, the influence of the different disturbances (e.g. crosswind forces), weight distribution (e.g. empty vehicle, full loaded, bias left and right), and track irregularities on the dynamic response of the system can also be studied.

REFERENCES

1. www.magnetbahnforum.de/index.php?en_what-is-Maglev.
2. Oleszczuk, G., *"Robustness and control of a Magnetically Levitated Transportation system,"* Ph.D. dissertation, Old Dominion University, Aug. 2006.
3. Hanasoge, A. M., *"Stability Analysis, Modeling, Simulation and Experimental Testing of an EMS Maglev System with Structural Flexibility"*, Ph.D. dissertation, Old Dominion University, Aug. 2009.
4. Alberts, T. and Hanasoge, A., "Modeling and Experimental Validation of an EMS Demonstration Vehicle", Maglev Conference-CA, USA, 2008.
5. Deodhar, A., Bawab, S., and Hanasoge, A., "Development and Validation of a Dynamic Model of the Maglev Transportation System at Old Dominion University", Maglev Conference, Dec. 2008.
6. Hanasoge, A., Hans, S., Bawab, S., Hou, G., and Alberts, T., "Effects of Track Irregularities on Dynamic Responses of a Moving Maglev Train", SAE International Conference, 2005.
7. Alberts, T., Hanasoge, A., Oleszczuk, G., "Stable Levitation Control of Magnetically Suspended Vehicles with Structural Flexibility," IEEE American Control Conference, 2008.
8. Davey, K., Morris, T., Britcher, C., Tola, R. and McCune, M. , "The Old Dominion University/American Maglev Demonstration System", 6th International Symposium on Magnetic Suspension Technology, Turin, Italy, 2001.
9. Alberts, T. E., Oleszczuk, G.," On the Influence of Structural Flexibility on Feedback Control System Stability for EMS Maglev Vehicles", Maglev Conference, 2006.

10. Limbert, D.A., Richardson, H., and Wormley D., "Controlled Dynamic Characteristics of Ferromagnetic Vehicle Suspensions Providing Simultaneous Lift and Guidance," ASME Journal of Dynamic Systems, Measurement, and Control, Vol. 101, Sep.1979.

11. Limbert, D.A., "*Analysis and Design of Ferromagnetic Vehicle Suspensions for Simultaneous Lift and Guidance of Tracked Levitated Vehicle*", ScD thesis, Massachusetts Institute of Technology, Dec.1976.

12. Worrnley, D. N., Richardson, H. H., Hedrick, J. K., and Limbert, D. A., "Noncontacting Suspension and Propulsion for Ground Transportation," MIT Contract DOT-OS-60135, 1979.

13. Sinha, P. K., *Electromagnetic Suspension-Dynamics & Control*, Peter Peregrinus, London, 1987.

14. Goodall, R.M., "Dynamics and Control Requirements for EMS Maglev Suspensions," in Proceeding of Maglev 2004, China, pp. 926-934, 2004.

15. Goodall, R.M., "The Theory of Electromagnetic Levitation," Physics in Technology 16(5): 207-2, 1985.

16. Goodall, R.M., "Electromagnetic Suspension Control without Airgap Measurement," Transactions of Measurements and Control, Vol. 11 No.2, 1989.

17. Szumko, S., and Dunn, M.J., "A Robust Observer for a Maglev System," Transactions of Measurements and Control, Vol. 13 No.2, 1991.

18. McLagen, N. S., "*Control of Electromagnetic Vehicle Suspension*", Ph.D. dissertation, Department of Engineering, University of Reading, June 1992.

19. Paddison, J. E., Macleod, C., Goodall, R. M., "State Variable Constraints on the Performance of Optimal Maglev Suspension Controllers", the third IEEE Conference on Control Applications, Aug.1994.

20. Taghirad, H. D., Abrishamchian, M., Ghabcheloo, R., "Electromagnetic Levitation System: An Experimental Approach", Proc. 7th Int. Conf. Electrical Engineering, Power Systems, pp. 19-26, Tehran, May 1998.

21. Cai, Y., Chen, S., and Rote, M., "Vehicle/Guideway Dynamic Interaction in Maglev Systems," Journal of Dynamic Systems, Measurement, and Control, Vol. 118, Issue 3, pp. 526-53, 1996.

22. WU, J., Zheng, J., and Zhou, Y., "Numerical Analyses on Dynamic Control of Five Degree of Freedom Maglev Vehicle Moving on Flexible Guideways," Journal of Sounds and Vibration. Vol. 38, No. 5, 2002.

23. Sinha, P., and Pechev, N., "Nonlinear H∞ Controllers for Electromagnetic Suspension Systems," IEEE Transactions on Automatic Control. Vol. 49, No. 4, 2004.

24. Guangwei S., Meisinger, R., Gang, S., "Simulation of a Maglev Train with Periodic Guideway Deflections", System Simulation and Scientific Computing, ICSC 2008.

25. Han, H., Yim, B., and Lee, B., Hur, Y., Kwon, J., "Vibration Analysis of a Maglev Vehicle Using Electromagnetic Suspension", Proceeding of International Conference on Electrical Machines and Systems, Seoul, Korea, 2007.

26. Shibo, R., Arie R., and Kees K., "Dynamic Simulation of the Maglev Vehicle/Guideway System," ASCE Journal of Bridge Engineering, May-June 2010.

27. Yaghoubi, H., and Rezvani, M. A., "Development of Maglev Guideway Loading Model," ASCE Journal of Transportation Engineering, Mar. 2011.

28. Yaghoubi, H., and Ziari, H., "Development of A Maglev Vehicle/Guideway System Interaction Model and Comparison of the Guideway Structural Analysis with Railway Bridge Structures," ASCE Journal of Transportation Engineering, Feb. 2011.

29. Yau, D., "Vibration Control of Maglev Vehicles Traveling over a Flexible Guideway," Journal of Sound and Vibration, Vol. 321, Issue 1-2, pp. 184-200, 2009.

30. Wang, P., Li, J., and Zhang, K., "Vibration Analysis of the Maglev Guideway with the Moving Load," Journal of Sound and Vibration, pp. 621–640, 2007.

31. Yau, J., and Yang, Y., "Vertical Accelerations of Simple Beams Due to Successive Loads Traveling at Resonant Speeds," Journal of Sound and Vibration, Vol. 289, pp. 210–228, 2006.

32. Sinha, P.K., Jayawant, B.V., "Analytical and Design Aspects of Magnetically Suspended Vehicles," Automatica, Vol. 15, Issue 5, pp. 539-552, Sept. 1979.

33. "Design Principles High-speed Maglev System (MSB)", Federal Railway Authority of Germany, 2007.

34. Morishita, M., "Robust Controller Design for Maglev Transport Vehicles with a Guide-Effective Electromagnetic Suspension System", Decision and Control, Proceedings of the 35th IEEE, 1996.

35. Shen,G., Meisinger R., Shu, G., "Modeling of a High-Speed Maglev Train with Vertical and Lateral Control," Vehicle System Dynamics, Vol. 46,Supplement, pp. 643-651, 2008.

36. The M^3 Urban Transportation System, A Report submitted to the Federal Transit Administration as a part of FTA Project MA-26-7077, 2003.

37. Schierman, J. D., Schmidt, D. K., "Limitations of Decentralized Control, "AIAA Journal of Guidance, Control and Dynamics, Vol. 20, No. 2, 1997.

38. Wang, S., Davison, E. J., "On the Stabilization of Decentralized Control Systems", IEEE Transactions on Automatic Control, Vol. 18, No. 5, pp. 473-478, 1973.

39. Aldeen, M., "Class of Stabilizing Decentralized Controllers for Interconnected Dynamical Systems", IEE Proceedings, D, Vol. 139, No. 2, 1992.

40. Siljak, D., "Decentralized Control and Computations: Status and Prospects," Annual Reviews in Control, Vol. 20, pp. 131-141, 1996.

41. Skogestad, S.and Postlethwaite, I., *Multivariable Feedback Control: Analysis and Design*, Second Edition, John Wiley and Sons Ltd., 2005.

42. Sinha, P.K., "Dynamics of Magnetically Suspended Vehicles," Transactions of the Institute of Measurement and Control, Vol. 1, Issue 1, pp. 57-64, Jan. 1979.

43. Bittar, A., Cruz , J., and Sales, R. M., "A New Approach to the Levitation Control of an Electromagnetic Suspension Vehicle", Proceedings of IEEE International Conference on Control Applications, Italy, Sept. 1998.

44. Shimizu, T., Sasaki, M., Wajima, K., "Passivity Based Control of a Magnetic Levitation System with Two Electromagnets for a Flexible Beam", Proceedings of 8th IEEE International Workshop on AMC, 2004.

45. Shimizu, T., Kobayashi, Y., Sasaki, M., Okada, T., "Passivity-Based Control of a Magnetically Levitated Flexible Beam," International Journal of Robust and Nonlinear Control, Vol. 19, Issue 6, pp. 662-675, April 2009.

46. Alberts, T., Aly, M., Omran, A., "Maglev-Girder Interaction for Centralized and Decentralized Controllers", 2010 ASME Dynamic Systems and Control Conference, Sept. 13-15, 2010.

47. Brzezina, W.,and Langerholc, J., "Lift and Side Forces on Rectangular Pole Pieces in Two Dimensions," Journal of Applied Physics Vol. 45, issue 4, pp. 1869 -1872, 1974.

48. Joshi, S. M., "Control of Large Flexible Structures", Lecture Notes in Control and Informational Sciences, Springer-Verlag, 1989.

49. Bristol, E.H., "RGA 1977: Dynamic Effects of Interaction," IEEE Conference on Decision and Control, 1977.

50. McAvoy, T.J.,"Connection between Relative Gain and Control Loop Stability and Design," AIChE Journal, Vol. 27, No.4, July 1981.

51. Wang, Q., Ye, Z., and Cai, W., Han, C., "PID Control for Multivariable Processes," Springer-Verlag Berlin, 2008.

52. Niederlinski, A., "A Heuristic Approach to the Design of Linear Multivariable Interacting Control Systems", Automatica, Vol. 7, pp. 691-701, 1971.

53. Shaked, U., "The Angles of Departure and Approach of the Root-Loci in the Linear Multivariable Systems," International Journal of Control, Vol. 23, No. 4, pp. 445-457, 1976.

54. MacFarlane, A. G. J., "Multivariable Nyquist-Bode and Multivariable Root-locus Techniques," Proceedings of the IEEE Conference on Decision and Control, Clearwater, Florida, Dec. 1976.

55. Newman, B.; Dongyu, F., "Sketching Rules for the Multivariable Root Locus Design Technique", American Control Conference, 1998.

56. O. N. Gasparyan, "Linear and Nonlinear Multivariable Feedback Control: a Classical Approach", John Wiley & Sons, Sussex, UK, 2008.

57. Bar-on, J. R., and Adams, R. J., "Multivariable Gain and Phase Margin Analysis of a Fully Coupled Six-Degree-of-Freedom Guided Missile", Proceeding of the International Conference on Control Applications, Hawaii, 1999.

58. Chen, D., Seborg, D. E., "Multiloop PI/PID Controller Design Based on Gershgorin Bands", Proceedings of the American Control Conference, Arlington, VA, June 25-27, 2001.

59. Zhuang, M., "*Computer Aided PID Controller Design*", PhD thesis, School of Engineering, University of Sussex, 1992.

60. Wang, Q.G., Zou, B., Lee, T.H., Bi, Q., "Auto-tuning of Multivariable PID Controllers from Decentralized Relay Feedback," Automatica, Vol. 33, pp. 319–330, 1997.

61. MacFarlane, A.G.J., *Complex Variable Methods for Linear Multivariable Feedback Systems*, Taylor and Francis, 1980.

62. Belletrutti, J.J. and MacFarlane, A.G.J., "Characteristic Loci Techniques in Multivariable Control System Design", Proceeding of IEE, Vol. 118, pp. 1291-1297, 1971.

63. Macfarlane, A.G.J. and Belletrutti, J.J., "The Characteristic Locus Design Method," Automatica, Vol. 9, Issue 5, pp. 575-588, 1973.

64. MacFarlane, A.G.J. and Postlethwaite, I., "The Generalised Nyquist Stability Criterion and Multivariable Root Loci," International Journal of Control, Vol. 25, pp. 81-127, 1977.

65. Falb, P. L., Wolovich, K. A., "Decoupling in the Design and Synthesis of Multivariable Control Systems", IEEE Transactions on Automatic Control, Vol. 12, No.6, pp. 651-659, 1967.

66. Mufti, I., "A Note on Decoupling of Multivariable Systems," IEEE Transactions on Automatic Control, Vol. 14, No.4, pp. 415-416, 1969.

67. Ho, W., Hang, C., and Zhou, J., "Self-Tuning PID Control of a Plant with Under-Damped Response with Specifications on Gain and Phase Margins," IEEE Transactions on Control Systems Technology, Vol. 5, No.4, 1997.

68. Machacek, J., "Unified Approach to Decentralized Control", Proceedings of 2000 IEEE International Conference on Control Applications, Glasgow, Sept. 2002.

69. Rodrigo, M.A., Seco, A., Ferrer, J., Penya-roja, J.M., Valverde ,J.,L., "Nonlinear Control of an Activated Sludge Aeration Process: Use of Fuzzy Techniques for Tuning PID Controllers," ISA transactions, Vol. 38, pp. 231-241, 1999.

70. Sinha, P.K., Pech, G., Abbassi, H. A., "Digital Control of an Electromagnetic Suspension System Using the TMS-32020 Signal Processor", Automatica, Vol. 27, No.6 pp. 1051-1054, 1991.

71. Brogan, W., *Modern Control Theory*, 3rd Edition, Printice-Hall, 1991.

72. Martin, G.D., "*On the Control of Flexible Mechanical Systems*", Ph.D. dissertation, Stanford University, May 1978.

73. Aly, M., Alberts, T., "De-centralized and Centralized Control for EMS Maglev System Levitation and Guidance", 2011 ASME Dynamic Systems and Control Conference, Arlington, Virginia Oct. 31st -Nov. 2nd, 2011.

74. Silva, E. and Erraz, D., "An LQR based MIMO PID Controller Synthesis Method for Unconstrained Lagrangian Mechanical Systems", Proceedings of the 45th IEEE Conference on Decision & Control, Dec. 2006.

75. Wells, J. M., "*Aerodynamic Analysis of an Urban Magnetic Levitation Vehicle*", MSc thesis, Old Dominion University, Dec. 2009.

76. www.mathworks.com/products/xpctarget/

77. Aly, M., and Alberts, T., "On Levitation and Lateral Control of EMS Maglev Systems," ASME Journal of Dynamic Systems Measurements and Control, Sent on October 2011 (Accepted).

78. Aly, M., Omran, A., Alberts, T., "Multi Input Multi Output Root Loci Analysis of EMS Maglev-Girder Interaction System", 2011 ASME Dynamic Systems and Control Conference, Arlington, Virginia Oct. 31st -Nov. 2nd, 2011.

79. Albertos, P. and Sala,A., "Multivariable Control Systems: An Engineering Approach", 1st Edition Edition, Springer, 2003.

80. Cai, Y., Chen,S., "Dynamic Characteristics of Magnetically-levitated Vehicle Systems," ASME Applied Mechanics Reviews, Vol. 50, issue 11, pp. 647, 1997.

81. Schiehlen, W., *Dynamical Analysis of Vehicule Systems*, CISM Courses and Lectures, SpringerWienNewYork, 2009.

82. Mechanical Vibration and Shock – Evaluation of Human Exposure to Whole Body Vibration – Part 1: General requirements, ISO2631-1.

RESUME

Mohamed M. Aly M. Moawad
1056 W.48th St., Apt.6, Norfolk, VA 23508
(757)-339-7049, mohamed.aly@gmx.com

EDUCATION

Ph.D. Mech. and Aero. Eng, Old Dominion University, VA-USA, May 2012
Major: Dynamics and Control GPA 3.93
M.S. Elec. Eng., Cairo University, Egypt, March 2006 Major: Automatic Control
B.S. Elec. Eng., Benha University, Egypt, June 1999 Major: Control & Measurements

EXPERIENCE

Old Dominion University, Mechanical and Aerospace Engineering dept., Norfolk, VA
Graduate Teaching and Research Assistant, Aug. 2008 to present.

NARSS, Cairo, Egypt- Yuzhnoye, Dnipropetrovs'k, Ukraine
EgyptSat-1 Project (MDR to OIR stage)
Control Engineer, March 2001 to Aug. 2008

- Developing the ADCS checking algorithms for ground and flight testing.
- Performing ADCS devices functioning check, and designing ADCS integrated tests programs for bench tests.
- Following the satellite Engineering and Flight models integrated tests and analyzing the telemetry data of the ADCS during these tests.
- Developing analytical programs for the analysis and verification of the satellite ADCS performance while the satellite operation in orbit.

Air Defense College, Alexandria, Egypt
Teaching Assistant, March 2000 to March 2001

Benha University -Egypt
Teaching Assistant, Fall Semester 1999

Automotive and Electric Company, Cairo-Egypt
Maintenance Engineer, Sept. 1999 to Jan. 2000

SELECTED PUBLICATIONS

M. Zahran and **M. Aly,** "Solar Cell based a Coarse Sun Sensor for a Small LEO Satellite Attitude Determination", Journal of Power Electronics Science & Technology, Vol. 9, No. 4, July 2009.

M. Aly, H. Abdel Fatah and A. Bahgat, "Nonlinear Observers for Spacecraft Attitude Estimation in Case of Yaw Angle Measurement Absence," International Journal of Control, Automation, and Systems, Vol. 8, No. 5, October 2010.

M. Aly, and T. Alberts, " On Levitation and Lateral Control of EMS Maglev Systems," sent to ASME Journal of Dynamic Systems Measurements and Control, 2011 (accepted).